CDF/ANAL/EXOTIC/CDFR/10765
Version 2.6
September 15, 2014

Search for the Fermiophobic Higgs Boson in the $3\gamma + X$ Final State

Atsunari Hamaguchi, Toru Okusawa, Yoshihiro Seiya, and Kazuhiro Yamamoto

Osaka City University, Japan

Abstract

We search for the fermiophobic Higgs boson (h_f), in the context of the two Higgs doublet model (type I), using $3\gamma + X$ events in $p\bar{p}$ collisions at $\sqrt{s} = 1.96$ TeV. In this model, the h_f is assumed to be produced in association with the charged Higgs boson ($H^\pm$) followed by the $H^\pm$ decaying to $h_f W^*$ and both of the two h_f's decaying to 2γ. The data were collected with the CDF-II detector at the Fermilab Tevatron collider and correspond to an integrated luminosity of 9.2 fb^{-1}. The number of backgrounds is estimated to be 2.96 ± 0.94 events, where the direct triphoton production dominates the contribution. The expected numbers of signal events are estimated for a set of the h_f and $H^\pm$ mass combinations. For example, it is 35 events for the h_f mass 75 GeV and the $H^\pm$ mass 120 GeV, with H^0 mass = 500 GeV, A^0 mass = 350 GeV, and $\tan\beta = 10$. The observed number of events in the data is 5. From these results, we obtain the limits on $\sigma(p\bar{p} \to h_f H^\pm) \times \mathcal{B}(H^\pm \to h_f W^*) \times [\mathcal{B}(h_f \to 2\gamma)]^2$ at the 95% confidence level. By comparing with the theoretical cross sections, the cross section limits are translated to h_f mass constraints for a given $m_{H^\pm}$, which are collectively represented as a rather large excluded region on the m_{h_f} vs. $m_{H^\pm}$ plane.

1 Introduction

Understanding the mechanism of electroweak gauge symmetry breaking (EWSB) is considered, for a long time, to be one of the most important milestones and major challenges in the elementary particle physics. In the Standard Model (SM), a doublet of complex scalar fields, the Higgs fields, are introduced to explain the EWSB and the origin of particle masses via a spontaneous EWSB, the so-called the Higgs mechanism.

The experiments using the Large Hadron Collider (LHC) at CERN discovered a scalar boson in 2012 [1]. The results support that the EWSB be indeed related to a scalar boson. Moreover, it was recently reported that the new particle actually coupled to fermions [2], which is also expected for the SM Higgs boson. The whole picture of the EWSB is, however, yet to be investigated. Even if the new particle is confirmed to be the SM Higgs boson, it does not mean that, for example, there are no other Higgs bosons, and there could be multiple Higgs bosons in the underlying fundamental physics. It is thus still necessary to continue testing various senarios as long as they are not explicitly excluded.

A minimal multiple-Higgs model is the "two Higgs doublet model" (2HDM). The resulting particle spectrum consists of two charged Higgs bosons H^+, H^- and three neutral members h^0, H^0 and A^0. The fermiophobic Higgs boson, which signifies very suppressed or zero couplings to the fermions, may arise in a particular version of the 2HDM called type I.

1.1 Models with fermiophobia

The 2HDM (type I) was first proposed in [3]. In this model, one Higgs doublet (Φ_2) of the $SU(2) \otimes U(1)$ gauge group couples to all the fermion types, while the other doublet (Φ_1) does not. Both couple to the gauge bosons via the kinetic term in the Lagrangian. One vacuum expectation value (v_2) gives masses to all the fermion types, while the gauge bosons receive their masses from both the v_1 and v_2.

Due to the mixing in the CP-even neutral Higgs sector, both the CP-even eigenstates h^0 and H^0 can couple to the fermions. The fermionic coupling of the lightest CP-even Higgs boson h^0 takes the form

$$h^0 f \bar{f} \sim \frac{\cos\alpha}{\sin\beta} \,,$$

where the f is any fermion, the α is the mixing angle in the neutral Higgs sector h^0 and H^0, and the β is defined by

$$\tan\beta = \frac{v_2}{v_1} \,.$$

Small values of the $\cos\alpha$ would seriously suppress the fermionic coupling, and in the limit

$$\cos\alpha \to 0 \,,$$

the coupling $h^0 f \bar{f}$ would vanish, giving rise to the fermiophobia and the h^0 is called a fermiophobic Higgs[1] (h_f).

The main decay mode of the h_f is

$$h_f \to 2\gamma$$

for $m_{h_f} \lesssim 95$ GeV as shown in Fig. 1 based on PYTHIA Monte Carlo (MC) calculations. The branching fraction ($\mathcal{B}$) is near 100% for $m_{h_f} \lesssim 80$ GeV, decreasing to 50% at $m_{h_f} \simeq 95$ GeV, and to 1% at $m_{h_f} \simeq 145$ GeV. In contrast, the $\mathcal{B}(\phi^0 \to 2\gamma) \simeq 0.22\%$ is the largest value in the SM, where the ϕ^0 represents the SM Higgs boson. We shall be focusing on the possibility of a light h_f,

$$m_{h_f} \lesssim 100 \text{ GeV} ,$$

for which the photonic decay mode always has a large $\mathcal{B}$.

1.2 Previous searches

The h_f had been searched for at the LEP, Tevatron, and the LHC experiments. A conventional h_f production and decay process at e^+e^- colliders is

$$e^+e^- \to Z^* \to h_f(\to 2\gamma)Z ,$$

and at hadron colliders

$$q\bar{q}' \to V^* \to h_f(\to 2\gamma)V ,$$

with the dominant contribution coming from $V = W^\pm$.

The OPAL and DELPHI collaborations also searched for the process

$$e^+e^- \to h_f(\to 2\gamma)A^0 ,$$

and the L3 collaboration considered

$$e^+e^- \to h_f(\to WW^*)Z$$

as well. The LEP ruled out regions on the plane

$$R \times \mathcal{B}(h_f \to 2\gamma) \quad \text{vs.} \quad m_{h_f},$$

where the R is defined by

$$R = \frac{\sigma(e^+e^- \to h_f Z)}{\sigma(e^+e^- \to \phi^0 Z)} .$$

In the benchmark scenario of the $R = 1$ and assuming $\mathcal{B}(h_f \to 2\gamma)$ given by [4, 5], each of the LEP collaborations, OPAL, DELPHI, ALEPH, and L3, derived a limit of

[1] Sometimes called a "bosonic" or "bosophillic" Higgs boson as well.

$m_{h_f} \gtrsim 100$ GeV at the 95% confidence level (C.L.). A combination of the results [6] yielded a lower bound

$$m_{h_f} > 109.7 \text{ GeV} .$$

In the Tevatron Run II, the lower limit on the m_{h_f} from the combined CDF and DØ analyses [7] was

$$m_{h_f} > 119 \text{ GeV}$$

at the 95% C.L., where the processes

$$q\bar{q}' \to V^* \to h_f(\to \gamma\gamma)V , \qquad q\bar{q}' \to V^* \to h_f(\to WW^*)V ,$$

$$q\bar{q}' \to q\bar{q}' h_f(\to 2\gamma) , \qquad q\bar{q}' \to q\bar{q}' h_f(\to WW^*) ,$$

were considered in the analysis.

Both the ATLAS and the CMS collaborations searched for

$$q\bar{q}' \to V^* \to h_f(\to \gamma\gamma)V , \qquad q\bar{q}' \to q\bar{q}' h_f(\to 2\gamma) ,$$

and obtained the results

$$m_{h_f} \notin 110\text{–}118 , \ 119.5\text{–}121.0 \text{ GeV} ,$$

and

$$m_{h_f} \notin 110\text{–}147 \text{ GeV} ,$$

respectively [8].

All these mass limits assumed that the $h_f VV$ coupling was of the same strength as the SM coupling $\phi^0 VV$, which in general would not be the case for the h_f in a realistic model such as the 2HDM (type I). The condition for the fermiophobia ($\cos\alpha \to 0$) causes the coupling $h_f VV$ to be suppressed by a factor

$$h_f VV \sim \sin^2(\beta - \alpha) \to \cos^2\beta \equiv \frac{1}{1 + \tan^2\beta} .$$

Taking $\tan\beta > 3$ (10) implies a strong suppression of ~ 0.1 (0.01) with respect to the coupling $\phi^0 VV$. It is not difficult to see that such a suppression in the R would permit a light h_f with the mass of ~ 80 (50) GeV, thus sizable regions of the $R \times \mathcal{B}(h_f \to \gamma\gamma)$ vs. m_h plane remain unexcluded. One could therefore imagine a scenario of a very light h_f ($m_{h_f} \lesssim 100$ GeV) which eluded the previous searches at the LEP, Tevatron, and LHC experiments.

At the Tevatron, other production mechanisms are available that could allow the discovery of the h_f even in the region where the process $q\bar{q}' \to h_f V$ is suppressed.

1.3 Signature of signal events

We introduce a production process which may offer sizable rates of the h_f even in the region where the coupling $h_f VV$ is very suppressed. We consider [9]

$$q\bar{q}' \to W^* \to h_f H^\pm \, .$$

A quark-antiquark annihilation produces a h_f in association with a $H^\pm$ via an intermediate W boson. This process makes use of the Higgs-Higgs-vector boson coupling,

$$H^\pm h_f W^\pm \sim \sin\beta \, ,$$

in the 2HDM (type I), providing non-negligible cross sections in the large $\tan\beta$ regions. The production cross section is shown in Fig. 2 which is obtained by `PYTHIA` calculations with applying a K factor of 1.4 [10].

We then use the cascade decays

$$H^\pm \to h_f W^*$$

which may have large $\mathcal{B}$'s. The large $\mathcal{B}$ can arise since the coupling of $H^\pm$ to all the fermions scales as

$$H^\pm f f' \sim \frac{1}{\tan\beta} \, ,$$

and thus for moderate to large $\tan\beta$, $\tan\beta = 3$ and 30 as discussed in [9] for example, even the three-body decays (i.e. with V^*) can have sizable or dominant $\mathcal{B}$'s. Moreover, the double h_f production may result in a distinctive 4γ topology and the multi-photon signature should have an advantage of very small background rates. The $\mathcal{B}(H^\pm \to h_f W^*)$ is shown in Fig. 3 which is also created from the `PYTHIA` calculations.

In this study, we perform a search for the fermiophobic Higgs using the $3\gamma + X$ final state emerging from the process

$$p\bar{p} \to h_f H^\pm \to h_f \, (h_f W^*) \to (2\gamma)(2\gamma) + X.$$

In Fig. 4 is shown the cross section

$$\sigma(p\bar{p} \to h_f H^\pm) \times \mathcal{B}(H^\pm \to h_f W^*) \times \left[\mathcal{B}(h_f \to 2\gamma)\right]^2 \, .$$

A Feynman diagram of this process is shown in Fig. 5.

In the past, the DØ collaboration performed this type of analysis using their 0.83 pb^{-1} of data [11]. They found the data consistent with the background expectation and obtained mass limits on the m_{h_f} for benchmark $H^\pm$ mass-points of 100 GeV and 150 GeV assuming $\tan\beta = 3$ and $\tan\beta = 30$. For example,

$$m_{h_f} > 80 \text{ GeV at the } 95\% \text{ C.L.}$$

for $m_{H^\pm} = 100$ GeV and $\tan\beta = 30$.

2 Data Samples and Event Selection

The analysis is based on the data collected from the runs 138425 (February 4, 2002) to 312510 (September 30, 2011) covering the period 0 though 38, and the corrsponding integrated luminosity is 9.2 fb^{-1} after the run filtering for good detector conditions.

The events used in this analysis are required to pass one of the following triggers:

- `DIPHOTON_12`,
- `DIPHOTON_18`,
- `TRIPHOTON`.

The requirements of each trigger are listed in Table 1.

The nominal signature of events by the production mechanism of our interest is the 4γ production but we require 3γ since it is more efficient than the case of detecting all of 4γ and still the background is kept at sufficiently low levels. The 3γ candidate events are selected from the sub-sample of events that pass one of the triggers. In the sample, 3 photons are required to pass the standard photon cut [12] given in Table 2. The "Cut level" and "Base cuts" in the table is explained in §4.1.1. In the case that more than 3 photon-candidates are found in a given event, we sort them from the one with having the largest E_T, then pick up the first 3 photon-candidates for further investigation of kinematics etc.

3 Signal Efficiency and Its Uncertainty

3.1 Signal efficiency

The detection efficiency for signal events must be known in order to measure the signal production cross section. First, the trigger efficiency is taken to be 100% [13] for our combination of triggers and high E_T photons passing the standard photon cuts. The rest of the detection efficiency is estimated as a function of h_f and $H^{\pm}$ masses using the `PYTHIA` MC data, with at least 40000 events for each mass point. The h_f masses range from 10 GeV to 105 GeV at a typical increment of 10 GeV, and from 30 GeV to 300 GeV for the $H^{\pm}$ masses with 5–25 GeV steps. For other parameters, we set $\alpha = \pi/2$ to ensure the fermiophobia ($\cos\alpha = 0$) and $\tan\beta = 10$ to be conservative compared to $\tan\beta = 30$ but still to sufficiently suppress the $h_f VV$ coupling and $H^{\pm}$ decays to fermions. The H^0 and A^0 masses are chosen to be large enough so as not to play in the $H^{\pm}$ decays. We set the H^0 mass = 500 GeV and the A^0 mass = 350 GeV, but there is no strong reason for picking up these particular values. Tables 3–5 are lists of generated mass points (with the dataset ID for the authors record).

The generated events are all passed through the full detector simulation `CDFSIM`. We estimate the efficiency by the following simple fraction:

$$\epsilon = \frac{\text{the number of Higgs-MC events passing the selection cuts}}{\text{the number of generated Higgs-MC events with } 4\gamma}\,, \tag{1}$$

where the denominator events are required to pass a cut on the primary-vertex position along the beamline,

$$|z_{\rm pv}| < 60 \text{ cm} .$$

The efficiency thus includes the geometrical efficiency, the kinematical efficiency, and the efficiency for 3γ passing the photon selection cuts, but does not include the primary-vertex cut efficiency. The absolute efficiency of the primary-vertex cut is estimated in independent dedicated analyses. We use the result from them which is 0.9743. The variables for the photon selection are not perfectly modeled in the `CDFSIM`. This has been studied in detail elsewhere [14]. The MC scale factors have been applied to correct for these effects in the efficiency calculation. Tables 6–8, and Fig. 6 show the signal efficiencies. Typically, the efficiencies are 0.1–1% when the m_{h_f} is smaller than 20 GeV, then rise to 15–20% as the m_{h_f} becomes large. We see from the plot that the efficiencies for the $m_{H^\pm}$ smaller than 50 GeV behave in rather a complicated way in the low m_{h_f} region. In this region, the first W boson created by the s-channel scattering is on-shell. Then the photons, especially from the first h_f from the W decay, get less boosts as the masses of the decay products ($H^\pm$ and h_f) become heavier. As these masses go even larger and the process passes the Breit-Wigner peak of the W boson, the final particles start having larger p_T again simply due to the large masses of the parent particles.

3.2 Systematic uncertainties

As mentioned in §3.1, we take a trigger efficiency of 100% with negligible errors [13]. For the rest of the efficiency, there are a number of effects that can cause the efficiency to be systematically mis-estimated. We identify them and explain how the uncertainties are estimated in the sub-sections below.

3.2.1 Photon selection

We take a systematic uncertainty of 2.7% per photon related to the efficiency for the photon selection [14]. Since there are three photons we take the total systematic uncertainty to be $3 \times 2.7\% = 8.1\%$.

3.2.2 Parton distribution function

When a proton and an anti-proton collide, it is mostly a single sub-particle, a parton (quark or gluon) in the proton or anti-proton, that participates in the hard collision and produces a high center-of-mass energy event. The momentum fraction, described by parton distribution functions (PDFs), that is carried by each of the partons in the proton or anti-proton is not perfectly understood. It affects the kinematics of the outgoing final state particles. To estimate the magnitude of this effect on the detection efficiency we use the standard technique of evaluating, event-by-event, the uncertainty of the probability for a given momentum fraction of the colliding parton

using a standardized "PDF-set" by the CTEQ collaboration (CTEQ-5L) [15]. As only the newer PDF-set version CTEQ-6M contains 90% confidence intervals for each eigenvector, the total uncertainty is estimated using a standard procedure by reweighting the parton momenta of the original CTEQ-5L set and varying the PDFs using the uncertainties from CTEQ-6M as described in [15]. We get a relative uncertainty of 1% on the detection efficiency.

3.2.3 Initial and final state radiation

The initial state radiation (ISR) caused by a gluon radiating from an incoming quark or the final state radiation (FSR) from an outgoing quark can both make the E_T spectrum of the final state particles softer than the case without radiation. The variations of the ISR/FSR thus can cause the photon or the jets to be systematically more or less likely to pass the kinematic requirements. The effect carries a non-negligible theoretical uncertainty and is estimated using the standard CDF procedure as described in [16]. Doing so we find a variation in the detection efficiency, taken to be the systematic uncertainty, of 2%.

3.2.4 Renormalization scale (Q^2)

We include the systematic uncertainty of the efficiency due to variations of the Q^2 scale. The variation observed by changing the scale from $0.25Q^2$ to $4Q^2$ is 3%.

3.2.5 Summary of the systematic uncertainties

The results are summarized in Table 9. All the systematic errors are combined in quadrature to give the total systematic uncertainty of 8.9%. These numbers are estimated for an example mass of $h_f = 50$ GeV and $H^{\pm} = 90$ GeV. We take the systematic uncertainty to be constant for all the masses.

4 Background Estimation

There are two major sources of the background events. The first comes from the events in which jets are mis-identified as photons. The other source is the Direct Triphoton Production (DTP). The contribution arising from detector noises is estimated to be negligible.

4.1 Background with mis-identified photons

QCD backgrounds to the $3\gamma + X$ final state contain at least one electromagnetic-like (EM-like) jets denoted here by j. There are 8 possible combinations of photons and jets: $\{\gamma,\gamma,\gamma\}$, $\{\gamma,\gamma,j\}$, $\{\gamma,j,\gamma\}$, $\{j,\gamma,\gamma\}$, $\{\gamma,j,j\}$, $\{j,\gamma,j\}$, $\{j,j,\gamma\}$, and $\{j,j,j\}$, where the ordering in a combination is determined by the E_T. The 1st component can,

in principle, contain the Higgs signal. The number of 3γ events that are produced can be obtained by solving eight linear equations:

$$\boldsymbol{n} = \boldsymbol{E}\boldsymbol{n}^* \qquad \left(n_i = \sum_{j=1}^{8} E_{ij} n_j^* \,, \quad i = 1, \cdots, 8 \right) \,,$$

or by writing the components explicitly,

$$\begin{pmatrix} n_{ppp} \\ n_{ppf} \\ n_{pfp} \\ n_{fpp} \\ n_{pff} \\ n_{fpf} \\ n_{ffp} \\ n_{fff} \end{pmatrix} = \begin{pmatrix} \epsilon_s\epsilon_s\epsilon_s & \epsilon_s\epsilon_s\epsilon_b & \epsilon_s\epsilon_b\epsilon_s & \epsilon_b\epsilon_s\epsilon_s & \epsilon_s\epsilon_b\epsilon_b & \epsilon_b\epsilon_s\epsilon_b & \epsilon_b\epsilon_b\epsilon_s & \epsilon_b\epsilon_b\epsilon_b \\ \epsilon_s\epsilon_s\bar{\epsilon_s} & \epsilon_s\epsilon_s\bar{\epsilon_b} & \epsilon_s\epsilon_b\bar{\epsilon_s} & \epsilon_b\epsilon_s\bar{\epsilon_s} & \epsilon_s\epsilon_b\bar{\epsilon_b} & \epsilon_b\epsilon_s\bar{\epsilon_b} & \epsilon_b\epsilon_b\bar{\epsilon_s} & \epsilon_b\epsilon_b\bar{\epsilon_b} \\ \epsilon_s\bar{\epsilon_s}\epsilon_s & \epsilon_s\bar{\epsilon_s}\epsilon_b & \epsilon_s\bar{\epsilon_b}\epsilon_s & \epsilon_b\bar{\epsilon_s}\epsilon_s & \epsilon_s\bar{\epsilon_b}\epsilon_b & \epsilon_b\bar{\epsilon_s}\epsilon_b & \epsilon_b\bar{\epsilon_b}\epsilon_s & \epsilon_b\bar{\epsilon_b}\epsilon_b \\ \bar{\epsilon_s}\epsilon_s\epsilon_s & \bar{\epsilon_s}\epsilon_s\epsilon_b & \bar{\epsilon_s}\epsilon_b\epsilon_s & \bar{\epsilon_b}\epsilon_s\epsilon_s & \bar{\epsilon_s}\epsilon_b\epsilon_b & \bar{\epsilon_b}\epsilon_s\epsilon_b & \bar{\epsilon_b}\epsilon_b\epsilon_s & \bar{\epsilon_b}\epsilon_b\epsilon_b \\ \epsilon_s\bar{\epsilon_s}\bar{\epsilon_s} & \epsilon_s\bar{\epsilon_s}\bar{\epsilon_b} & \epsilon_s\bar{\epsilon_b}\bar{\epsilon_s} & \epsilon_b\bar{\epsilon_s}\bar{\epsilon_s} & \epsilon_s\bar{\epsilon_b}\bar{\epsilon_b} & \epsilon_b\bar{\epsilon_s}\bar{\epsilon_b} & \epsilon_b\bar{\epsilon_b}\bar{\epsilon_s} & \epsilon_b\bar{\epsilon_b}\bar{\epsilon_b} \\ \bar{\epsilon_s}\epsilon_s\bar{\epsilon_s} & \bar{\epsilon_s}\epsilon_s\bar{\epsilon_b} & \bar{\epsilon_s}\epsilon_b\bar{\epsilon_s} & \bar{\epsilon_b}\epsilon_s\bar{\epsilon_s} & \bar{\epsilon_s}\epsilon_b\bar{\epsilon_b} & \bar{\epsilon_b}\epsilon_s\bar{\epsilon_b} & \bar{\epsilon_b}\epsilon_b\bar{\epsilon_s} & \bar{\epsilon_b}\epsilon_b\bar{\epsilon_b} \\ \bar{\epsilon_s}\bar{\epsilon_s}\epsilon_s & \bar{\epsilon_s}\bar{\epsilon_s}\epsilon_b & \bar{\epsilon_s}\bar{\epsilon_b}\epsilon_s & \bar{\epsilon_b}\bar{\epsilon_s}\epsilon_s & \bar{\epsilon_s}\bar{\epsilon_b}\epsilon_b & \bar{\epsilon_b}\bar{\epsilon_s}\epsilon_b & \bar{\epsilon_b}\bar{\epsilon_b}\epsilon_s & \bar{\epsilon_b}\bar{\epsilon_b}\epsilon_b \\ \bar{\epsilon_s}\bar{\epsilon_s}\bar{\epsilon_s} & \bar{\epsilon_s}\bar{\epsilon_s}\bar{\epsilon_b} & \bar{\epsilon_s}\bar{\epsilon_b}\bar{\epsilon_s} & \bar{\epsilon_b}\bar{\epsilon_s}\bar{\epsilon_s} & \bar{\epsilon_s}\bar{\epsilon_b}\bar{\epsilon_b} & \bar{\epsilon_b}\bar{\epsilon_s}\bar{\epsilon_b} & \bar{\epsilon_b}\bar{\epsilon_b}\bar{\epsilon_s} & \bar{\epsilon_b}\bar{\epsilon_b}\bar{\epsilon_b} \end{pmatrix} \begin{pmatrix} n^*_{\gamma\gamma\gamma} \\ n^*_{\gamma\gamma j} \\ n^*_{\gamma j\gamma} \\ n^*_{j\gamma\gamma} \\ n^*_{\gamma jj} \\ n^*_{j\gamma j} \\ n^*_{jj\gamma} \\ n^*_{jjj} \end{pmatrix} ,$$

where the

$$\boldsymbol{n} = \begin{pmatrix} n_{ppp} \\ n_{ppf} \\ n_{pfp} \\ n_{fpp} \\ n_{pff} \\ n_{fpf} \\ n_{ffp} \\ n_{fff} \end{pmatrix}$$

denotes a vector of observed events (p = passing, f = failing the photon selection) and the

$$\boldsymbol{n}^* = \begin{pmatrix} n^*_{\gamma\gamma\gamma} \\ n^*_{\gamma\gamma j} \\ n^*_{\gamma j\gamma} \\ n^*_{j\gamma\gamma} \\ n^*_{\gamma jj} \\ n^*_{j\gamma j} \\ n^*_{jj\gamma} \\ n^*_{jjj} \end{pmatrix}$$

denotes produced events. The $\boldsymbol{E}$ ($E_{ij},\ i,j = 1, \cdots, 8$) is an 8×8 efficiency matrix, where the signal and background efficiencies ($\epsilon_s,\ \epsilon_b$) are the probability of a photon and jet to pass the photon selection, and

$$\bar{\epsilon_s} \equiv 1 - \epsilon_s \,, \qquad \bar{\epsilon_b} \equiv 1 - \epsilon_b \,.$$

The E_T dependence of the ϵ_s is neglected, while we take into account of it for the ϵ_b.

4.1.1 Rate of jets faking photons

We estimate the rate at which a jet originating from a quark or a gluon fakes an isolated photon in the central calorimeter (CEM) to apply it as the ϵ_b in the efficiency matrix ($\boldsymbol{E}$). We call any photon that is due to the decay of a meson (e.g. $\pi^0/\eta^0 \to 2\gamma$) as "fake photons", whereas prompt photons via direct production or radiated off a quark make up the "true photon" signal. Our analysis technique basically follows the one as described in [17].

Raw fake-rates

Our analysis starts by measuring the raw jet-to-photon fake rate, which is simply the fraction of jets passing the standard photon cut in §2, for isolated jets found in a sample of jet-triggered events. The "raw" means that the selected photon candidates are a mixture of mis-identified hadronic quark/gluon showers and prompt photons. The raw fake-rate thus can be expressed by

$$P_{\rm raw} = \frac{N_\gamma^{\rm cand}}{N_j} = \frac{N_\gamma^{\rm true} + N_{j\to\gamma}}{N_j}$$

and it represents an upper limit on the actual fake-rate since it is contaminated by true photons $N_\gamma^{\rm true}$.

We use jets from the `JET20, JET50, JET70,` and `JET100` triggered datasets, filtered by the electron/muon no-silicon good-run list of the version called `higgs.` These datasets, which range from the runs 138425 to 312510, have a 9.7 fb^{-1} of integrated luminosity. We filter these QCD events by requiring that the ΔR separation between every pair of jets is at least 0.4. The jets are further sub-divided into three groups from the highest to the lowest jet E_T. They are the 1st jet, 2nd jet, and "3 or more jets". Note that the energy ranking uses all jets before any further cuts are made on the datasets. We choose the "3 or more jets" in order to avoid possible biases by the jet triggers especially on the E_T, and it is referred to as the probe jets. The probe jets are required to satisfy $E_T > 15$ GeV and $|\eta| < 1.1$ to be considered for the raw fake-rate measurement. The selection up to this point is denoted by the "Cut level" = 0 in Table 2.

Having determined the QCD jet sample, we search in each event for the closest matching EM object to the selected jet. If the separation is $\Delta R < 0.4$, we accept the EM object as a candidate for faking a photon. We then require the cuts indicated by the Cut level = 1 in Table 2, and these probe jets serve as denominator objects. The η and E_T cuts are actually re-applied in terms of the EM object variables. In this sense, the Cut level is something more like Cut level ≤ 1. The "Base cuts" in the table marks the cuts that are applied to collect these denominator objects, starting from the jet selection. Finally we apply all the photon selection cuts listed in Table 2, that is the Cut level ≤ 5, to the matched EM objects to determine the number that would be accepted as central photons. Figure 7 shows this raw fake-rate as a function of jet E_T, combining the `JET20` to `JET100` dataset, with statistical errors.

As a measure of the systematic errors we perform separate analyses using the different jet datasets. We take the difference of the fake rates measured from these datasets as a systematic error. The variation among the different jet datasets is shown in Fig. 8, which is approximately 5–15% over the E_T range being looked at.

Correction for true-photon contamination

The jet samples used to measured the raw fake-rate contain "true" photons from direct production or bremsstrahlung radiation. The true photons have a high probability to pass the photon selection and thus increase the measured fake rate. A correction factor,

$$F_{\rm QCD} = \frac{N_{j\to\gamma}}{N_\gamma^{\rm cand}} = \frac{N_{j\to\gamma}}{N_\gamma^{\rm true} + N_{j\to\gamma}} \,,$$

which estimates the fraction of actual jets that are in our fake-rate sample, is applied to the raw fake-rate to correct for prompt-photon contamination and to obtain the "true" fake-rate $P_{\rm true}$ that is applied as the ϵ_b in the efficiency matrix.

Correcting the raw fake-rate for prompt-photon contamination must be accomplished by statistical methods because the particle-by-particle identification is not possible. We use the isolation vs. CES-χ^2 method to determine the $F_{\rm QCD}$. In a 2-dimensional distribution of the calorimeter isolation variable and CES-χ^2, signal events congregate in the low isolation and low χ^2 region, while background events have large isolation energy due to hadronic activity. The 2-dimensional plane can be divided into four regions (see Table 10), where the region C is the signal region and the region D is entirely background. Assuming no correlation between the isolation energy and CES-χ^2 for background events, the background in the region C can be determined by

$$\frac{N_{\rm C}^{BG}}{N_{\rm A}} = \frac{N_{\rm B}}{N_{\rm D}} \,.$$

Then we obtain

$$F_{\rm QCD} = \frac{N_{\rm C}^{BG}}{N_{\rm C}} = \frac{N_{\rm B} N_{\rm A}}{N_{\rm D} N_{\rm C}} \,.$$

Figure 9 shows the result of the $F_{\rm QCD}$ measurement as a function of jet E_T. The data suggest that the true-photon contamination is small at lower energies and large at higher energies.

We take the difference of the $F_{\rm QCD}$ measured by using the different jet datasets as the systematic error. These $F_{\rm QCD}$ values are shown in Fig. 10.

True fake-rates

The "true" fake rate for the QCD sample is obtained by

$$P_{\rm true} = \frac{N_{j\to\gamma}}{N_j} = \frac{N_\gamma^{\rm cand}}{N_j} \times \frac{N_{j\to\gamma}}{N_\gamma^{\rm cand}} = P_{\rm raw} \times F_{\rm QCD} \,,$$

which is shown in Fig. 11.

4.1.2 Photon efficiency

We estimate the probability of a photon to pass the standard photon selection in §2 to use it as the ϵ_s in the efficiency matrix. Because a pure sample of photons in the detector data is unavailable, the photon efficiency is estimated using efficiencies for electrons by assuming that electrons and photons behave similarly in the detector. Our analysis technique follows the one as described in [14]. Here we deal with the photon efficiency itself just for obtaining the efficiency matrix, rather than discussing the scale factors to MC efficiencies.

The high-p_T electron trigger (`CENTRAL_ELECTRON_18`) is used to collect data from all the available datasets, `bhel0d` through `bhel0p`. The runs are required to be marked good for electrons/muons, no-silicon situation, and be included in the good run list version `higgs`. The corresponding integrated luminosity is 9.6 fb^{-1}.

The process $Z \to ee$ is selected to define a pure sample of electrons. All $Z \to ee$ events are the central-central data. We apply the cuts listed in Table 11 to both central electrons. Each event is required to have an electron passing all the cuts, referred to as the tight cuts, and another passing the Base cuts as indicated in the table, where these cuts correspond to the electron version of the cuts at the same Cut-levels for photons in Table 2. We then look at their invariant mass distributions. The signal is assumed to take the form of a double-Gaussian distribution, while the background is taken to be the 3rd-degree polynomial. By fitting the sum of these two functions to data, we fix the parameters of the Gaussian functions. The number of signal events is then estimated by integrating the Gaussian functions. After the number of events passing the cuts is calculated, the efficiency for these events can be determined. Figure 12 shows example plots for the Z counting.

In the case of two central electrons, the analysis creates a statistical bias because of the initial requirement of at least one tight electron in the central detector. As one tight central electron has already been required, the probability that the second central electron will pass the tight cuts is lower due to the two possible combinations of the tight and the Base-cut pair. To reconcile this bias, the central-central efficiency equation must be modified. The equation used is

$$\epsilon = \frac{N_{TT} + N_{TT}}{N_{TB} + N_{TT}} \,,$$

where the N_{TT} is the number of events with both legs passing all the tight cuts and the N_{TB} is the number of events with a tight leg and another leg passing at least the Base cuts. Table 12 shows the efficiencies for the standard photon selection with statistical errors.

4.1.3 Calculation of fake event

The observed numbers of events $\boldsymbol{n}$ are related to the objects passing or failing the standard photon cut of Table 2. The jet objects with $E_T > 15$ GeV and $|\eta| < 1.1$ are considered in the photon sample explained in §2. They must have a matched EM object passing the Base cuts. If there are more than 3 such objects in a given event, we pick up the 3 objects from the highest E_T. We then examine whether these EM objects pass the photon selection or not. The n_{ppp} is the number of observed events which have 3 denominator objects passing the standard photon cut, the n_{ppf} is the number of observed events which have 2 objects passing standard photon cut and 1 object failing, and the same can be said for others. Note that the n_{ppp} is the number of candidate events which are passing all the cuts, thus our analysis scheme does not allow a blind search.

The efficiency matrix $\boldsymbol{E}$ includes the ϵ_b which is the E_T dependent probability of a jet faking a photon. We take this event-by-event variation of the efficiency matrix by performing the matrix inversion for each event i, namely,

$$\boldsymbol{n}^* = \sum_i^{\text{events}} \boldsymbol{E}_i^{-1} \boldsymbol{e}_i \,,$$

where the $\boldsymbol{e}_i$ is the basic vector of the pass-fail representation. For example, if a given event is classified as ppf, then

$$\boldsymbol{e}_i = \begin{pmatrix} 0 \\ 1 \\ 0 \\ 0 \\ 0 \\ 0 \\ 0 \end{pmatrix} ,$$

and so on.

The number of the QCD contribution from $\{\gamma,\gamma,j\}$, $\{\gamma,j,\gamma\}$, $\{j,\gamma,\gamma\}$ $\{\gamma,j,j\}$, $\{j,\gamma,j\}$, $\{j,j,\gamma\}$, and $\{j,j,j\}$, is estimated by the following equation,

$$\begin{aligned} n_{\text{fake}}^{3\gamma} &= \epsilon_s^2\epsilon_b \times n^*_{\gamma\gamma j} + \epsilon_s\epsilon_b\epsilon_s \times n^*_{\gamma j\gamma} + \epsilon_b\epsilon_s^2 \times n^*_{j\gamma\gamma} + \epsilon_s\epsilon_b\epsilon_b \times n^*_{\gamma jj} \\ &+ \epsilon_b\epsilon_s\epsilon_b \times n^*_{j\gamma j} + \epsilon_b\epsilon_b\epsilon_s \times n^*_{jj\gamma} + \epsilon_b\epsilon_b\epsilon_b \times n^*_{jjj} \,. \end{aligned}$$

If we actually perform the calculation, we find the result to be 4.3 ± 0.4(stat). We will not, however, use this number as we will try to improve the estimation in the following section.

4.1.4 Introducing the loose cuts

The base formalism of estimating the fake-photon backgrounds has been given in §4.1.3, which is in principle a statistical method. It is therefore important to have reasonably sufficient number of observed events as the input for the calculation.

Our fake-photon background estimation is performed not only for the counting but also for checking various distributions. The statistical power then become more important for stable predictions bin-by-bin.

From these considerations, we loosen the cuts for the 3rd object to allow more events come in the input sample. We accept just jet objects in the central region with $E_T > 15$ GeV. These cuts are indicated by the Cut level = 0 in in Table 2. Before introducing the loose cut, the input number of events is

$$\boldsymbol{n} = \begin{pmatrix} n_{ppp} \\ n_{ppf} \\ n_{pfp} \\ n_{fpp} \\ n_{pff} \\ n_{fpf} \\ n_{ffp} \\ n_{fff} \end{pmatrix} = \begin{pmatrix} 10 \\ 27 \\ 51 \\ 60 \\ 152 \\ 176 \\ 440 \\ 1681 \end{pmatrix} ,$$

which changes to

$$\begin{pmatrix} 10 \\ 2639 \\ 45 \\ 47 \\ 5627 \\ 7118 \\ 387 \\ 38618 \end{pmatrix}$$

by applying the loose cut for the 3rd object.

The fake rates corresponding to the loose denominator objects must be measured. The corresponding raw fake-rates ($P'_{\rm raw}$) are shown in Fig. 13, and the true fake-rates ($P'_{\rm true}$) are shown in Fig. 14. Figure 15 shows the invariant mass distributions for measuring the photon efficiency corresponding to the loose denominator cuts (ϵ'_s) and the results are listed in Table 13. The $P'_{\rm true}$ and ϵ'_s replace the ϵ_b and ϵ_s for the 3rd object in the efficiency matrix $\boldsymbol{E}$, respectively. For example, the $E_{11} = \epsilon_s\epsilon_s\epsilon_s$ is changed to $E_{11} = \epsilon_s\epsilon_s\epsilon'_s$ and the $E_{15} = \epsilon_s\epsilon_b\epsilon_b$ is changed to $E_{15} = \epsilon_s\epsilon_b\epsilon'_b$.

By executing the calculation, the number of fake-photon background is estimated to be

$$n^{3\gamma}_{\rm fake} = 2.99 \pm 0.23({\rm stat}) \, .$$

This is also consistent with the result by the first method (4.3 ± 0.4) and will be used as the final number in our analysis. The systematic uncertainties of the result is discussed in the next section.

4.1.5 Systematic uncertainties

The systematic uncertainty on the number of fake events includes the uncertainties originating from the photon efficiency and the jet-to-photon fake rate. We take an uncertainty of 2.7% for the photon efficiency per photon as described in [14]. The contribution of this input uncertainty to the output number of fake events after applying our background-estimation method is found to be 0.2%. As the uncertainties of the input fake rates, we use the uncertainties shown in Fig. 11. The plot shows the statistical and systematic uncertainties separately but the combined uncertainties of these fake rates are considered to be the source of the systematic uncertainty here. We find that it results in the uncertainty of 19% of the estimated number of fake-backgrounds.

We consider another source of the systematic uncertainty which is related to the sample dependence of the fake rates. The probability of a jet faking a photon depends on the fragmentation process of the quark or gluon that the jet is originating from. For example, the fragmentation producing a single neutral pion should have higher probabilities than the general cases. Then the fragmentation is basically different between quarks and gluons, which means that the fake rates are sensitive to the composition of quarks and gluons in the sample. We measure the fake rates in the gneric jet samples, while we apply them to events containing 3 objects of different combination of types such as $\{\gamma, j, j\}$, $\{j, \gamma, j\}$, $\{j, j, j\}$, and so on. The quark-gluon compositions could be largely different among them which would lead to errors of the estimated number of fake backgrounds.

In order to take this effect into account of, we take a conservative approach rather than evaluating details such as the quark-gluon composition of the samples, which in fact turns out sufficient for our analysis. We assume that our fake rates obtained from the generic samples correspond to the 50%-50% mixture of quarks and gluons. We may say that this is equivalent to, from the Bayesian viewpoint, assuming that we do not have any information regarding the composition. Furthermore, we assume that the fake rates for gluon jets and quark jets differ by as much as 50%. From these, the fake rates are controlled by a single parameter, the quark fraction in the sample, f_q, that is

$$\epsilon_b^* = \epsilon_b \cdot (f_q + 0.5) \, ,$$

where the ϵ_b^* represents the unknown true fake-rate properly reflecting the quark-gluon composition of a given sub-sample of the photon events. We then generate f_q values uniformly in the range between 0 and 1, and repeat the calculation of the number of expected fake-photon backgrounds. In doing this, we use different f_q values for each of the type-combination, $\{j, j, j\}$, $\{\gamma, j, j\}$, $\{j, \gamma, j\}$, and so on. By this, we introduce the sample dependence of the fake rates, and at the same time, the correlation among the efficiency matrix elements is embedded in the evaluation. For example, the $\{j, j, j\}$ contributes to the $\{p, p, p\}$ through $E_{18} = \epsilon_b^* \epsilon_b^* \epsilon_b^*$ and $\{p, p, f\}$ through $E_{28} = \epsilon_b^* \epsilon_b^* (1 - \epsilon_b^*)$, thus the E_{18} and E_{28} are correlated.

We generate 1000 trials and look at the variation of the estimated number of fake-photon backgrounds. The result is shown in Fig. 16. The level of the variation is found to be 37%.

Adding all the systematic uncertainties in quadrature, the total systematic uncertainty is estimated to be 41%. As a summary, the fake-photon background we quote is

$$n_{\rm fake}^{3\gamma} = 3.0 \pm 0.2({\rm stat}) \pm 1.2({\rm syst}) \, .$$

4.2 Direct triphoton background

4.2.1 Monte Carlo data

We estimate the DTP background by using MC data based on the `MadGraph/MadEvent` (version 4) + `PYTHIA` parton-shower event generation. The `MadGraph/MadEvent` provides exact treetments of tree-level matrix elements for the DTP events. The number of jets allowed in one event at the `MadGraph/MadEvent` generation is 0–2. The 0-jet event corresponds to the LO tree-level process

$$q\bar{q} \to 3\gamma \, ,$$

and the 1-jet event is the NLO tree-level processes

$$q\bar{q} \to (3\gamma)g \, , \qquad qg \to (3\gamma)q \, , \qquad \bar{q}g \to (3\gamma)\bar{q} \, ,$$

then the 2-jet event consists of the NNLO tree-level processes

$$q\bar{q} \to (3\gamma)gg \, , \qquad qg \to (3\gamma)qg \, , \qquad \bar{q}g \to (3\gamma)\bar{q}g \, , \qquad gg \to (3\gamma)q\bar{q} \, .$$

We perform the so-called MLM matching between the matrix-element calculation and parton showering in order to remove double counting regarding the jet production. The parameter in the `MadGraph/MadEvent` to control the matching is named `xqcut` and we set `xqcut`$= 5$ to realize smooth distributions of the differential jet rate.

The data are created by ourselves for this study. The number of generated events is about 2.6 M events (correponding to about 19 ab^{-1}) which are passed through our full detector-simulation. We pick up prompt photons by looking at the `HEPG` and `OBSP` information, then after the same photon selection as we apply for the real data, we are left with 13949 DTP events.

We then proceed with the estimation of the DTP incorporating the scale factors for the photon selection efficiency, and the number of expected events is found to be

$$n_{\rm DTP}^{3\gamma} = 6.906 \pm 0.058({\rm stat}) \, .$$

4.2.2 Comparison with the `MCFM`

We look at some aspects of the cross-section calculation by comparing the `MadGraph` with another matrix-element calculation tool called the `MCFM` (version 6.8). It provides a theoretical calculation of the full NLO cross section, including loop diagrams, which has been made available recently [18]. With a certain kinematical constraints

on the parton-level final-states which is consistent with our analysis, the result of the cross-section calculation is summarized in Table 14. The LO cross-section by the MadGraph/MadEvent is 2.617 fb, and the same LO cross-section by the MCFM is 2.787 fb. The difference is 6.5%. The NLO cross-section without loop diagrams by the MadGraph/MadEvent is 4.911 fb, while the full NLO cross-section by the MCFM is found to be 4.667 fb. The K factors are

$$K_{\texttt{MG/ME}} = \frac{4.911}{2.617} = 1.877\,, \qquad K_{\texttt{MCFM}} = \frac{4.667}{2.787} = 1.675\,,$$

respectivly. The loop effect could be then quantified by

$$\frac{1.675}{1.877} = 0.892\,.$$

One thing to be noted is that the MadGraph/MadEvent predicts rather large contributions from 2-jet events, which is

$$\frac{6.840}{4.911} = 1.393\,.$$

The overall difference between the MadGraph/MadEvent and the MCFM is as much as

$$\frac{4.667}{6.840} = 0.682 \qquad \text{or} \qquad 32\% \text{ difference}\,.$$

4.2.3 Systematic uncertainties

The systematic uncertainty of the number of DTP events originating from the normalization is estimated to be 7.2% by changing the renormalization scale in the range between $0.5M_{3\gamma}$ and $2M_{3\gamma}$. We also quote 32% related to the normalization systematics by conservativly taking the difference of the cross sections between the MadGraph/MadEvent and the MCFM calculations. We take 1.1% for the matching uncertainty which is estimated by changing the xqcut parameter by ± 1. For the systematic uncertainties from the PDF and ISR/FSR, we follow the standard procedure at CDF. The systematic uncertainty from the PDF is found to be 1.2%, and the uncertainty from the ISR/FSR is 5.7%. The uncertainty from the photon efficiencies is $3 \times 2.7\% = 8.1\%$. Finally, the uncertainty due to the luminosity is 6% with major contributions from the uncertainties on the CLC efficiency, the detector simulation, and the event generator [19].

Adding these uncertainties in quadrature, we obtain the total systematic uncertainty of 35%. The estimated number of DTP events is then given by

$$n^{3\gamma}_{\rm DTP} = 6.9 \pm 0.1(\text{stat}) \pm 2.4(\text{syst})\,.$$

4.3 Electroweak processes

We investigate the contributions from electroweak processes using the MC data with calibrating them by real data as much as possible.

4.3.1 $Z(\rightarrow ee)\gamma$

We start from confirming Z peaks for events with 2 EM objects by turning off the cuts requiring the existence of the associated track, which are shown in Fig. 17. We measure the probability of electrons failing to have good tracks using these Z peaks by the same method in §4.1.2, and find it to be

$$\text{Trackless probability} = (1.991 \pm 0.044)\% \,.$$

We next look at events with 3 EM objects. Figure 18 compares the invariant mass distributions between the real data and MC data (`rewk33)`, where the track cuts are turned off for the two leading EM objects, while the 3rd EM object is required to have no associated track (2 EM + 1 Trackless events). The MC data reproduce the data well including the normalization. We then simply apply all the selection cuts to the MC data and obtain the distribution of $E_T^{\gamma_1} + E_T^{\gamma_2}$, the sum of E_T of the 1st and 2nd leading photon candidates, as shown in Fig. 19. This parameter $E_T^{\gamma_1} + E_T^{\gamma_2}$ is chosen here since it is used to define the final search region as explained in §5. The event yield for the MC data is found to be 0.46 ± 0.12 events.

In order to gain statistics and more robust predictions of kinematical distributions for the final MC events, we rescale the 2 EM + 1 Trackless events with the probability of electrons failing to have good tracks. By multiplying the probability, 1.991%, twice for these events, we obtain the $E_T^{\gamma_1} + E_T^{\gamma_2}$ distributions shown in Fig. 20. The number of events is

$$0.1676 \pm 0.0015 \,.$$

In any cases, the contribution from the $Z(\rightarrow ee)\gamma$ events is expected to be small.

4.3.2 $W(\rightarrow e\nu)\gamma$

We look at missing E_T ($\not\!\!E_T$) distributions to locate W events in the real data to normalize MC data. Figure 21 shows the $\not\!\!E_T$ distributions for events with 2 EM objects found in the real data and MC data (`rewk28)`. The track cut is turned off for the leading EM object, while the 2nd leading EM object is required to be trackless. The real data are fit with the MC prediction of the shape and an empirical function of the form $p_0 {\not\!\!E_T}^{-p_1}$ to model the non-W events, where the p_0 and p_1 are the fitting parameters for the non-W component. The MC data reproduces the W bump observed in the data well. The fit results in the MC normalization of

$$(15.55 \pm 0.99) \times 10^2 \text{ events} \,,$$

and the corresponding rescaling factor with respect to the MC luminosity is calculated to be

$$0.521 \pm 0.032 \,.$$

It would be nice to measure the probability of electrons to be reconstructed as trackless objects using the W bump in the data but it turns out that we cannot

confirm it as shown in Fig. 22, where both EM objects are required to be trackless. The fit returns zero-consistent W contribution. Given this, we compromise to estimate the probability simply using the MC data. Figure 23 shows the event reduction by requiring the leading EM object to be trackless. The probability is found to be

$$\text{Trackless probability} = (3.51 \pm 0.27)\% \,.$$

which is a similar level of value found for the $Z(\rightarrow ee)\gamma$ events in the real data.

We now turn to the events with 3 EM objects by requiring the 3rd EM object that is trackless in a given event. We find that only 2 events are left out of 4839 MC events as shown in Fig. 24. We take this to be the probability of finding another trackless EM object in the $W(\rightarrow e\nu)\gamma$ events. Then starting from the 1 EM + 1 Trackless events normalized to the data, our simple estimation is given by

$$(15.55 \times 10^2) \times \frac{3.51}{100} \times \frac{2}{4839} = (2.500 \pm 0.036) \times 10^{-2} \text{ events} \,,$$

where the error is statistical. The distibutions can be obtained by rescaling the MC events with 1 EM + 1 Trackless objects. The $E_T^{\gamma_1} + E_T^{\gamma_2}$ distibution as an example is shown in Fig. 25.

4.3.3 $Z(\rightarrow\tau\tau)\gamma$

It requires significant efforts to confirm this process in data for the MC normalization. We simply apply our selection cuts to full simulation data and use the MC luminosity for the normalization. The $E_T^{\gamma_1} + E_T^{\gamma_2}$ distribution is shown in Fig. 26. The number of expected event is

$$(0.256 \pm 0.060) \text{ events} \,.$$

4.3.4 $W(\rightarrow\tau\nu)\gamma$

Since this process is also difficult for the MC normalization, we just use the MC luminosity, which is about 470 fb^{-1}(`rewk6a`). After applying all the selection cuts, there is no event left. By taking a simple limit on the event yield at the 95% confidence level (C.L.), 3 events, it translates into

$$< 0.059 \text{ @ } 95\% \text{ C.L.} \,.$$

4.3.5 Summary of the electroweak backgrounds

Table 15 is a summary of the electroweak background estimation with statistical errors only. As the systematic error, we conservatively quote 71% which is the statistical error of 2 events found in estimating the probability of finding an extra photon-like object in the $W(\rightarrow e\nu)\gamma$ MC data. The systematic errors from the PDFs, Q^2, etc. are

typically less than 10% and we do not expect any larger relative systematic errors than the value we quote here. The expected total number of events is then

$$n^{3\gamma}_{\rm EWK} = 0.45 \pm 0.06({\rm stat}) \pm 0.32({\rm syst})$$

with omitting the contribution from $W(\to\tau\nu)\gamma$.

4.4 Summary of background estimation

The total background to the $3\gamma + X$ final state is estimated by the sum of $n^{3\gamma}_{\rm fake}$, $n^{3\gamma}_{\rm DTP}$, and $n^{3\gamma}_{\rm EWK}$. Table 16 summarizes the systematic errors for the event counting and Table 17 shows the estimated total background events with statistical and systematic errors. The number of events found in the data is also included in the table. After considering all the backgrounds, the expected E_T distributions for 3γ events are shown in Fig. 27. Here we are comparing the background distribution and the expected signal for an example mass of $h_f = 75$ GeV and mass of $H^\pm = 120$ GeV. The $W(\to e\nu)\gamma$ process is not included for some particular plots because the MC data do not have the 3rd object. The plot also includes the total error for the expected background estimation. The components of systematic errors considered in the plot are listed in Table 18. When the background contributions are added, 100% correlation is assumed for the same error sources for a given bin. Figure 28 shows the distribution of $E_T^{\gamma_1} + E_T^{\gamma_2}$. We see good agreements between the expected and observed 3γ events.

5 Optimization

5.1 Optimization and expected limits

Now that the background estimation methods are determined and the signal efficiency is available, along with their uncertainties, an optimization procedure can be employed.

We choose to optimize the $E_T^{\gamma_1} + E_T^{\gamma_2}$ cut. Let us recall that the signal event has four photons, and two jets or a lepton from a W boson. Each object is quite energetic carrying on average 10–20 GeV of energy in the transverse plane. Thus the h_f signal has a large $E_T^{\gamma_1} + E_T^{\gamma_2}$ compared to the SM backgrounds which are dominated by the fake and DTP backgrounds (see Fig. 28).

As a measure of our search sensitivity, we use 95% C.L. expected cross section limits, under the no-signal assumption, then find an optimal cut. We use the Bayesian limit calculation [20] to obtain the limits, taking into account of the signal efficiency, the predicted number of background events, the luminosity, and their systematic uncertainties as well as the theoretical uncertainty of the cross section. The electroweak backgrounds are not included in this optimization since their contributions are small.

The systematic uncertainty of the signal efficiency is 8.9% as discussed in §3.2. We take 20% as the theoretical uncertainty on the prediction of production cross section for signals [21]. The systematic unertainty of the luminosity is taken to be 6%. These systematic uncertainties on the number of signal events are already included in Table 16.

The systematic uncertainty of the backgrounds is determined from our understanding of fake events and DTP events, as described in §4.

The predicted number of background events and the efficiency are a function of cut choice, so the expected cross section limit is also a function of cut value ($30 \leq E_T^{\gamma_1} + E_T^{\gamma_2} \leq 125$ GeV in steps of 1 GeV). For each combination of the h_f and $H^{\pm}$ masses, the minimum expected cross section limit defines our optimal cut. The mass exclusion is given by the region where the theoretical cross section is above the 95% C.L. cross section limit. As an example of $E_T^{\gamma_1} + E_T^{\gamma_2} > 90$ GeV, Fig. 29 shows the 95% C.L. limits on the cross-section ratios with respect to the theory. In this case the excluded region is $m_{h_f} < 76$ GeV for $H^{\pm} = 90$ GeV. We choose the $E_T^{\gamma_1} + E_T^{\gamma_2}$ cut making the excluded region wide. Figure 30 shows the h_f mass limit for each mass of $H^{\pm}$ as a function of cut value. We choose $E_T^{\gamma_1} + E_T^{\gamma_2} > 90$ GeV as this cut reasonably maximizes and stabilizes the mass limit. Figure 31 shows the $E_T^{\gamma_1} + E_T^{\gamma_2}$ distribution with the final signal region indicated and Fig. 32 shows the cumulative distribution of the $E_T^{\gamma_1} + E_T^{\gamma_2}$.

5.2 Final search region

With the final cut of $E_T^{\gamma_1} + E_T^{\gamma_2} > 90$ GeV, we predict 2.96 ± 0.94 background events with 0.32 ± 0.16 of fake events, 2.60 ± 0.93 of DTP events, and 0.04 ± 0.03 of electroweak processes. Table 19 shows the expected number of background events and the number of events found in the data. Figures 33–37 show various distributions in the final 3γ events. Event displays for the 5 candidate events found in the data are shown in Figs. 38–42.

One may be curious about the staistical significance of the upward fluctuation of the observed data that we see, for example, in the bottom plot of Fig. 34. At the bin of $E_T^{\gamma_1} + E_T^{\gamma_2} + E_T^{\gamma_3} = 340$ GeV, we observe two events while the background expectation is 0.036 ± 0.014. The significance is derived from the so-called p value. The p-value calculation is performed in the framework of the prior-predictive method [22], i.e. the observed number of events is modeled by the Poisson statistics multiplied by the background prior with integrating nuisance parameters out. We use the truncated Gaussian as the background prior, then the probability density function (PDF) of the observed number of events is given by

$$\mathcal{P}(n|B, \Delta B) = \int_0^{+\infty} db \frac{e^{-b} b^n}{n!} \tilde{G}(b|B, \Delta B) \,, \tag{2}$$

where $\tilde{G}(b|B, \Delta B)$ represents a truncated Gaussian with the mean B and the sigma ΔB. When the observed number of events is given by n_0, we compute the p value with the test statistic n by

$$p = \sum_{n=n_0}^{+\infty} \mathcal{P}(n|B, \Delta B) \,. \tag{3}$$

Then, we use one-sided conversion of the p value to the sigma s:

$$p = 1 - \mathrm{Freq}(s)\ , \tag{4}$$

where the $\mathrm{Freq}(x)$ is the frequency function defined by

$$\mathrm{Freq}(x) \equiv \frac{1}{\sqrt{2\pi}} \int_{-\infty}^{x} dt\ e^{-\frac{t^2}{2}}\ . \tag{5}$$

By performing this exercise for the point in Fig. 34, we find the significance of 3.2σ. If we integrate the number of expected backgrounds from this bin to those in the higher region, we find the significance of 2.3σ, while it is 0.7σ if we integrate the number of expected backgrounds from the bin next to the 2nd highest observed event at 180 GeV.

6 Analysis Checks

6.1 Pilot regions

Before going to the final result, we define some categories of events in which the signal events are minimized to confirm consistency between our background expectations and the observed data. We call it here the "pilot regions" since signal events could still contribute to the regions and they are not completely controlled.

The first type of events we consider are the sum of n_{ppf}, n_{pfp}, and n_{fpp} categories. What we have to do is just to extend the fake-background estimation already done for the n_{ppp} component to others. This check is, however, not really powerful when the contributions from real-photons $n^*_{\gamma\gamma\gamma}$ are small, because all the observed contributions are automatically attributed to fake backgrounds in the efficiency-matrix method. It therefore provides a general check of our machinery, such as the matrix inversion, used to estimate the background. We repeat the fake and DTP background estimation for each component, which is listed in Table 20, where the electroweak backgrounds are not included since they are expected to be negligibly small. Figure 43 shows the result in the plot.

We look at the region $E_T^{\gamma_1} + E_T^{\gamma_2} < 90$ GeV as another check of our background estimation. In order to minimize the signal contribution, we impose an additional cut

$$E_T^{\gamma_3} < 24 \text{ GeV}$$

on top of the $E_T^{\gamma_1} + E_T^{\gamma_2} < 90$ GeV cut. The counting result is shown in Table 21. Figures 44–49 show various distributions for $3\gamma + X$ events in this pilot region. We see reasonable agreements between our expectation and the data.

6.2 Stability of fake-background estimation

We vary the tightness of the selection for denominator objects to see how stable the fake-background estimation is. By doing so, the fake rates and photon efficiency also

change, but the estimated fake-background should be consistent within the quoted uncertainties since the final selection is kept the same.

We change the Cut level for defining the denominator objects from 1 to 4 which is denoted in Tables 2 and 11. Also, we compare the cases where we introduce the loose cut or not. The result is shown in Fig. 50 for all the $3\gamma + X$ events and for those with $E_T^{\gamma 1} + E_T^{\gamma 2} > 90$ GeV. The fake-background estimations are stable within the quoted uncertainties.

6.3 `MadGraph/MadEvent` vs. `MCFM`

Our nominal MC data are created by the `MadGraph/MadEvent` which does not include the loop diagrams. We check whether this fact significantly affects the predicted distributions by comparing $E_T^{\gamma 1} + E_T^{\gamma 2}$ between the two as shown in Fig. 51. Both distributions are similar to each other.

As discussed in §4.2.2, the `MadGraph/MadEvent` predicts rather large contributions from $3\gamma + 2j$ events. It would be thus interesting to see if there are any hints for it in the data. Figure 52 shows comparison of the multiplicity of jets in the central region satisfying $E_T > 10$ GeV among the data, `MadGraph/MadEvent`, and `MCFM`. Although the generator-level distributions and others are not directly compared, it is inconclusive mainly due to low statistics of the real data.

7 Final Results

Tables 22–27 show the signal efficiencies for the final selection requirement. Tables 28–36 show the theoretical cross sections, expected and observed cross-section limits for each combination of the m_{h_f} and $m_{H^\pm}$. Figures 53–59 are corresponding plots. Figure 60 is an example plot of the limit as a function of $H^\pm$ mass for $m_{h_f} = 45$ GeV. The excluded mass regions are tabulated in Table 37 and displayed on the m_{h_f}-$m_{H^\pm}$ plane in Fig. 61.

The excluded m_{h_f} values by the DØ analysis for $\tan\beta = 30$ is indicated in the version of Fig. 62 as two vertical lines corresponding to the two $H^\pm$-mass points they study. We added a shaded region between the two lines as it is naturally expected to be excluded. The left vertical line indicates that they reach a maximum sensitivity because the upper end is close to the kinematical limit. Therefore, the left side of this line would be also excluded by their analysis as our analysis does.

The effects of different $\tan\beta$ values are noticable when, especially, the m_{h_f} is close to the $m_{H^\pm}$, i.e. the kinematical limit. For example, the production cross-section would change by a factor of as much as $\simeq 100$ when $\tan\beta$ is changed from $\tan\beta = 3$ to $\tan\beta = 30$ for $(m_{h_f}, m_{H^\pm}) = (80, 100)$ GeV [9]. The factor of 10 increase of the production cross-section would result in the m_{h_f} limit change of about 10 GeV as we see, for example, from the $m_{H^\pm} = 90$ GeV result in Fig. 54. In this region, the $\mathcal{B}(H^\pm \to h_f W^\pm)$ becomes smaller due to smaller available phase-space and becomes

comparable to the suppressed $H^{\pm}$ decays to fermions. The way to bring the sensitivity back is to make $\mathcal{B}(H^{\pm}\to h_f W^{\pm})$ larger by further suppressing the $H^{\pm}$ decays to fermions with larger $\tan\beta$ values. In other kinematical regions, $\tan\beta$ does not affect the search sensitivity so much if $\tan\beta > 10$ because the coupling $\propto \sin\beta$ is already saturated and the $\mathcal{B}(H^{\pm}\to h_f W^{\pm})$ is always dominant. We explicitly check the effects of the $\tan\beta$ on the production cross-section in Fig. 63, where the top plot compares $\tan\beta = 10$ and $\tan\beta = 30$, while the bottom plot compares $\tan\beta = 10$ and $\tan\beta = 3$. The cross section limits are given in Figs. 64–70 for $\tan\beta = 30$ and in Figs. 71–77 for $\tan\beta = 3$. The corresponding excluded mass-regions are shown in Fig. 78, respectively. Figure 79 include the results from the DØ analysis as a reference.

8 Conclusions

We searched for the fermiophobic Higgs boson (h_f) in the two Higgs double model (type I) using the $3\gamma + X$ final state coming from the process

$$p\overline{p}\to h_f H^{\pm}\to h_f(h_f W^*)\to 4\gamma + X\ .$$

The number of background events was estimated to be 2.96 ± 0.94 for the integrated luminosity of 9.2 fb^{-1}, which was dominated by the contribution from direct triphoton events. The observed number of events was 5, which was consistent with the expected number of background events. The numbers of signal events were estimated for the m_{h_f} ranging from 10 to 105 GeV and for $m_{H^{\pm}}$ from 30 to 300 GeV, which were then translated to the excluded mass region on the m_{h_f} vs. $m_{H^{\pm}}$ plane at the 95% confidence level.

Table 1: Trigger selection.

DIPHOTON_12	
Level 1	• Single tower $E_T > 8$ GeV • Single tower Had/EM < 0.125 $\|\|$ $E_T > 14$ GeV
Level 2	• Two high E_T pass clusters, $E_T > 10$ GeV, $\|\eta\| < 3.6$ • Clusters Had/EM < 0.125 • Clusters Iso $< 0.15 \times E_T$ $\|\|$ < 3 GeV
Level 3	• Two L3 clusters, $E_T > 12$ GeV • Clusters Had/EM $< 0.055 + 0.00045 \times E$ $\|\|$ $E_T > 200$ GeV • Clusters Iso (cone 0.4) $< 0.1 \times E_T$ $\|\|$ < 2 GeV • For the central, average and scaled CES-$\chi^2 < 20$
DIPHOTON_18	
Level 1	Same as the DIPHOTON_12
Level 2	• Two high E_T pass clusters, $E_T > 16$ GeV, $\|\eta\| < 3.6$ • Clusters Had/EM < 0.125
Level 3	• Two L3 clusters, $E_T > 18$ GeV • Clusters Had/EM $< 0.055 + 0.00045 \times E$ $\|\|$ $E_T > 200$ GeV • For the central, average and scaled CES-$\chi^2 < 20$
TRIPHOTON	
Level 1	Same as the DIPHOTON_12
Level 2	• Three high E_T pass clusters, $E_T > 10$ GeV, $\|\eta\| < 3.6$ • Clusters Had/EM < 0.125
Level 3	• Three L3 clusters, $E_T > 10$ GeV

Table 2: Standard photon selection cuts.

		Cut level	Base cuts
Geometrical and kinematical cuts			
Detector	CEM/CHA/WHA	0	$\surd$
	CEM	1	$\surd$
Pseudo-rapidity	$\|\eta\| < 1.1$	0	$\surd$
CES fiduciality	$\|X_{\rm CES}\| \leq 21$ cm, 9 cm $\leq \|Z_{\rm CES}\| \leq 230$ cm	1	$\surd$
Kinematical cut	$E_T > 15$ GeV	0	$\surd$
Track cuts			
Associated tracks	$\begin{cases} \text{N3D tracks} \leq 1 \\ p_T \leq 1.0 + 0.005 \times E_T \text{ GeV}/c \text{ (N3D=1)} \end{cases}$	1	$\surd$
Isolation cuts			
Corrected Iso (cone 0.4)	Iso $\leq 0.1 \times E_T \mid\mid < 2$ GeV	3	
	$\begin{cases} E_T \leq 20 \text{ GeV} : \text{Iso} \leq 0.1 \times E_T \text{ GeV} \\ E_T > 20 \text{ GeV} : \text{Iso} \leq 2.0 + 0.02 \times (E_T - 20) \text{ GeV} \end{cases}$	5	
Track Iso (cone 0.4)	Iso $\leq 2.0 + 0.005 \times E_T$ GeV	5	
Identification cuts			
Shower profile	Had/EM $< 0.055 + 0.00045 \times E \mid\mid E_T > 200$ GeV	2	
	$\overline{\chi}^2_{\rm CES} \equiv \dfrac{\chi^2_{\rm strip} + \chi^2_{\rm wire}}{2} < 20$	4	
	Had/EM $< 0.055 + 0.00045 \times E \mid\mid \leq 0.125$	5	
2nd CES cluster	$\begin{cases} E_T \leq 18 \text{ GeV} : E_T^{\rm 2nd} \leq 0.14 \times E_T \text{ GeV} \\ E_T > 18 \text{ GeV} : E_T^{\rm 2nd} \leq 2.4 + 0.01 \times E_T \text{ GeV} \end{cases}$	5	

Table 3: List of the generated mass points. The dataset IDs are not relevant for general readers.

plot100.p050.tex

		$H^{\pm}$ mass (GeV)								
		30	45	50	60	75	90	120	150	175
	key	m	b	a	z	0	1	2	3	4
h_f mass (GeV)										
10	w	—	h4gpbw	h4gpaw	h4gpzw	h4gp0w	h4gp1w	h4gp2w	h4gp3w	h4gp4w
11	p	—	h4gpbp	—	—	—	—	—	—	—
12	q	h4gpmq	—	—	—	—	—	—	—	—
13	r	h4gpmr	h4gpbr	—	—	—	—	—	—	—
15	x	h4gpmx	h4gpbx	h4gpax	h4gpzx	h4gp0x	h4gp1x	h4gp2x	h4gp3x	h4gp4x
20	y	h4gpmy	h4gpby	h4gpay	h4gpzy	h4gp0y	h4gp1y	h4gp2y	h4gp3y	h4gp4y
25	t	h4gpmt	—	—	—	—	—	—	—	—
28	c	h4gpmc	—	—	—	—	—	—	—	—
30	0	—	h4gpb0	h4gpa0	h4gpz0	h4gp00	h4gp10	h4gp20	h4gp30	h4gp40
40	1	—	h4gpb1	h4gpa1	h4gpz1	h4gp01	h4gp11	h4gp21	h4gp31	h4gp41
43	d	—	h4gpbd	—	—	—	—	—	—	—
45	2	—	—	h4gpa2	h4gpz2	h4gp02	h4gp12	h4gp22	h4gp32	h4gp42
48	e	—	—	h4gpae	—	—	—	—	—	—
50	3	—	—	—	h4gpz3	h4gp03	h4gp13	h4gp23	h4gp33	h4gp43
55	o	—	—	—	h4gpzo	—	—	—	—	—
58	f	—	—	—	h4gpzf	—	—	—	—	—
60	4	—	—	—	—	h4gp04	h4gp14	h4gp24	h4gp34	h4gp44
70	5	—	—	—	—	h4gp05	h4gp15	h4gp25	h4gp35	h4gp45
75	6	—	—	—	—	—	h4gp16	h4gp26	h4gp36	h4gp46
77	7	—	—	—	—	—	h4gp17	h4gp27	h4gp37	h4gp47
85	8	—	—	—	—	—	h4gp18	h4gp28	h4gp38	h4gp48
90	9	—	—	—	—	—	—	h4gp29	h4gp39	h4gp49
100	a	—	—	—	—	—	—	h4gp2a	h4gp3a	h4gp4a
105	b	—	—	—	—	—	—	h4gp2b	h4gp3b	h4gp4b

Table 4: List of the generated mass points. The dataset IDs are not relevant for general readers.

plot100.p051.tex

		$H^{\pm}$ mass (GeV)								
		200	210	215	220	224	230	235	240	245
	key	5	d	e	f	v	g	h	i	j
h_f mass (GeV)										
10	w	h4gp5w	h4gpdw	h4gpew	—	—	—	h4gphw	—	—
11	p	—	—	—	—	—	—	—	—	—
12	q	—	—	—	—	—	—	—	—	—
13	r	—	—	—	—	—	—	—	—	—
15	x	h4gp5x	h4gpdx	h4gpex	h4gpfx	h4gpvx	h4gpgx	h4gphx	—	—
20	y	h4gp5y	h4gpdy	h4gpey	h4gpfy	h4gpvy	h4gpgy	h4gphy	h4gpiy	h4gpjy
25	t	—	—	—	—	—	—	—	—	—
28	c	—	—	—	—	—	—	—	—	—
30	0	h4gp50	h4gpd0	h4gpe0	h4gpf0	h4gpv0	h4gpg0	h4gph0	h4gpi0	h4gpj0
40	1	h4gp51	h4gpd1	h4gpe1	h4gpf1	h4gpv1	h4gpg1	h4gph1	h4gpi1	h4gpj1
43	d	—	—	—	—	—	—	—	—	—
45	2	h4gp52	h4gpd2	h4gpe2	h4gpf2	h4gpv2	h4gpg2	h4gph2	h4gpi2	h4gpj2
48	e	—	—	—	—	—	—	—	—	—
50	3	h4gp53	h4gpd3	h4gpe3	h4gpf3	h4gpv3	h4gpg3	h4gph3	h4gpi3	h4gpj3
55	o	—	—	—	—	—	—	—	—	—
58	f	—	—	—	—	—	—	—	—	—
60	4	h4gp54	h4gpd4	h4gpe4	h4gpf4	h4gpv4	h4gpg4	h4gph4	h4gpi4	h4gpj4
70	5	h4gp55	h4gpd5	h4gpe5	h4gpf5	h4gpv5	h4gpg5	h4gph5	h4gpi5	h4gpj5
75	6	h4gp56	h4gpd6	h4gpe6	h4gpf6	h4gpv6	h4gpg6	h4gph6	h4gpi6	h4gpj6
77	7	h4gp57	h4gpd7	h4gpe7	h4gpf7	h4gpv7	h4gpg7	h4gph7	h4gpi7	h4gpj7
85	8	h4gp58	h4gpd8	h4gpe8	h4gpf8	h4gpv8	h4gpg8	h4gph8	h4gpi8	h4gpj8
90	9	h4gp59	h4gpd9	h4gpe9	h4gpf9	h4gpv9	h4gpg9	h4gph9	h4gpi9	h4gpj9
100	a	h4gp5a	h4gpda	h4gpea	h4gpfa	h4gpva	h4gpga	h4gpha	h4gpia	h4gpja
105	b	h4gp5b	h4gpdb	h4gpeb	h4gpfb	h4gpvb	h4gpgb	h4gphb	h4gpib	h4gpjb

Table 5: List of the generated mass points. The dataset IDs are not relevant for general readers.

plot100.p052.tex

		$H^{\pm}$ mass (GeV)							
		248	250	260	270	275	285	290	300
	key	y	7	p	r	8	t	u	9
h_f mass (GeV)									
10	w	—	h4gp7w	—	—	h4gp8w	—	—	h4gp9w
11	p	—	—	—	—	—	—	—	—
12	q	—	—	—	—	—	—	—	—
13	r	—	—	—	—	—	—	—	—
15	x	—	h4gp7x	—	—	h4gp8x	—	—	h4gp9x
20	y	h4gpyy	h4gp7y	h4gppy	h4gpry	h4gp8y	h4gpty	h4gpuy	h4gp9y
25	t	—	—	—	—	—	—	—	—
28	c	—	—	—	—	—	—	—	—
30	0	h4gpy0	h4gp70	h4gpp0	h4gpr0	h4gp80	h4gpt0	h4gpu0	h4gp90
40	1	h4gpy1	h4gp71	h4gpp1	h4gpr1	h4gp81	h4gpt1	h4gpu1	h4gp91
43	d	—	—	—	—	—	—	—	—
45	2	h4gpy2	h4gp72	h4gpp2	h4gpr2	h4gp82	h4gpt2	h4gpu2	h4gp92
48	e	—	—	—	—	—	—	—	—
50	3	h4gpy3	h4gp73	h4gpp3	h4gpr3	h4gp83	h4gpt3	h4gpu3	h4gp93
55	o	—	—	—	—	—	—	—	—
58	f	—	—	—	—	—	—	—	—
60	4	h4gpy4	h4gp74	h4gpp4	h4gpr4	h4gp84	h4gpt4	h4gpu4	h4gp94
70	5	h4gpy5	h4gp75	h4gpp5	h4gpr5	h4gp85	h4gpt5	h4gpu5	h4gp95
75	6	h4gpy6	h4gp76	h4gpp6	h4gpr6	h4gp86	h4gpt6	h4gpu6	h4gp96
77	7	h4gpy7	h4gp77	h4gpp7	h4gpr7	h4gp87	h4gpt7	h4gpu7	h4gp97
85	8	h4gpy8	h4gp78	h4gpp8	h4gpr8	h4gp88	h4gpt8	h4gpu8	h4gp98
90	9	h4gpy9	h4gp79	h4gpp9	h4gpr9	h4gp89	h4gpt9	h4gpu9	h4gp99
100	a	h4gpya	h4gp7a	h4gppa	h4gpra	h4gp8a	h4gpta	h4gpua	h4gp9a
105	b	h4gpyb	h4gp7b	h4gppb	h4gprb	h4gp8b	h4gptb	h4gpub	h4gp9b

Table 6: Detection efficiencies estimated by using Monte Carlo data, with showing statistical errors only.

plot100.p201.tex

h_f mass	$H^{\pm}$ mass (GeV)								
(GeV)	30	45	50	60	75	90	120	150	175
10.0	—	0.000728	0.000590	0.000545	0.00385	0.00159	0.00680	0.00633	0.00309
	—	±0.000022	±0.000022	±0.000020	±0.00016	±0.00010	±0.00046	±0.00044	±0.00031
11.0	—	0.000776	—	—	—	—	—	—	—
	—	±0.000023	—	—	—	—	—	—	—
12.0	0.003296	—	—	—	—	—	—	—	—
	±0.000046	—	—	—	—	—	—	—	—
13.0	0.003595	0.000963	—	—	—	—	—	—	—
	±0.000053	±0.000037	—	—	—	—	—	—	—
15.0	0.004147	0.000986	0.001079	0.00201	0.01497	0.01239	0.02140	0.02784	0.02425
	±0.000099	±0.000059	±0.000062	±0.00026	±0.00070	±0.00065	±0.00082	±0.00094	±0.00088
20.0	0.00614	0.00147	0.00144	0.00891	0.02374	0.0296	0.0358	0.0549	0.0548
	±0.00012	±0.00010	±0.00010	±0.00053	±0.00090	±0.0010	±0.0011	±0.0014	±0.0014
25.0	0.01009	—	—	—	—	—	—	—	—
	±0.00016	—	—	—	—	—	—	—	—
28.0	0.01624	—	—	—	—	—	—	—	—
	±0.00077	—	—	—	—	—	—	—	—
30.0	—	0.00785	0.01675	0.0365	0.0480	0.0554	0.0547	0.0849	0.0998
	—	±0.00049	±0.00071	±0.0011	±0.0012	±0.0013	±0.0012	±0.0016	±0.0017
40.0	—	0.0530	0.0560	0.0629	0.0718	0.0790	0.0773	0.1038	0.1217
	—	±0.0013	±0.0013	±0.0015	±0.0015	±0.0016	±0.0015	±0.0018	±0.0020
43.0	—	0.0697	—	—	—	—	—	—	—
	—	±0.0016	—	—	—	—	—	—	—
45.0	—	—	0.0728	0.0779	0.0830	0.0896	0.0957	0.1100	0.1296
	—	—	±0.0016	±0.0017	±0.0016	±0.0017	±0.0017	±0.0018	±0.0020
48.0	—	—	0.0856	—	—	—	—	—	—
	—	—	±0.0018	—	—	—	—	—	—
50.0	—	—	—	0.0855	0.0912	0.1005	0.1082	0.1159	0.1377
	—	—	—	±0.0017	±0.0017	±0.0018	±0.0018	±0.0019	±0.0020
55.0	—	—	—	0.1002	—	—	—	—	—
	—	—	—	±0.0020	—	—	—	—	—
58.0	—	—	—	0.1133	—	—	—	—	—
	—	—	—	±0.0021	—	—	—	—	—
60.0	—	—	—	—	0.1093	0.1168	0.1263	0.1255	0.1450
	—	—	—	—	±0.0018	±0.0019	±0.0020	±0.0020	±0.0021
70.0	—	—	—	—	0.1297	0.1289	0.1378	0.1340	0.1482
	—	—	—	—	±0.0021	±0.0020	±0.0021	±0.0021	±0.0022
75.0	—	—	—	—	—	0.1327	0.1409	0.1451	0.1541
	—	—	—	—	—	±0.0021	±0.0010	±0.0022	±0.0022
77.0	—	—	—	—	—	0.1334	0.1464	0.1469	0.1510
	—	—	—	—	—	±0.0021	±0.0022	±0.0021	±0.0022
85.0	—	—	—	—	—	0.1551	0.1502	0.1559	0.1509
	—	—	—	—	—	±0.0023	±0.0022	±0.0022	±0.0022
90.0	—	—	—	—	—	—	0.1529	0.1566	0.1511
	—	—	—	—	—	—	±0.0022	±0.0022	±0.0022
100.0	—	—	—	—	—	—	0.1589	0.1643	0.1617
	—	—	—	—	—	—	±0.0023	±0.0023	±0.0023
105.0	—	—	—	—	—	—	0.1602	0.1599	0.1647
	—	—	—	—	—	—	±0.0022	±0.0022	±0.0023

Table 7: Detection efficiencies estimated by using Monte Carlo data, with showing statistical errors only.

plot100.p202.tex

h_f mass	$H^{\pm}$ mass (GeV)								
(GeV)	200	210	215	220	224	230	235	240	245
10.0	0.00207	0.00173	0.00119	—	—	—	0.00154	—	—
	±0.00026	±0.00023	±0.00020	—	—	—	±0.00022	—	—
11.0	—	—	—	—	—	—	—	—	—
	—	—	—	—	—	—	—	—	—
12.0	—	—	—	—	—	—	—	—	—
	—	—	—	—	—	—	—	—	—
13.0	—	—	—	—	—	—	—	—	—
	—	—	—	—	—	—	—	—	—
15.0	0.01859	0.01443	0.01284	0.01157	0.01117	0.01014	0.00851	—	—
	±0.00078	±0.00069	±0.00063	±0.00061	±0.00059	±0.00057	±0.00052	—	—
20.0	0.0469	0.0438	0.0411	0.0391	0.0376	0.0359	0.03041	0.02941	0.02690
	±0.0013	±0.0012	±0.0012	±0.0011	±0.0011	±0.0011	±0.00099	±0.00100	±0.00091
25.0	—	—	—	—	—	—	—	—	—
	—	—	—	—	—	—	—	—	—
28.0	—	—	—	—	—	—	—	—	—
	—	—	—	—	—	—	—	—	—
30.0	0.1035	0.1020	0.1028	0.0989	0.0982	0.0964	0.0972	0.0964	0.0984
	±0.0018	±0.0019	±0.0019	±0.0019	±0.0019	±0.0018	±0.0019	±0.0018	±0.0019
40.0	0.1330	0.1408	0.1343	0.1405	0.1384	0.1391	0.1375	0.1409	0.1425
	±0.0021	±0.0023	±0.0021	±0.0022	±0.0023	±0.0022	±0.0022	±0.0023	±0.0023
43.0	—	—	—	—	—	—	—	—	—
	—	—	—	—	—	—	—	—	—
45.0	0.1455	0.1475	0.1488	0.1502	0.1514	0.1554	0.1555	0.1557	0.1520
	±0.0021	±0.0023	±0.0023	±0.0024	±0.0024	±0.0024	±0.0023	±0.0023	±0.0023
48.0	—	—	—	—	—	—	—	—	—
	—	—	—	—	—	—	—	—	—
50.0	0.1496	0.1564	0.1547	0.1536	0.1605	0.1592	0.1595	0.1597	0.1705
	±0.0022	±0.0025	±0.0023	±0.0024	±0.0025	±0.0024	±0.0024	±0.0024	±0.0026
55.0	—	—	—	—	—	—	—	—	—
	—	—	—	—	—	—	—	—	—
58.0	—	—	—	—	—	—	—	—	—
	—	—	—	—	—	—	—	—	—
60.0	0.1601	0.1610	0.1647	0.1669	0.1682	0.1698	0.1713	0.1702	0.1737
	±0.0023	±0.0024	±0.0025	±0.0025	±0.0025	±0.0025	±0.0025	±0.0025	±0.0026
70.0	0.1664	0.1680	0.1694	0.1726	0.1804	0.1827	0.1803	0.1826	0.1824
	±0.0023	±0.0025	±0.0024	±0.0025	±0.0026	±0.0027	±0.0026	±0.0027	±0.0026
75.0	0.1694	0.1711	0.1741	0.1761	0.1757	0.1797	0.1797	0.1877	0.1847
	±0.0023	±0.0025	±0.0026	±0.0026	±0.0026	±0.0026	±0.0027	±0.0026	±0.0026
77.0	0.1690	0.1731	0.1734	0.1782	0.1790	0.1856	0.1862	0.1849	0.1864
	±0.0023	±0.0025	±0.0025	±0.0025	±0.0025	±0.0026	±0.0026	±0.0025	±0.0026
85.0	0.1681	0.1742	0.1772	0.1788	0.1794	0.1843	0.1827	0.1850	0.1896
	±0.0023	±0.0025	±0.0026	±0.0025	±0.0026	±0.0026	±0.0026	±0.0026	±0.0026
90.0	0.1660	0.1753	0.1729	0.1814	0.1828	0.1856	0.1900	0.1933	0.1862
	±0.0023	±0.0025	±0.0025	±0.0026	±0.0026	±0.0026	±0.0026	±0.0028	±0.0025
100.0	0.1645	0.1725	0.1751	0.1785	0.1801	0.1820	0.1865	0.1919	0.1885
	±0.0023	±0.0025	±0.0025	±0.0025	±0.0026	±0.0026	±0.0027	±0.0026	±0.0027
105.0	0.1644	0.1739	0.1742	0.1781	0.1811	0.1814	0.1856	0.1866	0.1885
	±0.0023	±0.0025	±0.0026	±0.0025	±0.0026	±0.0025	±0.0026	±0.0027	±0.0027

Table 8: Detection efficiencies estimated by using Monte Carlo data, with showing statistical errors only.

plot100.p203.tex

h_f mass	$H^{\pm}$ mass (GeV)							
(GeV)	248	250	260	270	275	285	290	300
10.0	—	0.00139	—	—	0.00172	—	—	0.00170
	—	±0.00022	—	—	±0.00024	—	—	±0.00023
11.0	—	—	—	—	—	—	—	—
	—	—	—	—	—	—	—	—
12.0	—	—	—	—	—	—	—	—
	—	—	—	—	—	—	—	—
13.0	—	—	—	—	—	—	—	—
	—	—	—	—	—	—	—	—
15.0	—	0.00736	—	—	0.00603	—	—	0.00447
	—	±0.00049	—	—	±0.00045	—	—	±0.00039
20.0	0.02593	0.02479	0.02174	0.02055	0.01843	0.01710	0.01598	0.01482
	±0.00091	±0.00090	±0.00084	±0.00081	±0.00079	±0.00078	±0.00073	±0.00072
25.0	—	—	—	—	—	—	—	—
	—	—	—	—	—	—	—	—
28.0	—	—	—	—	—	—	—	—
	—	—	—	—	—	—	—	—
30.0	0.0918	0.0909	0.0880	0.0802	0.0800	0.0773	0.0769	0.0695
	±0.0018	±0.0017	±0.0017	±0.0017	±0.0017	±0.0016	±0.0016	±0.0015
40.0	0.1446	0.1393	0.1478	0.1421	0.1417	0.1376	0.1398	0.1365
	±0.0023	±0.0021	±0.0023	±0.0023	±0.0022	±0.0022	±0.0022	±0.0022
43.0	—	—	—	—	—	—	—	—
	—	—	—	—	—	—	—	—
45.0	0.1551	0.1546	0.1548	0.1552	0.1622	0.1584	0.1558	0.1551
	±0.0024	±0.0022	±0.0023	±0.0023	±0.0029	±0.0024	±0.0024	±0.0023
48.0	—	—	—	—	—	—	—	—
	—	—	—	—	—	—	—	—
50.0	0.1644	0.1597	0.1642	0.1678	0.1678	0.1651	0.1660	0.1666
	±0.0024	±0.0022	±0.0024	±0.0024	±0.0025	±0.0024	±0.0024	±0.0024
55.0	—	—	—	—	—	—	—	—
	—	—	—	—	—	—	—	—
58.0	—	—	—	—	—	—	—	—
	—	—	—	—	—	—	—	—
60.0	0.1750	0.1733	0.1782	0.1819	0.1817	0.1837	0.1796	0.1858
	±0.0026	±0.0024	±0.0026	±0.0026	±0.0026	±0.0026	±0.0026	±0.0026
70.0	0.1835	0.1844	0.1901	0.1896	0.1887	0.1954	0.1900	0.1958
	±0.0026	±0.0025	±0.0027	±0.0027	±0.0026	±0.0027	±0.0026	±0.0028
75.0	0.1865	0.1908	0.1884	0.1927	0.1888	0.1962	0.1996	0.1936
	±0.0026	±0.0025	±0.0027	±0.0027	±0.0027	±0.0027	±0.0027	±0.0027
77.0	0.1937	0.1848	0.1927	0.1932	0.1966	0.1957	0.1993	0.1975
	±0.0027	±0.0025	±0.0026	±0.0027	±0.0026	±0.0027	±0.0027	±0.0027
85.0	0.1916	0.1895	0.1919	0.1964	0.1988	0.1992	0.1997	0.1998
	±0.0027	±0.0025	±0.0027	±0.0027	±0.0027	±0.0026	±0.0027	±0.0028
90.0	0.1883	0.1930	0.1941	0.1953	0.1934	0.1997	0.1994	0.2032
	±0.0026	±0.0025	±0.0027	±0.0027	±0.0027	±0.0027	±0.0027	±0.0027
100.0	0.1943	0.1904	0.1947	0.1986	0.1993	0.2079	0.2019	0.2058
	±0.0027	±0.0025	±0.0027	±0.0027	±0.0027	±0.0027	±0.0027	±0.0027
105.0	0.1916	0.1899	0.1951	0.2011	0.1991	0.1981	0.2027	0.2061
	±0.0026	±0.0025	±0.0028	±0.0027	±0.0028	±0.0027	±0.0027	±0.0027

Table 9: Summary of the systematic uncertainties of the signal detection efficiency for the $h_f = 50$ GeV and $H^{\pm} = 90$ GeV.

Sources	Systematic Uncertainty (%)
Photon selection	8.1
PDF	1.0
ISR/FSR	2.0
Q^2	3.0
Total	8.9

Table 10: Cut values determining regions used for the isolation vs. CES-χ^2 method.

Region	$E_T < 20$ GeV		$E_T > 20$ GeV	
A	$\overline{\chi}^2_{\rm CES} > 20$	$\mathrm{ISO}^{\rm cal}_{0.4}/E_T < 0.1$	$\overline{\chi}^2_{\rm CES} > 20$	$\dfrac{(\mathrm{ISO}^{\rm cal}_{0.4} - 2)}{(E_T - 20)} < 0.02$
B	$\overline{\chi}^2_{\rm CES} < 20$	$\mathrm{ISO}^{\rm cal}_{0.4}/E_T > 0.2$	$\overline{\chi}^2_{\rm CES} < 20$	$\dfrac{(\mathrm{ISO}^{\rm cal}_{0.4} - 2)}{(E^{\gamma}_T - 20)} > 0.06$
C	$\overline{\chi}^2_{\rm CES} < 20$	$\mathrm{ISO}^{\rm cal}_{0.4}/E_T < 0.1$	$\overline{\chi}^2_{\rm CES} < 20$	$\dfrac{(\mathrm{ISO}^{\rm cal}_{0.4} - 2)}{(E^{\gamma}_T - 20)} < 0.02$
D	$\overline{\chi}^2_{\rm CES} > 20$	$\mathrm{ISO}^{\rm cal}_{0.4}/E_T > 0.2$	$\overline{\chi}^2_{\rm CES} > 20$	$\dfrac{(\mathrm{ISO}^{\rm cal}_{0.4} - 2)}{(E^{\gamma}_T - 20)} > 0.06$

Table 11: Central electron event selection cuts.

		Cut level	Base cuts
Geometrical and kinematical cuts			
Detector	CEM/CHA/WHA	0	$\surd$
	CEM	1	$\surd$
Pseudo-rapidity	$\|\eta\| < 1.1$	0	$\surd$
CES fiduciality	$\|X_{\rm CES}\| \leq 21$ cm, 9 cm $\leq \|Z_{\rm CES}\| \leq 230$ cm	1	$\surd$
Kinematical cut	$E_T > 15$ GeV	0	$\surd$
Track cuts			
Associated tracks	$\begin{cases} \text{N3D tracks} \leq 2 \\ p_T \leq 1.0 + 0.005 \times E_T \text{ GeV}/c \text{ (N3D=2)} \end{cases}$	1	$\surd$
Isolation cuts			
Corrected Iso (cone 0.4)	Iso $\leq 0.1 \times E_T$ $\|\|$ < 2 GeV	3	
	$\begin{cases} E_T \leq 20 \text{ GeV} : \text{Iso} \leq 0.1 \times E_T \text{ GeV} \\ E_T > 20 \text{ GeV} : \text{Iso} \leq 2.0 + 0.02 \times (E_T - 20) \text{ GeV} \end{cases}$	5	
Track Iso (cone 0.4)	Iso $\leq 2.0 + 0.005 \times E_T$ GeV	5	
Identification cuts			
CAL-track matching	$0.9 < E/p < 1.1$	1	$\surd$
Shower profile	Had/EM $< 0.055 + 0.00045 \times E$ $\|\|$ $E_T > 200$ GeV	2	
	$\overline{\chi}^2_{\rm CES} \equiv \dfrac{\chi^2_{\rm strip} + \chi^2_{\rm wire}}{2} < 20$	4	
	Had/EM $< 0.055 + 0.00045 \times E$ $\|\|$ ≤ 0.125	5	
2nd CES cluster	$\begin{cases} E_T \leq 18 \text{ GeV} : E_T^{\rm 2nd} \leq 0.14 \times E_T \text{ GeV} \\ E_T > 18 \text{ GeV} : E_T^{\rm 2nd} \leq 2.4 + 0.01 \times E_T \text{ GeV} \end{cases}$	5	

Table 12: The probability of a photon to pass the photon selection (ϵ_s). We use the probability as the ϵ_s in the efficiency matrix ($\boldsymbol{E}$) when estimating the number of fake-photon events.

plot301.p010.tex

Periods	ϵ_s
0–9	0.951 ± 0.015
10–17	0.935 ± 0.014
18–28	0.960 ± 0.011
29–38	0.935 ± 0.010

Table 13: The probability of a photon passing the loose denominator cuts to pass also the final photon selection (ϵ'_s).

plot321.p010.tex

Periods	ϵ_s
0–9	0.491 ± 0.007
10–17	0.445 ± 0.006
18–28	0.420 ± 0.005
29–38	0.461 ± 0.005

Table 14: Comparison between the MadGraph/MadEvent and MCFM cross-section calculations.

			MadGraph/MadEvent (fb)	MCFM (v6.8) (fb)
LO		$q\bar{q}\to 3\gamma$	2.617	2.787
NLO (loop)		$q\bar{q}\to 3\gamma$	—	
NLO (tree)		$q\bar{q}\to(3\gamma)g$	0.796	
		$qg\to(3\gamma)q$ and $\bar{q}g\to(3\gamma)\bar{q}$	1.498	
	Total		4.911	4.667
NNLO (tree)		$q\bar{q}\to(3\gamma)gg$		—
		$q\bar{q}\to(3\gamma)q\bar{q}$		—
		Total	1.529	—
		$qg\to(3\gamma)qg$ and $\bar{q}g\to(3\gamma)\bar{q}g$	0.268	—
		$gg\to(3\gamma)q\bar{q}$	0.132	—
Total			6.840	—

Table 15: Summary of the Monte Carlo studies for the contributions from the electroweak processes.

Process	DSID	Generated	L (fb^{-1})	Events
$Z(\to ee)\gamma$	rewk33	4.0M	281	0.1676 ± 0.0015(stat)
$W(\to e\nu)\gamma$	rewk28	6.6M	15	$(2.500 \pm 0.036$(stat)$) \times 10^{-2}$
$Z(\to\tau\tau)\gamma$	rewk37	9.3M	644	0.256 ± 0.060(stat)
$W(\to\tau\nu)\gamma$	rewk6a	9.0M	470	< 0.059 (95% C.L.)
Total*				0.449 ± 0.060(stat)

* $W(\to\tau\nu)\gamma$ is omitted.

Table 16: Summary of systematic errors for the counting experiments.

plot921.p002.sys.cdfnote.tex

$h_f H^{\pm} \to 3\gamma + X$	CDF Run II Preliminary: 9179.8 pb^{-1}			
Sources	Uncertainty (%)			
	Signal	Fakes	DTP	EWK
Photon selection	8	1	8	8
PDF	1	—	1	—
ISR/FSR	2	—	6	—
Fake rates	—	23	—	—
q/g composition	—	37	—	—
Parton-shower matching	—	—	1	—
Cross section	20	—	33	—
EWK normalization	—	—	—	71
Luminosity	6	—	6	6
Total	23	43	35	72

Table 17: Total background to the $3\gamma + X$ final state.

plot921.p001.3g.cdfnote.tex

$h_f H^{\pm} \to 3\gamma + X$	CDF Run II Preliminary: 9179.8 pb^{-1}				
	Events ($E_T^{\gamma 1} + E_T^{\gamma 2} > 30$ GeV: control+signal regions)				
			(stat)		(syst)
Fake	3.0	±	0.2	±	1.2
Direct triphoton	6.9	±	0.1	±	2.4
Electroweak	0.4	±	0.1	±	0.3
Total	10.3	±	0.2	±	2.7
Data			10		

Table 18: Systematic errors considered in producing various distributions. The "variable" means that the errors are different between different bins of histograms.

Sources	Fakes	DTP	EWK
Photon selection	Variable	8%	8%
PDF	—	Variable	—
ISR/FSR	—	Variable	—
Fake rates	Variable	—	—
q/g composition	37%	—	—
Parton-shower matching	—	Variable	—
Cross section	—	33%	—
EWK Normalization	—	—	71%
Luminosity	—	6%	6%

Table 19: Background to the $3\gamma + X$ final state for the final selection requirement.

plot921.p200.3g.cdfnote.tex

$h_f H^{\pm} \to 3\gamma + X$ CDF Run II Preliminary: 9179.8 pb^{-1}

	Events ($E_T^{\gamma 1} + E_T^{\gamma 2} > 90$ GeV: signal region)				
			(stat)		(syst)
Fake	0.32	±	0.07	±	0.15
Direct triphoton	2.60	±	0.04	±	0.93
Electroweak	0.04	±	0.01	±	0.03
Total	2.96	±	0.08	±	0.94
Data	5				

Table 20: Events in the pilot regions and data.

plot921.p200.sb.cdfnote.tex

	Fake					Direct triphoton					Total					Data
			(stat)		(syst)			(stat)		(syst)			(stat)		(syst)	
ppf	360.4	±	0.0	±	44.1	0.83	±	0.02	±	0.29	361.2	±	0.0	±	44.1	360
pfp	7.0	±	0.0	±	2.5	0.35	±	0.01	±	0.12	7.4	±	0.0	±	2.5	7
fpp	3.0	±	0.0	±	1.0	0.17	±	0.01	±	0.06	3.2	±	0.0	±	1.0	3
Total	370.4	±	0.0	±	68.0	1.35	±	0.03	±	0.48	371.8	±	0.0	±	68.0	370

Table 21: Events in the pilot regions and data.

plot921.p205.3g.cdfnote.tex

$h_f H^{\pm} \to 3\gamma + X$ CDF Run II Preliminary: 9179.8 pb^{-1}

	Events (control region)				
			(stat)		(syst)
Fake	2.56	±	0.16	±	1.05
Direct triphoton	3.74	±	0.04	±	1.31
Electroweak	0.32	±	0.05	±	0.22
Total	6.62	±	0.17	±	1.69
Data			5		

Table 22: The efficiency (%) for various m_{h_f} and $m_{H^\pm}$ for the final selection requirement.

plot921.p300.tex

h_f mass (GeV)		$H^\pm$ mass (GeV)								
		30	45	50	60	75	90	120	150	175
10		—	—	0.000394	0.000353	0.0127	0.00642	0.0717	0.0867	0.0789
	(stat)	—	—	±0.000176	±0.000158	±0.0029	±0.00203	±0.0150	±0.0164	±0.0155
	(syst)	—	—	±0.000035	±0.000031	±0.0011	±0.00057	±0.0064	±0.0077	±0.0070
11		—	0.000428	—	—	—	—	—	—	—
	(stat)	—	±0.000175	—	—	—	—	—	—	—
	(syst)	—	±0.000038	—	—	—	—	—	—	—
12		0.000197	—	—	—	—	—	—	—	—
	(stat)	±0.000114	—	—	—	—	—	—	—	—
	(syst)	±0.000018	—	—	—	—	—	—	—	—
13		0.000630	0.00128	—	—	—	—	—	—	—
	(stat)	±0.000223	±0.00043	—	—	—	—	—	—	—
	(syst)	±0.000056	±0.00011	—	—	—	—	—	—	—
15		0.00358	0.00288	0.00530	0.0260	0.198	0.238	0.423	0.946	1.021
	(stat)	±0.00092	±0.00102	±0.00137	±0.0092	±0.025	±0.028	±0.036	±0.054	±0.057
	(syst)	±0.00032	±0.00026	±0.00047	±0.0023	±0.018	±0.021	±0.038	±0.084	±0.091
20		0.00290	0.0183	0.0193	0.176	0.631	0.947	1.23	2.93	3.27
	(stat)	±0.00084	±0.0036	±0.0037	±0.024	±0.046	±0.057	±0.06	±0.10	±0.10
	(syst)	±0.00026	±0.0016	±0.0017	±0.016	±0.056	±0.084	±0.11	±0.26	±0.29
25		0.01032	—	—	—	—	—	—	—	—
	(stat)	±0.00159	—	—	—	—	—	—	—	—
	(syst)	±0.00092	—	—	—	—	—	—	—	—
28		0.0364	—	—	—	—	—	—	—	—
	(stat)	±0.0115	—	—	—	—	—	—	—	—
	(syst)	±0.0032	—	—	—	—	—	—	—	—
30		—	0.0674	0.343	1.027	1.93	2.56	2.97	5.86	7.89
	(stat)	—	±0.0144	±0.032	±0.059	±0.07	±0.08	±0.09	±0.13	±0.15
	(syst)	—	±0.0060	±0.031	±0.091	±0.17	±0.23	±0.26	±0.52	±0.70
40		—	1.075	1.55	2.35	3.25	4.47	4.63	7.70	10.09
	(stat)	—	±0.058	±0.07	±0.09	±0.10	±0.11	±0.12	±0.15	±0.18
	(syst)	—	±0.096	±0.14	±0.21	±0.29	±0.40	±0.41	±0.69	±0.90
43		—	2.03	—	—	—	—	—	—	—
	(stat)	—	±0.09	—	—	—	—	—	—	—
	(syst)	—	±0.18	—	—	—	—	—	—	—
45		—	—	2.41	3.19	4.05	5.17	6.20	8.29	10.95
	(stat)	—	—	±0.09	±0.10	±0.11	±0.12	±0.13	±0.16	±0.18
	(syst)	—	—	±0.21	±0.28	±0.36	±0.46	±0.55	±0.74	±0.97
48		—	—	3.53	—	—	—	—	—	—
	(stat)	—	—	±0.11	—	—	—	—	—	—
	(syst)	—	—	±0.31	—	—	—	—	—	—

Table 23: The efficiency (%) for various m_{h_f} and $m_{H^\pm}$ for the final selection requirement.

plot921.p301.tex

h_f mass (GeV)		$H^\pm$ mass (GeV)								
		30	45	50	60	75	90	120	150	175
50		—	—	—	4.01	5.02	6.28	7.66	8.87	11.8
	(stat)	—	—	—	±0.12	±0.12	±0.14	±0.15	±0.17	±0.2
	(syst)	—	—	—	±0.36	±0.45	±0.56	±0.68	±0.79	±1.1
55		—	—	—	5.73	—	—	—	—	—
	(stat)	—	—	—	±0.15	—	—	—	—	—
	(syst)	—	—	—	±0.51	—	—	—	—	—
58		—	—	—	7.22	—	—	—	—	—
	(stat)	—	—	—	±0.16	—	—	—	—	—
	(syst)	—	—	—	±0.64	—	—	—	—	—
60		—	—	—	—	7.49	8.44	10.07	10.24	12.8
	(stat)	—	—	—	—	±0.15	±0.16	±0.17	±0.18	±0.2
	(syst)	—	—	—	—	±0.67	±0.75	±0.90	±0.91	±1.1
70		—	—	—	—	10.54	10.71	12.1	11.6	13.5
	(stat)	—	—	—	—	±0.18	±0.18	±0.2	±0.2	±0.2
	(syst)	—	—	—	—	±0.94	±0.95	±1.1	±1.0	±1.2
75		—	—	—	—	—	11.8	12.8	13.3	14.4
	(stat)	—	—	—	—	—	±0.2	±0.1	±0.2	±0.2
	(syst)	—	—	—	—	—	±1.1	±1.1	±1.2	±1.3
77		—	—	—	—	—	12.0	13.5	13.8	14.2
	(stat)	—	—	—	—	—	±0.2	±0.2	±0.2	±0.2
	(syst)	—	—	—	—	—	±1.1	±1.2	±1.2	±1.3
85		—	—	—	—	—	14.9	14.5	15.1	14.6
	(stat)	—	—	—	—	—	±0.2	±0.2	±0.2	±0.2
	(syst)	—	—	—	—	—	±1.3	±1.3	±1.3	±1.3
90		—	—	—	—	—	—	15.0	15.4	14.8
	(stat)	—	—	—	—	—	—	±0.2	±0.2	±0.2
	(syst)	—	—	—	—	—	—	±1.3	±1.4	±1.3
100		—	—	—	—	—	—	15.8	16.3	16.1
	(stat)	—	—	—	—	—	—	±0.2	±0.2	±0.2
	(syst)	—	—	—	—	—	—	±1.4	±1.5	±1.4
105		—	—	—	—	—	—	16.0	16.0	16.4
	(stat)	—	—	—	—	—	—	±0.2	±0.2	±0.2
	(syst)	—	—	—	—	—	—	±1.4	±1.4	±1.5

Table 24: The efficiency (%) for various m_{h_f} and $m_{H^\pm}$ for the final selection requirement.

plot921.p302.tex

h_f mass (GeV)		$H^\pm$ mass (GeV)								
		200	210	215	220	224	230	235	240	245
10		0.0541	0.0630	0.0599	—	—	—	0.0463	—	—
	(stat)	±0.0131	±0.0141	±0.0141	—	—	—	±0.0120	—	—
	(syst)	±0.0048	±0.0056	±0.0053	—	—	—	±0.0041	—	—
11		—	—	—	—	—	—	—	—	—
	(stat)	—	—	—	—	—	—	—	—	—
	(syst)	—	—	—	—	—	—	—	—	—
12		—	—	—	—	—	—	—	—	—
	(stat)	—	—	—	—	—	—	—	—	—
	(syst)	—	—	—	—	—	—	—	—	—
13		—	—	—	—	—	—	—	—	—
	(stat)	—	—	—	—	—	—	—	—	—
	(syst)	—	—	—	—	—	—	—	—	—
15		0.921	0.853	0.717	0.679	0.683	0.630	0.496	—	—
	(stat)	±0.055	±0.053	±0.047	±0.046	±0.046	±0.045	±0.040	—	—
	(syst)	±0.082	±0.076	±0.064	±0.060	±0.061	±0.056	±0.044	—	—
20		3.36	3.15	2.99	2.97	2.86	2.72	2.35	2.27	2.12
	(stat)	±0.11	±0.10	±0.10	±0.10	±0.10	±0.10	±0.09	±0.09	±0.08
	(syst)	±0.30	±0.28	±0.27	±0.26	±0.25	±0.24	±0.21	±0.20	±0.19
25		—	—	—	—	—	—	—	—	—
	(stat)	—	—	—	—	—	—	—	—	—
	(syst)	—	—	—	—	—	—	—	—	—
28		—	—	—	—	—	—	—	—	—
	(stat)	—	—	—	—	—	—	—	—	—
	(syst)	—	—	—	—	—	—	—	—	—
30		8.87	8.87	9.06	8.74	8.75	8.70	8.75	8.80	9.02
	(stat)	±0.16	±0.17	±0.18	±0.18	±0.18	±0.17	±0.18	±0.17	±0.18
	(syst)	±0.79	±0.79	±0.81	±0.78	±0.78	±0.77	±0.78	±0.78	±0.80
40		12.0	12.8	12.2	13.0	12.7	12.9	12.9	13.2	13.5
	(stat)	±0.2	±0.2	±0.2	±0.2	±0.2	±0.2	±0.2	±0.2	±0.2
	(syst)	±1.1	±1.1	±1.1	±1.2	±1.1	±1.2	±1.1	±1.2	±1.2
43		—	—	—	—	—	—	—	—	—
	(stat)	—	—	—	—	—	—	—	—	—
	(syst)	—	—	—	—	—	—	—	—	—
45		13.1	13.5	13.9	14.0	14.1	14.6	14.7	14.7	14.5
	(stat)	±0.2	±0.2	±0.2	±0.2	±0.2	±0.2	±0.2	±0.2	±0.2
	(syst)	±1.2	±1.2	±1.2	±1.2	±1.3	±1.3	±1.3	±1.3	±1.3
48		—	—	—	—	—	—	—	—	—
	(stat)	—	—	—	—	—	—	—	—	—
	(syst)	—	—	—	—	—	—	—	—	—

Table 25: The efficiency (%) for various m_{h_f} and $m_{H^\pm}$ for the final selection requirement.

plot921.p303.tex

h_f mass (GeV)		$H^\pm$ mass (GeV)								
		200	210	215	220	224	230	235	240	245
50		13.6	14.6	14.4	14.4	15.1	15.1	15.2	15.3	16.4
	(stat)	±0.2	±0.2	±0.2	±0.2	±0.2	±0.2	±0.2	±0.2	±0.3
	(syst)	±1.2	±1.3	±1.3	±1.3	±1.3	±1.3	±1.4	±1.4	±1.5
55		—	—	—	—	—	—	—	—	—
	(stat)	—	—	—	—	—	—	—	—	—
	(syst)	—	—	—	—	—	—	—	—	—
58		—	—	—	—	—	—	—	—	—
	(stat)	—	—	—	—	—	—	—	—	—
	(syst)	—	—	—	—	—	—	—	—	—
60		14.9	15.2	15.6	15.9	16.1	16.3	16.5	16.4	16.8
	(stat)	±0.2	±0.2	±0.2	±0.2	±0.2	±0.2	±0.2	±0.2	±0.3
	(syst)	±1.3	±1.4	±1.4	±1.4	±1.4	±1.5	±1.5	±1.5	±1.5
70		15.9	16.1	16.2	16.7	17.5	17.7	17.5	17.8	17.9
	(stat)	±0.2	±0.2	±0.2	±0.2	±0.3	±0.3	±0.3	±0.3	±0.3
	(syst)	±1.4	±1.4	±1.4	±1.5	±1.6	±1.6	±1.6	±1.6	±1.6
75		16.3	16.6	16.9	17.1	17.2	17.6	17.6	18.4	18.1
	(stat)	±0.2	±0.2	±0.3	±0.3	±0.3	±0.3	±0.3	±0.3	±0.3
	(syst)	±1.5	±1.5	±1.5	±1.5	±1.5	±1.6	±1.6	±1.6	±1.6
77		16.3	16.8	16.9	17.3	17.5	18.2	18.2	18.1	18.4
	(stat)	±0.2	±0.2	±0.2	±0.2	±0.2	±0.3	±0.3	±0.3	±0.3
	(syst)	±1.4	±1.5	±1.5	±1.5	±1.6	±1.6	±1.6	±1.6	±1.6
85		16.4	17.1	17.5	17.6	17.7	18.2	18.1	18.3	18.8
	(stat)	±0.2	±0.2	±0.3	±0.3	±0.3	±0.3	±0.3	±0.3	±0.3
	(syst)	±1.5	±1.5	±1.6	±1.6	±1.6	±1.6	±1.6	±1.6	±1.7
90		16.4	17.3	17.1	18.0	18.1	18.4	18.8	19.2	18.5
	(stat)	±0.2	±0.3	±0.2	±0.3	±0.3	±0.3	±0.3	±0.3	±0.3
	(syst)	±1.5	±1.5	±1.5	±1.6	±1.6	±1.6	±1.7	±1.7	±1.6
100		16.4	17.2	17.4	17.8	17.9	18.1	18.6	19.1	18.8
	(stat)	±0.2	±0.2	±0.3	±0.3	±0.3	±0.3	±0.3	±0.3	±0.3
	(syst)	±1.5	±1.5	±1.6	±1.6	±1.6	±1.6	±1.7	±1.7	±1.7
105		16.4	17.4	17.4	17.8	18.1	18.1	18.5	18.6	18.8
	(stat)	±0.2	±0.3	±0.3	±0.3	±0.3	±0.3	±0.3	±0.3	±0.3
	(syst)	±1.5	±1.5	±1.5	±1.6	±1.6	±1.6	±1.6	±1.7	±1.7

Table 26: The efficiency (%) for various m_{h_f} and $m_{H^\pm}$ for the final selection requirement.

plot921.p304.tex

h_f mass (GeV)		$H^\pm$ mass (GeV)							
		248	250	260	270	275	285	290	300
10		—	0.0136	—	—	0.0232	—	—	0.0185
	(stat)	—	±0.0068	—	—	±0.0088	—	—	±0.0075
	(syst)	—	±0.0012	—	—	±0.0021	—	—	±0.0016
11		—	—	—	—	—	—	—	—
	(stat)	—	—	—	—	—	—	—	—
	(syst)	—	—	—	—	—	—	—	—
12		—	—	—	—	—	—	—	—
	(stat)	—	—	—	—	—	—	—	—
	(syst)	—	—	—	—	—	—	—	—
13		—	—	—	—	—	—	—	—
	(stat)	—	—	—	—	—	—	—	—
	(syst)	—	—	—	—	—	—	—	—
15		—	0.443	—	—	0.262	—	—	0.156
	(stat)	—	±0.038	—	—	±0.030	—	—	±0.023
	(syst)	—	±0.039	—	—	±0.023	—	—	±0.014
20		2.00	1.89	1.72	1.59	1.35	1.22	1.22	1.093
	(stat)	±0.08	±0.08	±0.07	±0.07	±0.07	±0.07	±0.06	±0.062
	(syst)	±0.18	±0.17	±0.15	±0.14	±0.12	±0.11	±0.11	±0.097
25		—	—	—	—	—	—	—	—
	(stat)	—	—	—	—	—	—	—	—
	(syst)	—	—	—	—	—	—	—	—
28		—	—	—	—	—	—	—	—
	(stat)	—	—	—	—	—	—	—	—
	(syst)	—	—	—	—	—	—	—	—
30		8.39	8.29	8.05	7.29	7.40	7.07	7.00	6.22
	(stat)	±0.17	±0.16	±0.16	±0.16	±0.16	±0.15	±0.15	±0.14
	(syst)	±0.75	±0.74	±0.72	±0.65	±0.66	±0.63	±0.62	±0.55
40		13.7	13.2	14.1	13.6	13.5	13.2	13.4	13.1
	(stat)	±0.2	±0.2	±0.2	±0.2	±0.2	±0.2	±0.2	±0.2
	(syst)	±1.2	±1.2	±1.3	±1.2	±1.2	±1.2	±1.2	±1.2
43		—	—	—	—	—	—	—	—
	(stat)	—	—	—	—	—	—	—	—
	(syst)	—	—	—	—	—	—	—	—
45		14.8	14.8	14.8	14.9	15.7	15.3	15.0	15.0
	(stat)	±0.2	±0.2	±0.2	±0.2	±0.3	±0.2	±0.2	±0.2
	(syst)	±1.3	±1.3	±1.3	±1.3	±1.4	±1.4	±1.3	±1.3
48		—	—	—	—	—	—	—	—
	(stat)	—	—	—	—	—	—	—	—
	(syst)	—	—	—	—	—	—	—	—

Table 27: The efficiency (%) for various m_{h_f} and $m_{H^\pm}$ for the final selection requirement.

plot921.p305.tex

h_f mass (GeV)		$H^\pm$ mass (GeV)							
		248	250	260	270	275	285	290	300
50		15.8	15.4	15.8	16.2	16.3	16.0	16.2	16.2
	(stat)	±0.2	±0.2	±0.2	±0.2	±0.2	±0.2	±0.2	±0.2
	(syst)	±1.4	±1.4	±1.4	±1.4	±1.5	±1.4	±1.4	±1.4
55		—	—	—	—	—	—	—	—
	(stat)	—	—	—	—	—	—	—	—
	(syst)	—	—	—	—	—	—	—	—
58		—	—	—	—	—	—	—	—
	(stat)	—	—	—	—	—	—	—	—
	(syst)	—	—	—	—	—	—	—	—
60		16.9	16.8	17.4	17.8	17.8	18.0	17.6	18.2
	(stat)	±0.3	±0.2	±0.3	±0.3	±0.3	±0.3	±0.3	±0.3
	(syst)	±1.5	±1.5	±1.5	±1.6	±1.6	±1.6	±1.6	±1.6
70		17.9	18.0	18.7	18.7	18.6	19.3	18.8	19.3
	(stat)	±0.3	±0.2	±0.3	±0.3	±0.3	±0.3	±0.3	±0.3
	(syst)	±1.6	±1.6	±1.7	±1.7	±1.7	±1.7	±1.7	±1.7
75		18.3	18.8	18.6	19.1	18.7	19.4	19.8	19.2
	(stat)	±0.3	±0.2	±0.3	±0.3	±0.3	±0.3	±0.3	±0.3
	(syst)	±1.6	±1.7	±1.7	±1.7	±1.7	±1.7	±1.8	±1.7
77		19.1	18.2	19.0	19.1	19.4	19.4	19.8	19.6
	(stat)	±0.3	±0.2	±0.3	±0.3	±0.3	±0.3	±0.3	±0.3
	(syst)	±1.7	±1.6	±1.7	±1.7	±1.7	±1.7	±1.8	±1.7
85		19.0	18.8	19.1	19.5	19.8	19.8	19.9	19.9
	(stat)	±0.3	±0.3	±0.3	±0.3	±0.3	±0.3	±0.3	±0.3
	(syst)	±1.7	±1.7	±1.7	±1.7	±1.8	±1.8	±1.8	±1.8
90		18.7	19.2	19.3	19.4	19.3	19.9	19.9	20.3
	(stat)	±0.3	±0.3	±0.3	±0.3	±0.3	±0.3	±0.3	±0.3
	(syst)	±1.7	±1.7	±1.7	±1.7	±1.7	±1.8	±1.8	±1.8
100		19.4	19.0	19.4	19.8	19.9	20.8	20.2	20.5
	(stat)	±0.3	±0.3	±0.3	±0.3	±0.3	±0.3	±0.3	±0.3
	(syst)	±1.7	±1.7	±1.7	±1.8	±1.8	±1.8	±1.8	±1.8
105		19.1	19.0	19.5	20.1	19.9	19.8	20.3	20.6
	(stat)	±0.3	±0.3	±0.3	±0.3	±0.3	±0.3	±0.3	±0.3
	(syst)	±1.7	±1.7	±1.7	±1.8	±1.8	±1.8	±1.8	±1.8

Table 28: The theoretical cross sections, the expected cross-section limits, and the observed limits for the final selection requirement given for various m_{h_f} and $m_{H^\pm}$.

plot921.p601.tex

h_f mass (GeV)		$H^\pm$ mass (GeV)								
		30	45	50	60	75	90	120	150	175
10	$\sigma_{\rm th}$ (fb)	201159.39	166625.45	116913.71	38501.38	1610.76	571.73	164.64	70.32	41.02
	$\sigma_{95}^{\rm exp}/\sigma_{\rm th}$	—	—	3.34	11.4	4.17	27.5	7.0	13.2	25.1
		—	—	$^{+0.79}_{-1.25}$	$^{+2.7}_{-4.2}$	$^{+0.89}_{-1.47}$	$^{+6.1}_{-9.9}$	$^{+1.5}_{-2.5}$	$^{+2.8}_{-4.6}$	$^{+5.3}_{-8.8}$
	$\sigma_{95}^{\rm obs}/\sigma_{\rm th}$	—	—	3.6	12.3	5.6	35.8	9.4	17.8	33.8
11	$\sigma_{\rm th}$ (fb)	182135.63	161030.69	112983.46	35241.67	1532.02	558.95	162.56	69.44	40.42
	$\sigma_{95}^{\rm exp}/\sigma_{\rm th}$	—	1.92	—	—	—	—	—	—	—
		—	$^{+0.45}_{-0.71}$	—	—	—	—	—	—	—
	$\sigma_{95}^{\rm obs}/\sigma_{\rm th}$	—	2.26	—	—	—	—	—	—	—
12	$\sigma_{\rm th}$ (fb)	160124.15	153114.24	107034.83	31605.04	1457.13	546.46	160.51	68.57	39.82
	$\sigma_{95}^{\rm exp}/\sigma_{\rm th}$	10.6	—	—	—	—	—	—	—	—
		$^{+2.8}_{-4.2}$	—	—	—	—	—	—	—	—
	$\sigma_{95}^{\rm obs}/\sigma_{\rm th}$	6.4	—	—	—	—	—	—	—	—
13	$\sigma_{\rm th}$ (fb)	140772.81	145586.96	101399.41	28343.68	1385.90	534.24	158.48	67.70	39.24
	$\sigma_{95}^{\rm exp}/\sigma_{\rm th}$	1.25	0.57	—	—	—	—	—	—	—
		$^{+0.28}_{-0.46}$	$^{+0.13}_{-0.20}$	—	—	—	—	—	—	—
	$\sigma_{95}^{\rm obs}/\sigma_{\rm th}$	1.58	0.73	—	—	—	—	—	—	—
15	$\sigma_{\rm th}$ (fb)	98465.02	131305.54	88878.17	20191.69	1253.72	510.62	154.50	66.01	38.09
	$\sigma_{95}^{\rm exp}/\sigma_{\rm th}$	0.254	0.295	0.190	0.212	0.306	0.62	1.13	1.17	1.87
		$^{+0.055}_{-0.090}$	$^{+0.066}_{-0.107}$	$^{+0.041}_{-0.067}$	$^{+0.048}_{-0.077}$	$^{+0.063}_{-0.106}$	$^{+0.13}_{-0.22}$	$^{+0.23}_{-0.39}$	$^{+0.24}_{-0.40}$	$^{+0.38}_{-0.65}$
	$\sigma_{95}^{\rm obs}/\sigma_{\rm th}$	0.34	0.37	0.25	0.27	0.41	0.84	1.53	1.59	2.55
20	$\sigma_{\rm th}$ (fb)	19976.39	86458.30	54812.64	5571.44	1010.74	452.31	141.86	61.17	34.83
	$\sigma_{95}^{\rm exp}/\sigma_{\rm th}$	1.64	0.051	0.077	0.078	0.115	0.170	0.417	0.403	0.63
		$^{+0.36}_{-0.59}$	$^{+0.011}_{-0.018}$	$^{+0.016}_{-0.027}$	$^{+0.016}_{-0.027}$	$^{+0.024}_{-0.040}$	$^{+0.035}_{-0.059}$	$^{+0.086}_{-0.144}$	$^{+0.083}_{-0.139}$	$^{+0.13}_{-0.22}$
	$\sigma_{95}^{\rm obs}/\sigma_{\rm th}$	2.16	0.07	0.10	0.11	0.16	0.23	0.57	0.55	0.86
25	$\sigma_{\rm th}$ (fb)	760.68	41286.18	23182.83	2344.50	807.18	384.13	130.12	55.88	31.19
	$\sigma_{95}^{\rm exp}/\sigma_{\rm th}$	9.9	—	—	—	—	—	—	—	—
		$^{+2.1}_{-3.4}$	—	—	—	—	—	—	—	—
	$\sigma_{95}^{\rm obs}/\sigma_{\rm th}$	13.4	—	—	—	—	—	—	—	—
28	$\sigma_{\rm th}$ (fb)	3.82	18658.78	8993.12	1789.19	714.51	352.80	122.69	53.13	29.41
	$\sigma_{95}^{\rm exp}/\sigma_{\rm th}$	728.3	—	—	—	—	—	—	—	—
		$^{+161.0}_{-261.9}$	—	—	—	—	—	—	—	—
	$\sigma_{95}^{\rm obs}/\sigma_{\rm th}$	945.9	—	—	—	—	—	—	—	—
30	$\sigma_{\rm th}$ (fb)	—	8942.48	4053.63	1498.29	658.72	333.34	117.98	51.37	28.27
	$\sigma_{95}^{\rm exp}/\sigma_{\rm th}$	—	0.138	0.053	0.0473	0.057	0.085	0.206	0.240	0.324
		—	$^{+0.029}_{-0.049}$	$^{+0.011}_{-0.018}$	$^{+0.0097}_{-0.0164}$	$^{+0.012}_{-0.020}$	$^{+0.017}_{-0.029}$	$^{+0.042}_{-0.071}$	$^{+0.049}_{-0.083}$	$^{+0.066}_{-0.112}$
	$\sigma_{95}^{\rm obs}/\sigma_{\rm th}$	—	0.185	0.072	0.064	0.078	0.115	0.281	0.327	0.442

Table 29: The theoretical cross sections, the expected cross-section limits, and the observed limits for the final selection requirement given for various m_{h_f} and $m_{H^\pm}$.

plot921.p602.tex

h_f mass (GeV)		$H^\pm$ mass (GeV)								
		30	45	50	60	75	90	120	150	175
40	$\sigma_{\rm th}$ (fb)	—	6.10	97.85	520.20	423.54	246.67	94.20	42.77	23.71
	$\sigma_{95}^{\rm exp}/\sigma_{\rm th}$	—	11.1	0.477	0.059	0.052	0.065	0.165	0.219	0.301
		—	$^{+2.3}_{-3.8}$	$^{+0.098}_{-0.165}$	$^{+0.012}_{-0.020}$	$^{+0.011}_{-0.018}$	$^{+0.013}_{-0.023}$	$^{+0.034}_{-0.057}$	$^{+0.045}_{-0.076}$	$^{+0.062}_{-0.104}$
	$\sigma_{95}^{\rm obs}/\sigma_{\rm th}$	—	15.118	0.651	0.081	0.072	0.089	0.226	0.299	0.411
43	$\sigma_{\rm th}$ (fb)	—	0.06	15.69	309.10	363.50	223.96	88.16	40.06	22.44
	$\sigma_{95}^{\rm exp}/\sigma_{\rm th}$	—	629.7	—	—	—	—	—	—	—
		—	$^{+129.1}_{-217.6}$	—	—	—	—	—	—	—
	$\sigma_{95}^{\rm obs}/\sigma_{\rm th}$	—	858.9	—	—	—	—	—	—	—
45	$\sigma_{\rm th}$ (fb)	—	—	2.70	187.03	328.28	209.99	84.35	38.36	21.63
	$\sigma_{95}^{\rm exp}/\sigma_{\rm th}$	—	—	11.1	0.121	0.054	0.066	0.138	0.227	0.304
		—	—	$^{+2.3}_{-3.8}$	$^{+0.025}_{-0.042}$	$^{+0.011}_{-0.019}$	$^{+0.014}_{-0.023}$	$^{+0.028}_{-0.048}$	$^{+0.046}_{-0.078}$	$^{+0.062}_{-0.105}$
	$\sigma_{95}^{\rm obs}/\sigma_{\rm th}$	—	—	15.127	0.165	0.074	0.091	0.188	0.309	0.416
48	$\sigma_{\rm th}$ (fb)	—	—	0.01	67.01	267.74	188.59	78.69	36.01	20.38
	$\sigma_{95}^{\rm exp}/\sigma_{\rm th}$	—	—	1662.5	—	—	—	—	—	—
		—	—	$^{+340.6}_{-574.4}$	—	—	—	—	—	—
	$\sigma_{95}^{\rm obs}/\sigma_{\rm th}$	—	—	2268.3	—	—	—	—	—	—
50	$\sigma_{\rm th}$ (fb)	—	—	—	27.35	233.72	175.54	75.13	34.53	19.58
	$\sigma_{95}^{\rm exp}/\sigma_{\rm th}$	—	—	—	0.66	0.062	0.065	0.125	0.236	0.311
		—	—	—	$^{+0.13}_{-0.23}$	$^{+0.013}_{-0.021}$	$^{+0.013}_{-0.023}$	$^{+0.026}_{-0.043}$	$^{+0.048}_{-0.081}$	$^{+0.064}_{-0.108}$
	$\sigma_{95}^{\rm obs}/\sigma_{\rm th}$	—	—	—	0.898	0.084	0.089	0.171	0.322	0.425
55	$\sigma_{\rm th}$ (fb)	—	—	—	0.83	133.94	142.70	64.32	31.23	17.74
	$\sigma_{95}^{\rm exp}/\sigma_{\rm th}$	—	—	—	15.2	—	—	—	—	—
		—	—	—	$^{+3.1}_{-5.2}$	—	—	—	—	—
	$\sigma_{95}^{\rm obs}/\sigma_{\rm th}$	—	—	—	20.7	—	—	—	—	—
58	$\sigma_{\rm th}$ (fb)	—	—	—	0.00	72.05	122.19	58.47	28.60	16.30
	$\sigma_{95}^{\rm exp}/\sigma_{\rm th}$	—	—	—	2609.0	—	—	—	—	—
		—	—	—	$^{+534.4}_{-901.2}$	—	—	—	—	—
	$\sigma_{95}^{\rm obs}/\sigma_{\rm th}$	—	—	—	3560.6	—	—	—	—	—
60	$\sigma_{\rm th}$ (fb)	—	—	—	—	47.66	110.18	54.87	26.98	15.40
	$\sigma_{95}^{\rm exp}/\sigma_{\rm th}$	—	—	—	—	0.202	0.078	0.131	0.261	0.365
		—	—	—	—	$^{+0.041}_{-0.070}$	$^{+0.016}_{-0.027}$	$^{+0.027}_{-0.045}$	$^{+0.053}_{-0.090}$	$^{+0.075}_{-0.126}$
	$\sigma_{95}^{\rm obs}/\sigma_{\rm th}$	—	—	—	—	0.276	0.106	0.178	0.356	0.498

Table 30: The theoretical cross sections, the expected cross-section limits, and the observed limits for the final selection requirement given for various m_{h_f} and $m_{H^\pm}$.

plot921.p603.tex

h_f mass (GeV)		$H^\pm$ mass (GeV)								
		30	45	50	60	75	90	120	150	175
70	$\sigma_{\rm th}$ (fb)	—	—	—	—	0.19	42.01	37.46	19.00	11.14
	$\sigma_{95}^{\rm exp}/\sigma_{\rm th}$	—	—	—	—	35.2	0.160	0.159	0.327	0.478
		—	—	—	—	$^{+7.2}_{-12.1}$	$^{+0.033}_{-0.055}$	$^{+0.033}_{-0.055}$	$^{+0.067}_{-0.113}$	$^{+0.098}_{-0.165}$
	$\sigma_{95}^{\rm obs}/\sigma_{\rm th}$	—	—	—	—	47.991	0.219	0.218	0.446	0.652
75	$\sigma_{\rm th}$ (fb)	—	—	—	—	—	13.70	29.49	15.31	9.06
	$\sigma_{95}^{\rm exp}/\sigma_{\rm th}$	—	—	—	—	—	0.446	0.191	0.355	0.55
		—	—	—	—	—	$^{+0.091}_{-0.154}$	$^{+0.039}_{-0.066}$	$^{+0.073}_{-0.122}$	$^{+0.11}_{-0.19}$
	$\sigma_{95}^{\rm obs}/\sigma_{\rm th}$	—	—	—	—	—	0.61	0.26	0.48	0.75
77	$\sigma_{\rm th}$ (fb)	—	—	—	—	—	5.98	25.98	13.61	8.14
	$\sigma_{95}^{\rm exp}/\sigma_{\rm th}$	—	—	—	—	—	1.00	0.206	0.385	0.62
		—	—	—	—	—	$^{+0.21}_{-0.35}$	$^{+0.042}_{-0.071}$	$^{+0.079}_{-0.133}$	$^{+0.13}_{-0.21}$
	$\sigma_{95}^{\rm obs}/\sigma_{\rm th}$	—	—	—	—	—	1.37	0.28	0.52	0.85
85	$\sigma_{\rm th}$ (fb)	—	—	—	—	—	0.04	14.76	8.43	5.03
	$\sigma_{95}^{\rm exp}/\sigma_{\rm th}$	—	—	—	—	—	111.0	0.337	0.56	0.99
		—	—	—	—	—	$^{+22.7}_{-38.3}$	$^{+0.069}_{-0.117}$	$^{+0.12}_{-0.20}$	$^{+0.20}_{-0.34}$
	$\sigma_{95}^{\rm obs}/\sigma_{\rm th}$	—	—	—	—	—	151.47	0.46	0.77	1.35
90	$\sigma_{\rm th}$ (fb)	—	—	—	—	—	—	8.22	4.98	3.08
	$\sigma_{95}^{\rm exp}/\sigma_{\rm th}$	—	—	—	—	—	—	0.58	0.94	1.58
		—	—	—	—	—	—	$^{+0.12}_{-0.20}$	$^{+0.19}_{-0.32}$	$^{+0.32}_{-0.54}$
	$\sigma_{95}^{\rm obs}/\sigma_{\rm th}$	—	—	—	—	—	—	0.80	1.28	2.15
100	$\sigma_{\rm th}$ (fb)	—	—	—	—	—	—	0.65	0.73	0.46
	$\sigma_{95}^{\rm exp}/\sigma_{\rm th}$	—	—	—	—	—	—	7.0	6.0	9.8
		—	—	—	—	—	—	$^{+1.4}_{-2.4}$	$^{+1.2}_{-2.1}$	$^{+2.0}_{-3.4}$
	$\sigma_{95}^{\rm obs}/\sigma_{\rm th}$	—	—	—	—	—	—	9.6	8.2	13.4
105	$\sigma_{\rm th}$ (fb)	—	—	—	—	—	—	0.08	0.22	0.14
	$\sigma_{95}^{\rm exp}/\sigma_{\rm th}$	—	—	—	—	—	—	59.8	20.6	31.5
		—	—	—	—	—	—	$^{+12.2}_{-20.6}$	$^{+4.2}_{-7.1}$	$^{+6.5}_{-10.9}$
	$\sigma_{95}^{\rm obs}/\sigma_{\rm th}$	—	—	—	—	—	—	81.6	28.1	43.0

Table 31: The theoretical cross sections, the expected cross-section limits, and the observed limits for the final selection requirement given for various m_{h_f} and $m_{H^\pm}$.

plot921.p604.tex

h_f mass (GeV)		$H^\pm$ mass (GeV)								
		200	210	215	220	224	230	235	240	245
10	$\sigma_{\rm th}$ (fb)	26.78	23.07	21.64	20.24	19.24	17.94	17.07	16.15	15.36
	$\sigma_{95}^{\rm exp}/\sigma_{\rm th}$	60.2	58.2	66.5	—	—	—	113.2	—	—
		$^{+12.9}_{-21.3}$	$^{+12.4}_{-20.5}$	$^{+14.2}_{-23.5}$	—	—	—	$^{+24.4}_{-40.2}$	—	—
	$\sigma_{95}^{\rm obs}/\sigma_{\rm th}$	80.4	77.9	88.9	—	—	—	150.6	—	—
11	$\sigma_{\rm th}$ (fb)	26.25	22.59	21.17	19.77	18.79	17.49	16.61	15.71	14.92
	$\sigma_{95}^{\rm exp}/\sigma_{\rm th}$	—	—	—	—	—	—	—	—	—
		—	—	—	—	—	—	—	—	—
	$\sigma_{95}^{\rm obs}/\sigma_{\rm th}$	—	—	—	—	—	—	—	—	—
12	$\sigma_{\rm th}$ (fb)	25.74	22.12	20.71	19.32	18.35	17.04	16.16	15.27	14.49
	$\sigma_{95}^{\rm exp}/\sigma_{\rm th}$	—	—	—	—	—	—	—	—	—
		—	—	—	—	—	—	—	—	—
	$\sigma_{95}^{\rm obs}/\sigma_{\rm th}$	—	—	—	—	—	—	—	—	—
13	$\sigma_{\rm th}$ (fb)	25.23	21.66	20.27	18.88	17.92	16.61	15.73	14.85	14.07
	$\sigma_{95}^{\rm exp}/\sigma_{\rm th}$	—	—	—	—	—	—	—	—	—
		—	—	—	—	—	—	—	—	—
	$\sigma_{95}^{\rm obs}/\sigma_{\rm th}$	—	—	—	—	—	—	—	—	—
15	$\sigma_{\rm th}$ (fb)	24.25	20.77	19.40	18.02	17.08	15.78	14.89	14.04	13.27
	$\sigma_{95}^{\rm exp}/\sigma_{\rm th}$	3.26	4.12	5.3	6.0	6.3	7.4	9.9	—	—
		$^{+0.67}_{-1.13}$	$^{+0.85}_{-1.42}$	$^{+1.1}_{-1.8}$	$^{+1.2}_{-2.1}$	$^{+1.3}_{-2.2}$	$^{+1.5}_{-2.5}$	$^{+2.0}_{-3.4}$	—	—
	$\sigma_{95}^{\rm obs}/\sigma_{\rm th}$	4.4	5.6	7.2	8.1	8.5	10.0	13.5	—	—
20	$\sigma_{\rm th}$ (fb)	21.51	18.09	16.76	15.59	14.62	13.49	12.58	11.84	11.12
	$\sigma_{95}^{\rm exp}/\sigma_{\rm th}$	1.00	1.27	1.44	1.56	1.73	1.97	2.44	2.70	3.08
		$^{+0.20}_{-0.35}$	$^{+0.26}_{-0.44}$	$^{+0.30}_{-0.50}$	$^{+0.32}_{-0.54}$	$^{+0.35}_{-0.60}$	$^{+0.40}_{-0.68}$	$^{+0.50}_{-0.84}$	$^{+0.55}_{-0.93}$	$^{+0.63}_{-1.06}$
	$\sigma_{95}^{\rm obs}/\sigma_{\rm th}$	1.36	1.73	1.97	2.13	2.36	2.69	3.33	3.68	4.20
25	$\sigma_{\rm th}$ (fb)	18.88	15.64	14.35	13.18	12.34	11.21	10.39	9.65	9.01
	$\sigma_{95}^{\rm exp}/\sigma_{\rm th}$	—	—	—	—	—	—	—	—	—
		—	—	—	—	—	—	—	—	—
	$\sigma_{95}^{\rm obs}/\sigma_{\rm th}$	—	—	—	—	—	—	—	—	—
28	$\sigma_{\rm th}$ (fb)	17.41	14.33	13.04	11.95	11.14	10.05	9.27	8.57	7.94
	$\sigma_{95}^{\rm exp}/\sigma_{\rm th}$	—	—	—	—	—	—	—	—	—
		—	—	—	—	—	—	—	—	—
	$\sigma_{95}^{\rm obs}/\sigma_{\rm th}$	—	—	—	—	—	—	—	—	—
30	$\sigma_{\rm th}$ (fb)	16.50	13.51	12.24	11.20	10.40	9.34	8.60	7.93	7.31
	$\sigma_{95}^{\rm exp}/\sigma_{\rm th}$	0.49	0.60	0.65	0.74	0.79	0.89	0.96	1.03	1.10
		$^{+0.10}_{-0.17}$	$^{+0.12}_{-0.21}$	$^{+0.13}_{-0.22}$	$^{+0.15}_{-0.25}$	$^{+0.16}_{-0.27}$	$^{+0.18}_{-0.31}$	$^{+0.20}_{-0.33}$	$^{+0.21}_{-0.36}$	$^{+0.22}_{-0.38}$
	$\sigma_{95}^{\rm obs}/\sigma_{\rm th}$	0.67	0.82	0.89	1.01	1.08	1.21	1.31	1.41	1.49

Table 32: The theoretical cross sections, the expected cross-section limits, and the observed limits for the final selection requirement given for various m_{h_f} and $m_{H^\pm}$.

plot921.p605.tex

h_f mass (GeV)		$H^\pm$ mass (GeV)								
		200	210	215	220	224	230	235	240	245
40	$\sigma_{\rm th}$ (fb)	13.68	11.08	10.02	9.05	8.37	7.43	6.74	6.15	5.56
	$\sigma_{95}^{\rm exp}/\sigma_{\rm th}$	0.441	0.51	0.59	0.61	0.68	0.75	0.83	0.89	0.96
		$^{+0.090}_{-0.152}$	$^{+0.10}_{-0.18}$	$^{+0.12}_{-0.20}$	$^{+0.13}_{-0.21}$	$^{+0.14}_{-0.23}$	$^{+0.15}_{-0.26}$	$^{+0.17}_{-0.29}$	$^{+0.18}_{-0.31}$	$^{+0.20}_{-0.33}$
	$\sigma_{95}^{\rm obs}/\sigma_{\rm th}$	0.60	0.70	0.80	0.84	0.92	1.02	1.14	1.21	1.31
43	$\sigma_{\rm th}$ (fb)	13.04	10.56	9.55	8.62	7.97	7.09	6.45	5.88	5.31
	$\sigma_{95}^{\rm exp}/\sigma_{\rm th}$	—	—	—	—	—	—	—	—	—
		—	—	—	—	—	—	—	—	—
	$\sigma_{95}^{\rm obs}/\sigma_{\rm th}$	—	—	—	—	—	—	—	—	—
45	$\sigma_{\rm th}$ (fb)	12.63	10.23	9.24	8.35	7.71	6.86	6.27	5.70	5.15
	$\sigma_{95}^{\rm exp}/\sigma_{\rm th}$	0.434	0.52	0.56	0.62	0.66	0.72	0.78	0.86	0.97
		$^{+0.089}_{-0.150}$	$^{+0.11}_{-0.18}$	$^{+0.12}_{-0.19}$	$^{+0.13}_{-0.21}$	$^{+0.14}_{-0.23}$	$^{+0.15}_{-0.25}$	$^{+0.16}_{-0.27}$	$^{+0.18}_{-0.30}$	$^{+0.20}_{-0.33}$
	$\sigma_{95}^{\rm obs}/\sigma_{\rm th}$	0.59	0.71	0.77	0.84	0.90	0.98	1.07	1.17	1.32
48	$\sigma_{\rm th}$ (fb)	11.91	9.72	8.77	7.93	7.35	6.53	5.97	5.42	4.91
	$\sigma_{95}^{\rm exp}/\sigma_{\rm th}$	—	—	—	—	—	—	—	—	—
		—	—	—	—	—	—	—	—	—
	$\sigma_{95}^{\rm obs}/\sigma_{\rm th}$	—	—	—	—	—	—	—	—	—
50	$\sigma_{\rm th}$ (fb)	11.45	9.39	8.46	7.66	7.12	6.32	5.77	5.24	4.76
	$\sigma_{95}^{\rm exp}/\sigma_{\rm th}$	0.462	0.53	0.59	0.65	0.67	0.76	0.82	0.90	0.92
		$^{+0.095}_{-0.160}$	$^{+0.11}_{-0.18}$	$^{+0.12}_{-0.20}$	$^{+0.13}_{-0.23}$	$^{+0.14}_{-0.23}$	$^{+0.16}_{-0.26}$	$^{+0.17}_{-0.28}$	$^{+0.18}_{-0.31}$	$^{+0.19}_{-0.32}$
	$\sigma_{95}^{\rm obs}/\sigma_{\rm th}$	0.63	0.72	0.81	0.89	0.91	1.04	1.12	1.23	1.26
55	$\sigma_{\rm th}$ (fb)	10.38	8.48	7.60	6.91	6.37	5.73	5.21	4.71	4.29
	$\sigma_{95}^{\rm exp}/\sigma_{\rm th}$	—	—	—	—	—	—	—	—	—
		—	—	—	—	—	—	—	—	—
	$\sigma_{95}^{\rm obs}/\sigma_{\rm th}$	—	—	—	—	—	—	—	—	—
58	$\sigma_{\rm th}$ (fb)	9.65	7.84	7.12	6.43	5.96	5.31	4.86	4.38	4.02
	$\sigma_{95}^{\rm exp}/\sigma_{\rm th}$	—	—	—	—	—	—	—	—	—
		—	—	—	—	—	—	—	—	—
	$\sigma_{95}^{\rm obs}/\sigma_{\rm th}$	—	—	—	—	—	—	—	—	—
60	$\sigma_{\rm th}$ (fb)	9.19	7.44	6.82	6.13	5.70	5.05	4.64	4.17	3.85
	$\sigma_{95}^{\rm exp}/\sigma_{\rm th}$	0.52	0.64	0.68	0.74	0.79	0.88	0.94	1.05	1.11
		$^{+0.11}_{-0.18}$	$^{+0.13}_{-0.22}$	$^{+0.14}_{-0.23}$	$^{+0.15}_{-0.26}$	$^{+0.16}_{-0.27}$	$^{+0.18}_{-0.30}$	$^{+0.19}_{-0.33}$	$^{+0.22}_{-0.36}$	$^{+0.23}_{-0.38}$
	$\sigma_{95}^{\rm obs}/\sigma_{\rm th}$	0.72	0.87	0.93	1.01	1.07	1.20	1.28	1.44	1.52

Table 33: The theoretical cross sections, the expected cross-section limits, and the observed limits for the final selection requirement given for various m_{h_f} and $m_{H^\pm}$.

plot921.p606.tex

h_f mass (GeV)		$H^\pm$ mass (GeV)								
		200	210	215	220	224	230	235	240	245
70	$\sigma_{\rm th}$ (fb)	6.59	5.45	4.98	4.54	4.17	3.70	3.42	3.07	2.82
	$\sigma_{95}^{\rm exp}/\sigma_{\rm th}$	0.69	0.82	0.89	0.95	0.99	1.10	1.20	1.32	1.43
		$^{+0.14}_{-0.24}$	$^{+0.17}_{-0.28}$	$^{+0.18}_{-0.31}$	$^{+0.20}_{-0.33}$	$^{+0.20}_{-0.34}$	$^{+0.23}_{-0.38}$	$^{+0.25}_{-0.42}$	$^{+0.27}_{-0.46}$	$^{+0.29}_{-0.50}$
	$\sigma_{95}^{\rm obs}/\sigma_{\rm th}$	0.94	1.12	1.22	1.30	1.35	1.50	1.64	1.80	1.96
75	$\sigma_{\rm th}$ (fb)	5.46	4.50	4.03	3.72	3.44	3.04	2.82	2.59	2.33
	$\sigma_{95}^{\rm exp}/\sigma_{\rm th}$	0.81	0.97	1.06	1.14	1.22	1.35	1.45	1.51	1.70
		$^{+0.17}_{-0.28}$	$^{+0.20}_{-0.33}$	$^{+0.22}_{-0.36}$	$^{+0.23}_{-0.39}$	$^{+0.25}_{-0.42}$	$^{+0.28}_{-0.47}$	$^{+0.30}_{-0.50}$	$^{+0.31}_{-0.52}$	$^{+0.35}_{-0.59}$
	$\sigma_{95}^{\rm obs}/\sigma_{\rm th}$	1.10	1.32	1.44	1.55	1.67	1.84	1.97	2.07	2.33
77	$\sigma_{\rm th}$ (fb)	4.90	4.05	3.64	3.33	3.09	2.76	2.53	2.33	2.11
	$\sigma_{95}^{\rm exp}/\sigma_{\rm th}$	0.91	1.06	1.17	1.25	1.33	1.44	1.56	1.71	1.86
		$^{+0.19}_{-0.31}$	$^{+0.22}_{-0.37}$	$^{+0.24}_{-0.41}$	$^{+0.26}_{-0.43}$	$^{+0.27}_{-0.46}$	$^{+0.29}_{-0.50}$	$^{+0.32}_{-0.54}$	$^{+0.35}_{-0.59}$	$^{+0.38}_{-0.64}$
	$\sigma_{95}^{\rm obs}/\sigma_{\rm th}$	1.24	1.45	1.60	1.71	1.82	1.96	2.13	2.33	2.54
85	$\sigma_{\rm th}$ (fb)	3.10	2.54	2.32	2.12	1.96	1.76	1.61	1.48	1.33
	$\sigma_{95}^{\rm exp}/\sigma_{\rm th}$	1.42	1.66	1.78	1.93	2.08	2.25	2.47	2.66	2.89
		$^{+0.29}_{-0.49}$	$^{+0.34}_{-0.57}$	$^{+0.36}_{-0.61}$	$^{+0.40}_{-0.67}$	$^{+0.43}_{-0.72}$	$^{+0.46}_{-0.78}$	$^{+0.51}_{-0.85}$	$^{+0.55}_{-0.92}$	$^{+0.59}_{-1.00}$
	$\sigma_{95}^{\rm obs}/\sigma_{\rm th}$	1.94	2.27	2.43	2.63	2.83	3.07	3.38	3.64	3.94
90	$\sigma_{\rm th}$ (fb)	1.86	1.55	1.41	1.29	1.20	1.07	0.98	0.89	0.82
	$\sigma_{95}^{\rm exp}/\sigma_{\rm th}$	2.37	2.68	2.99	3.10	3.33	3.67	3.90	4.20	4.73
		$^{+0.49}_{-0.82}$	$^{+0.55}_{-0.93}$	$^{+0.61}_{-1.03}$	$^{+0.63}_{-1.07}$	$^{+0.68}_{-1.15}$	$^{+0.75}_{-1.27}$	$^{+0.80}_{-1.35}$	$^{+0.86}_{-1.45}$	$^{+0.97}_{-1.63}$
	$\sigma_{95}^{\rm obs}/\sigma_{\rm th}$	3.23	3.66	4.08	4.23	4.54	5.00	5.33	5.74	6.46
100	$\sigma_{\rm th}$ (fb)	0.28	0.23	0.21	0.20	0.18	0.16	0.15	0.14	0.13
	$\sigma_{95}^{\rm exp}/\sigma_{\rm th}$	15.6	17.9	19.5	20.8	22.1	24.1	25.8	27.2	29.9
		$^{+3.2}_{-5.4}$	$^{+3.7}_{-6.2}$	$^{+4.0}_{-6.7}$	$^{+4.3}_{-7.2}$	$^{+4.5}_{-7.6}$	$^{+4.9}_{-8.3}$	$^{+5.3}_{-8.9}$	$^{+5.6}_{-9.4}$	$^{+6.1}_{-10.3}$
	$\sigma_{95}^{\rm obs}/\sigma_{\rm th}$	21.3	24.4	26.6	28.3	30.2	32.9	35.2	37.1	40.8
105	$\sigma_{\rm th}$ (fb)	0.08	0.07	0.07	0.06	0.06	0.05	0.05	0.04	0.04
	$\sigma_{95}^{\rm exp}/\sigma_{\rm th}$	52.2	58.6	63.6	66.7	71.3	79.2	83.5	91.0	98.5
		$^{+10.7}_{-18.0}$	$^{+12.0}_{-20.2}$	$^{+13.0}_{-22.0}$	$^{+13.7}_{-23.0}$	$^{+14.6}_{-24.6}$	$^{+16.2}_{-27.4}$	$^{+17.1}_{-28.8}$	$^{+18.6}_{-31.4}$	$^{+20.2}_{-34.0}$
	$\sigma_{95}^{\rm obs}/\sigma_{\rm th}$	71.2	80.0	86.8	91.0	97.3	108.1	114.0	124.3	134.5

Table 34: The theoretical cross sections, the expected cross-section limits, and the observed limits for the final selection requirement given for various m_{h_f} and $m_{H^\pm}$.

plot921.p607.tex

h_f mass (GeV)		$H^\pm$ mass (GeV) 248	250	260	270	275	285	290	300
10	$\sigma_{\rm th}$ (fb)	14.93	14.62	13.38	12.42	11.95	11.12	10.75	10.16
	$\sigma_{95}^{\rm exp}/\sigma_{\rm th}$	—	1000.6	—	—	431.4	—	—	704.9
		—	$^{+245.8}_{-381.4}$	—	—	$^{+98.4}_{-157.8}$	—	—	$^{+163.5}_{-260.2}$
	$\sigma_{95}^{\rm obs}/\sigma_{\rm th}$	—	913.6	—	—	530.3	—	—	828.2
11	$\sigma_{\rm th}$ (fb)	14.49	14.19	12.96	11.99	11.53	10.72	10.37	9.78
	$\sigma_{95}^{\rm exp}/\sigma_{\rm th}$	—	—	—	—	—	—	—	—
		—	—	—	—	—	—	—	—
	$\sigma_{95}^{\rm obs}/\sigma_{\rm th}$	—	—	—	—	—	—	—	—
12	$\sigma_{\rm th}$ (fb)	14.07	13.76	12.55	11.58	11.13	10.33	9.99	9.41
	$\sigma_{95}^{\rm exp}/\sigma_{\rm th}$	—	—	—	—	—	—	—	—
		—	—	—	—	—	—	—	—
	$\sigma_{95}^{\rm obs}/\sigma_{\rm th}$	—	—	—	—	—	—	—	—
13	$\sigma_{\rm th}$ (fb)	13.66	13.35	12.15	11.18	10.75	9.96	9.63	9.05
	$\sigma_{95}^{\rm exp}/\sigma_{\rm th}$	—	—	—	—	—	—	—	—
		—	—	—	—	—	—	—	—
	$\sigma_{95}^{\rm obs}/\sigma_{\rm th}$	—	—	—	—	—	—	—	—
15	$\sigma_{\rm th}$ (fb)	12.87	12.57	11.40	10.43	10.01	9.26	8.95	8.38
	$\sigma_{95}^{\rm exp}/\sigma_{\rm th}$	—	13.2	—	—	28.5	—	—	58.9
		—	$^{+2.7}_{-4.6}$	—	—	$^{+5.9}_{-9.9}$	—	—	$^{+12.3}_{-20.5}$
	$\sigma_{95}^{\rm obs}/\sigma_{\rm th}$	—	18.0	—	—	38.7	—	—	79.6
20	$\sigma_{\rm th}$ (fb)	10.72	10.46	9.41	8.49	8.10	7.40	7.09	6.54
	$\sigma_{95}^{\rm exp}/\sigma_{\rm th}$	3.37	3.67	4.47	5.4	6.6	8.0	8.4	10.2
		$^{+0.69}_{-1.16}$	$^{+0.75}_{-1.27}$	$^{+0.92}_{-1.54}$	$^{+1.1}_{-1.9}$	$^{+1.4}_{-2.3}$	$^{+1.6}_{-2.8}$	$^{+1.7}_{-2.9}$	$^{+2.1}_{-3.5}$
	$\sigma_{95}^{\rm obs}/\sigma_{\rm th}$	4.6	5.0	6.1	7.3	9.0	10.9	11.5	13.9
25	$\sigma_{\rm th}$ (fb)	8.62	8.37	7.36	6.50	6.14	5.52	5.25	4.77
	$\sigma_{95}^{\rm exp}/\sigma_{\rm th}$	—	—	—	—	—	—	—	—
		—	—	—	—	—	—	—	—
	$\sigma_{95}^{\rm obs}/\sigma_{\rm th}$	—	—	—	—	—	—	—	—
28	$\sigma_{\rm th}$ (fb)	7.56	7.31	6.35	5.53	5.18	4.58	4.30	3.85
	$\sigma_{95}^{\rm exp}/\sigma_{\rm th}$	—	—	—	—	—	—	—	—
		—	—	—	—	—	—	—	—
	$\sigma_{95}^{\rm obs}/\sigma_{\rm th}$	—	—	—	—	—	—	—	—
30	$\sigma_{\rm th}$ (fb)	6.93	6.69	5.76	4.97	4.62	4.05	3.77	3.33
	$\sigma_{95}^{\rm exp}/\sigma_{\rm th}$	1.24	1.30	1.55	1.99	2.11	2.52	2.74	3.48
		$^{+0.25}_{-0.43}$	$^{+0.27}_{-0.45}$	$^{+0.32}_{-0.54}$	$^{+0.41}_{-0.69}$	$^{+0.43}_{-0.73}$	$^{+0.52}_{-0.87}$	$^{+0.56}_{-0.95}$	$^{+0.71}_{-1.20}$
	$\sigma_{95}^{\rm obs}/\sigma_{\rm th}$	1.69	1.77	2.12	2.72	2.88	3.44	3.73	4.75

Table 35: The theoretical cross sections, the expected cross-section limits, and the observed limits for the final selection requirement given for various m_{h_f} and $m_{H^\pm}$.

plot921.p608.tex

h_f mass (GeV)		$H^\pm$ mass (GeV)							
		248	250	260	270	275	285	290	300
40	$\sigma_{\rm th}$ (fb)	5.28	5.11	4.20	3.52	3.23	2.74	2.54	2.12
	$\sigma_{95}^{\rm exp}/\sigma_{\rm th}$	1.00	1.07	1.22	1.50	1.65	2.00	2.13	2.59
		$^{+0.20}_{-0.34}$	$^{+0.22}_{-0.37}$	$^{+0.25}_{-0.42}$	$^{+0.31}_{-0.52}$	$^{+0.34}_{-0.57}$	$^{+0.41}_{-0.69}$	$^{+0.44}_{-0.74}$	$^{+0.53}_{-0.89}$
	$\sigma_{95}^{\rm obs}/\sigma_{\rm th}$	1.36	1.45	1.67	2.05	2.25	2.72	2.90	3.53
43	$\sigma_{\rm th}$ (fb)	5.02	4.86	4.03	3.37	3.09	2.62	2.41	2.03
	$\sigma_{95}^{\rm exp}/\sigma_{\rm th}$	—	—	—	—	—	—	—	—
		—	—	—	—	—	—	—	—
	$\sigma_{95}^{\rm obs}/\sigma_{\rm th}$	—	—	—	—	—	—	—	—
45	$\sigma_{\rm th}$ (fb)	4.86	4.70	3.93	3.27	3.01	2.55	2.33	1.98
	$\sigma_{95}^{\rm exp}/\sigma_{\rm th}$	1.00	1.04	1.24	1.48	1.53	1.85	2.06	2.43
		$^{+0.21}_{-0.35}$	$^{+0.21}_{-0.36}$	$^{+0.25}_{-0.43}$	$^{+0.30}_{-0.51}$	$^{+0.31}_{-0.53}$	$^{+0.38}_{-0.64}$	$^{+0.42}_{-0.71}$	$^{+0.50}_{-0.84}$
	$\sigma_{95}^{\rm obs}/\sigma_{\rm th}$	1.37	1.42	1.69	2.01	2.09	2.53	2.81	3.32
48	$\sigma_{\rm th}$ (fb)	4.64	4.48	3.73	3.13	2.88	2.42	2.23	1.88
	$\sigma_{95}^{\rm exp}/\sigma_{\rm th}$	—	—	—	—	—	—	—	—
		—	—	—	—	—	—	—	—
	$\sigma_{95}^{\rm obs}/\sigma_{\rm th}$	—	—	—	—	—	—	—	—
50	$\sigma_{\rm th}$ (fb)	4.50	4.35	3.60	3.04	2.79	2.34	2.16	1.82
	$\sigma_{95}^{\rm exp}/\sigma_{\rm th}$	1.02	1.08	1.27	1.46	1.58	1.92	2.06	2.45
		$^{+0.21}_{-0.35}$	$^{+0.22}_{-0.37}$	$^{+0.26}_{-0.44}$	$^{+0.30}_{-0.50}$	$^{+0.32}_{-0.55}$	$^{+0.39}_{-0.66}$	$^{+0.42}_{-0.71}$	$^{+0.50}_{-0.85}$
	$\sigma_{95}^{\rm obs}/\sigma_{\rm th}$	1.39	1.47	1.73	1.99	2.15	2.62	2.81	3.34
55	$\sigma_{\rm th}$ (fb)	4.07	3.93	3.28	2.74	2.52	2.12	1.95	1.65
	$\sigma_{95}^{\rm exp}/\sigma_{\rm th}$	—	—	—	—	—	—	—	—
		—	—	—	—	—	—	—	—
	$\sigma_{95}^{\rm obs}/\sigma_{\rm th}$	—	—	—	—	—	—	—	—
58	$\sigma_{\rm th}$ (fb)	3.78	3.67	3.06	2.56	2.35	1.99	1.81	1.54
	$\sigma_{95}^{\rm exp}/\sigma_{\rm th}$	—	—	—	—	—	—	—	—
		—	—	—	—	—	—	—	—
	$\sigma_{95}^{\rm obs}/\sigma_{\rm th}$	—	—	—	—	—	—	—	—
60	$\sigma_{\rm th}$ (fb)	3.60	3.51	2.93	2.44	2.25	1.90	1.72	1.48
	$\sigma_{95}^{\rm exp}/\sigma_{\rm th}$	1.18	1.22	1.42	1.66	1.80	2.10	2.37	2.68
		$^{+0.24}_{-0.41}$	$^{+0.25}_{-0.42}$	$^{+0.29}_{-0.49}$	$^{+0.34}_{-0.57}$	$^{+0.37}_{-0.62}$	$^{+0.43}_{-0.73}$	$^{+0.49}_{-0.82}$	$^{+0.55}_{-0.93}$
	$\sigma_{95}^{\rm obs}/\sigma_{\rm th}$	1.61	1.66	1.93	2.26	2.46	2.87	3.24	3.66

Table 36: The theoretical cross sections, the expected cross-section limits, and the observed limits for the final selection requirement given for various m_{h_f} and $m_{H^\pm}$.

plot921.p609.tex

h_f mass (GeV)		$H^\pm$ mass (GeV)							
		248	250	260	270	275	285	290	300
70	$\sigma_{\rm th}$ (fb)	2.65	2.60	2.17	1.81	1.66	1.40	1.31	1.10
	$\sigma_{95}^{\rm exp}/\sigma_{\rm th}$	1.51	1.54	1.78	2.14	2.34	2.66	2.93	3.39
		$^{+0.31}_{-0.52}$	$^{+0.32}_{-0.53}$	$^{+0.36}_{-0.62}$	$^{+0.44}_{-0.74}$	$^{+0.48}_{-0.81}$	$^{+0.54}_{-0.92}$	$^{+0.60}_{-1.01}$	$^{+0.69}_{-1.17}$
	$\sigma_{95}^{\rm obs}/\sigma_{\rm th}$	2.07	2.10	2.43	2.92	3.19	3.63	4.00	4.63
75	$\sigma_{\rm th}$ (fb)	2.21	2.13	1.79	1.50	1.38	1.17	1.08	0.92
	$\sigma_{95}^{\rm exp}/\sigma_{\rm th}$	1.78	1.80	2.17	2.51	2.79	3.17	3.38	4.10
		$^{+0.36}_{-0.62}$	$^{+0.37}_{-0.62}$	$^{+0.45}_{-0.75}$	$^{+0.51}_{-0.87}$	$^{+0.57}_{-0.96}$	$^{+0.65}_{-1.10}$	$^{+0.69}_{-1.17}$	$^{+0.84}_{-1.41}$
	$\sigma_{95}^{\rm obs}/\sigma_{\rm th}$	2.43	2.46	2.97	3.43	3.81	4.33	4.61	5.59
77	$\sigma_{\rm th}$ (fb)	2.00	1.93	1.62	1.36	1.25	1.06	0.97	0.83
	$\sigma_{95}^{\rm exp}/\sigma_{\rm th}$	1.89	2.05	2.34	2.77	2.97	3.52	3.76	4.45
		$^{+0.39}_{-0.65}$	$^{+0.42}_{-0.71}$	$^{+0.48}_{-0.81}$	$^{+0.57}_{-0.96}$	$^{+0.61}_{-1.03}$	$^{+0.72}_{-1.22}$	$^{+0.77}_{-1.30}$	$^{+0.91}_{-1.54}$
	$\sigma_{95}^{\rm obs}/\sigma_{\rm th}$	2.58	2.80	3.20	3.78	4.05	4.81	5.13	6.07
85	$\sigma_{\rm th}$ (fb)	1.27	1.24	1.03	0.87	0.80	0.68	0.63	0.53
	$\sigma_{95}^{\rm exp}/\sigma_{\rm th}$	2.99	3.10	3.65	4.26	4.55	5.3	5.8	6.8
		$^{+0.61}_{-1.03}$	$^{+0.63}_{-1.07}$	$^{+0.75}_{-1.26}$	$^{+0.87}_{-1.47}$	$^{+0.93}_{-1.57}$	$^{+1.1}_{-1.8}$	$^{+1.2}_{-2.0}$	$^{+1.4}_{-2.4}$
	$\sigma_{95}^{\rm obs}/\sigma_{\rm th}$	4.1	4.2	5.0	5.8	6.2	7.3	7.9	9.3
90	$\sigma_{\rm th}$ (fb)	0.77	0.76	0.63	0.55	0.49	0.42	0.38	0.33
	$\sigma_{95}^{\rm exp}/\sigma_{\rm th}$	5.0	5.0	5.9	6.8	7.6	8.7	9.5	10.8
		$^{+1.0}_{-1.7}$	$^{+1.0}_{-1.7}$	$^{+1.2}_{-2.0}$	$^{+1.4}_{-2.3}$	$^{+1.6}_{-2.6}$	$^{+1.8}_{-3.0}$	$^{+1.9}_{-3.3}$	$^{+2.2}_{-3.7}$
	$\sigma_{95}^{\rm obs}/\sigma_{\rm th}$	6.8	6.8	8.0	9.3	10.4	11.9	13.0	14.7
100	$\sigma_{\rm th}$ (fb)	0.12	0.12	0.10	0.08	0.08	0.07	0.06	0.05
	$\sigma_{95}^{\rm exp}/\sigma_{\rm th}$	30.7	32.7	37.4	43.5	47.1	53.1	58.8	68.2
		$^{+6.3}_{-10.6}$	$^{+6.7}_{-11.3}$	$^{+7.7}_{-12.9}$	$^{+8.9}_{-15.0}$	$^{+9.6}_{-16.3}$	$^{+10.9}_{-18.3}$	$^{+12.0}_{-20.3}$	$^{+14.0}_{-23.6}$
	$\sigma_{95}^{\rm obs}/\sigma_{\rm th}$	41.9	44.7	51.1	59.3	64.2	72.4	80.3	93.1
105	$\sigma_{\rm th}$ (fb)	0.04	0.04	0.03	0.03	0.02	0.02	0.02	0.02
	$\sigma_{95}^{\rm exp}/\sigma_{\rm th}$	101.7	104.9	120.5	141.1	152.3	181.9	191.5	222.2
		$^{+20.8}_{-35.1}$	$^{+21.5}_{-36.2}$	$^{+24.7}_{-41.6}$	$^{+28.9}_{-48.7}$	$^{+31.2}_{-52.6}$	$^{+37.2}_{-62.8}$	$^{+39.2}_{-66.1}$	$^{+45.5}_{-76.7}$
	$\sigma_{95}^{\rm obs}/\sigma_{\rm th}$	138.9	143.2	164.5	192.6	207.9	248.2	261.4	303.3

Table 37: Excluded mass regions based on the $\pm 2\sigma$, $\pm\sigma$, expected, and observed cross-section limits for the final selection requirement.

plot921.p700.tex

			$H^{\pm}$ mass (GeV)							
			30	45	50	60	75	90	120	150
$+2\sigma$ exclusion	Min	(GeV)	14.1	13.4	13.3	13.9	14.0	15.7	18.8	18.7
	Max	(GeV)	16.9	33.0	40.2	49.3	61.9	75.4	89.1	83.6
$+1\sigma$ exclusion	Min	(GeV)	13.5	12.4	12.5	13.3	13.1	14.6	16.5	16.6
	Max	(GeV)	18.1	34.1	40.9	50.4	62.7	76.5	91.4	88.8
Expected exclusion	Min	(GeV)	13.3	12.1	12.1	13.1	12.7	14.4	15.6	15.7
	Max	(GeV)	18.7	34.5	41.2	50.7	63.1	77.0	92.2	90.3
-1σ exclusion	Min	(GeV)	12.9	11.3	11.3	12.5	11.9	13.8	14.2	14.4
	Max	(GeV)	19.9	35.5	41.9	51.3	63.9	77.7	93.9	92.6
-2σ exclusion	Min	(GeV)	12.8	10.0	10.9	12.2	11.5	13.5	13.5	14.0
	Max	(GeV)	20.5	36.0	42.2	51.7	64.4	78.1	94.8	93.9
Observed exclusion	Min	(GeV)	13.6	12.4	12.4	13.3	13.3	14.8	17.2	17.2
	Max	(GeV)	17.9	33.8	40.7	50.2	62.5	76.2	90.9	87.6

			$H^{\pm}$ mass (GeV)								
			175	200	210	215	220	224	230	235	240
$+2\sigma$ exclusion	Min	(GeV)	22.7	29.1	38.0	—	—	—	—	—	—
	Max	(GeV)	73.4	60.2	50.2	—	—	—	—	—	—
$+1\sigma$ exclusion	Min	(GeV)	18.8	22.6	25.7	26.9	28.4	29.4	34.0	40.2	—
	Max	(GeV)	82.0	75.5	70.4	67.4	64.5	62.3	56.3	50.9	—
Expected exclusion	Min	(GeV)	17.9	20.0	23.2	24.6	25.9	27.0	28.5	29.6	32.1
	Max	(GeV)	85.2	78.8	75.7	73.4	71.4	70.3	65.8	62.5	56.7
-1σ exclusion	Min	(GeV)	15.9	18.2	19.2	19.8	20.3	21.6	23.2	25.0	25.9
	Max	(GeV)	89.7	85.7	83.5	82.1	80.7	79.5	78.1	76.4	75.1
-2σ exclusion	Min	(GeV)	14.9	17.2	18.2	18.9	19.2	19.6	20.3	22.5	23.5
	Max	(GeV)	91.1	88.0	86.6	85.8	85.0	83.7	82.2	80.7	79.2
Observed exclusion	Min	(GeV)	19.3	24.4	27.4	28.5	30.3	34.9	42.6	—	—
	Max	(GeV)	79.8	71.9	65.6	62.8	59.2	55.6	46.9	—	—

			$H^{\pm}$ mass (GeV)								
			245	248	250	260	270	275	285	290	300
$+2\sigma$ exclusion	Min	(GeV)	—	—	—	—	—	—	—	—	—
	Max	(GeV)	—	—	—	—	—	—	—	—	—
$+1\sigma$ exclusion	Min	(GeV)	—	—	—	—	—	—	—	—	—
	Max	(GeV)	—	—	—	—	—	—	—	—	—
Expected exclusion	Min	(GeV)	36.8	39.8	—	—	—	—	—	—	—
	Max	(GeV)	54.2	43.0	—	—	—	—	—	—	—
-1σ exclusion	Min	(GeV)	26.8	27.9	28.4	30.7	39.4	—	—	—	—
	Max	(GeV)	71.8	70.3	69.6	63.3	53.7	—	—	—	—
-2σ exclusion	Min	(GeV)	24.5	25.6	26.2	28.0	31.2	33.7	42.3	—	—
	Max	(GeV)	77.6	77.3	76.0	72.0	65.9	62.6	50.5	—	—
Observed exclusion	Min	(GeV)	—	—	—	—	—	—	—	—	—
	Max	(GeV)	—	—	—	—	—	—	—	—	—

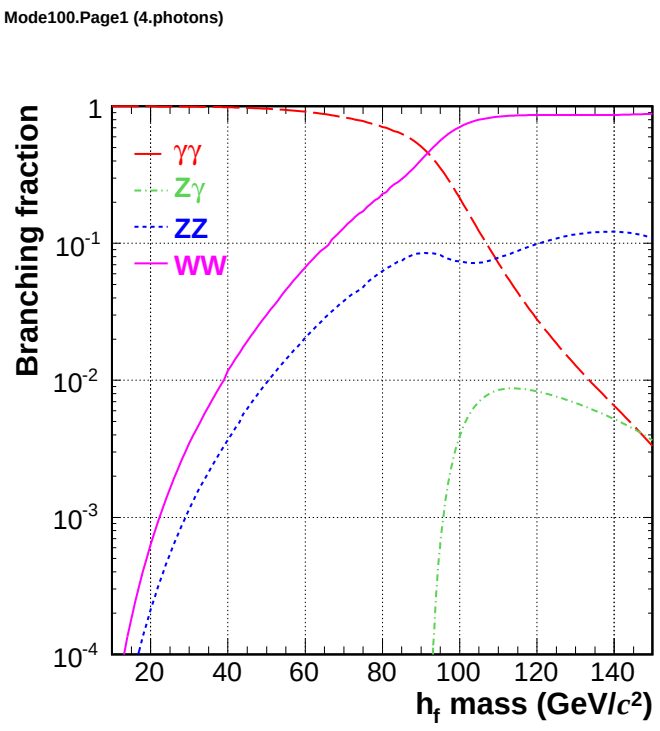

Figure 1: Branching fractions of $h_f \to XY$.

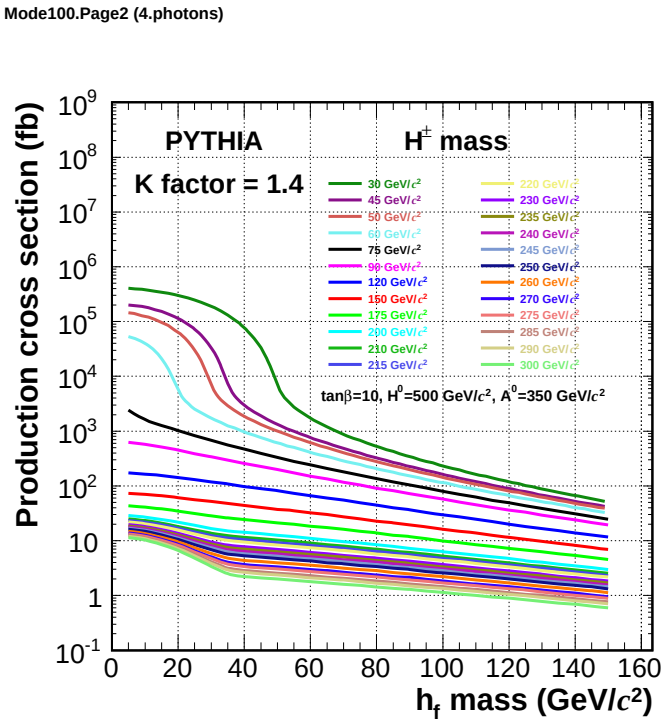

Figure 2: Production cross section.

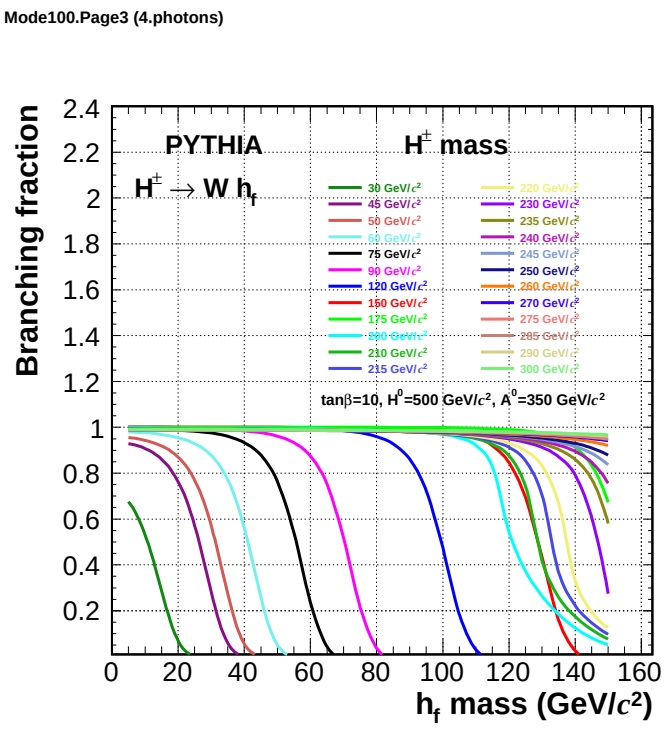

Figure 3: Branching fractions of $H^{\pm} \to W h_f$ ($\tan\beta = 10$).

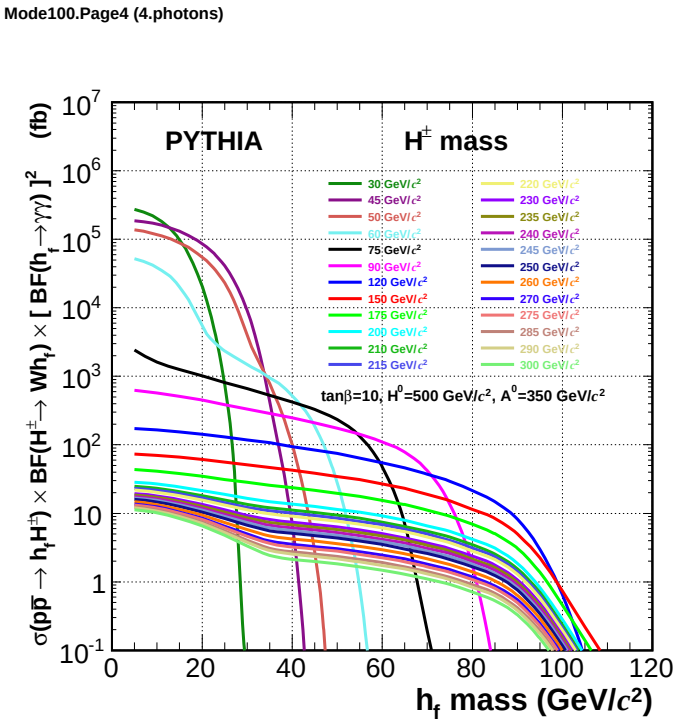

Figure 4: Cross section for $p\bar{p} \to h_f H^{\pm} \to h_f h_f W \to \gamma\gamma\gamma\gamma + X$.

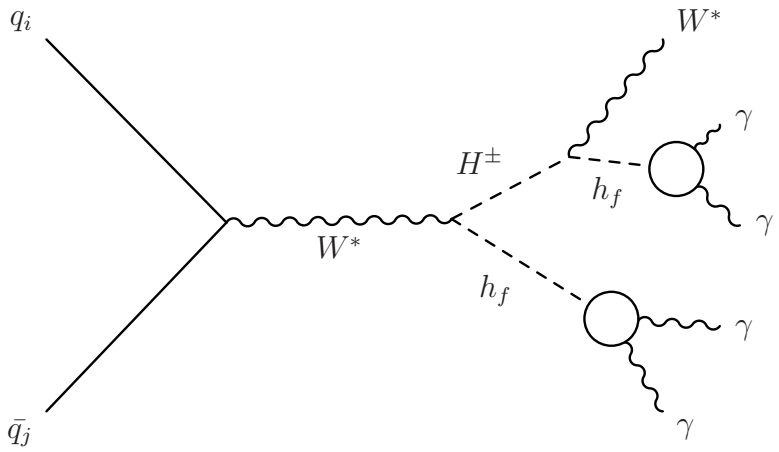

Figure 5: A Feynman diagram for the fermiophobic higgs production and decay.

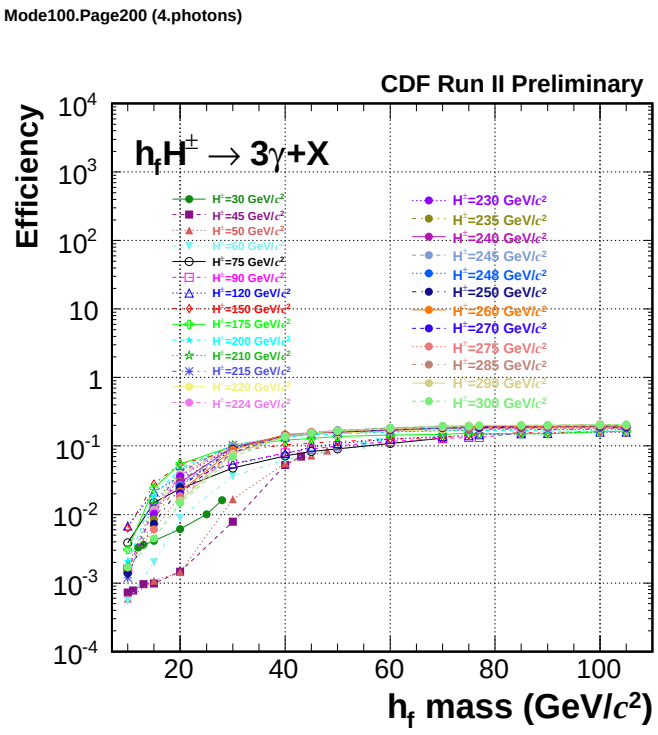

Figure 6: Efficiencies of the h_f detection.

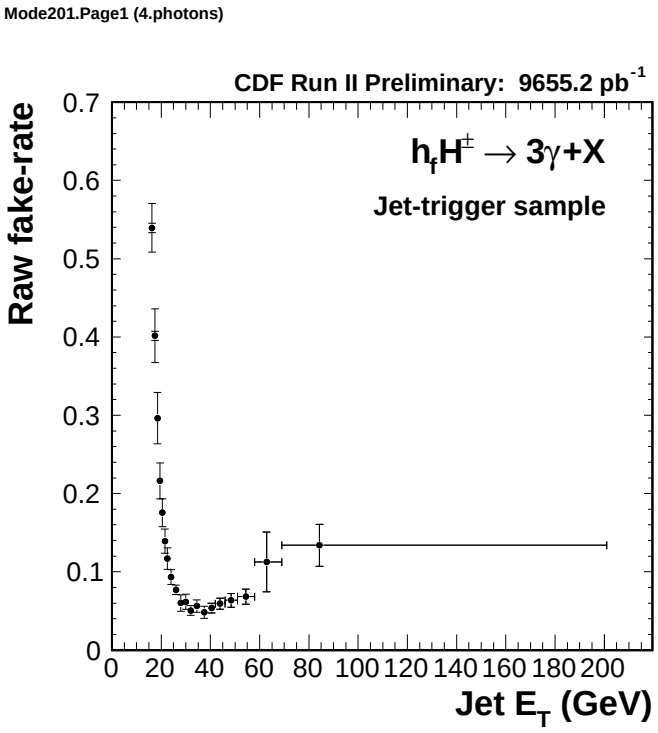

Figure 7: Raw fake-rates (P_{raw}) with statistical uncertainties for the combined jet datasets (JET20, JET50, JET70, and JET100).

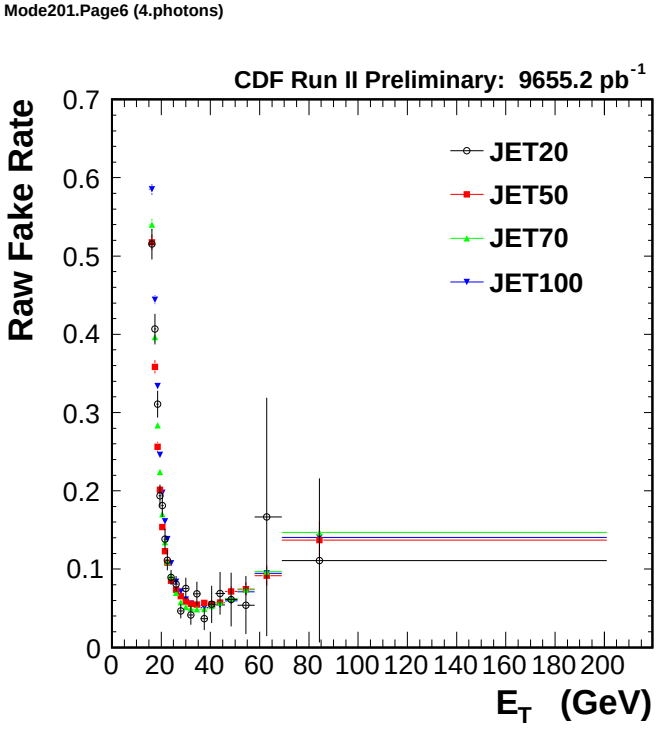

Figure 8: Raw fake-rates (P_{raw}) obtained from the different jet datasets (JET20, JET50, JET70, and JET100).

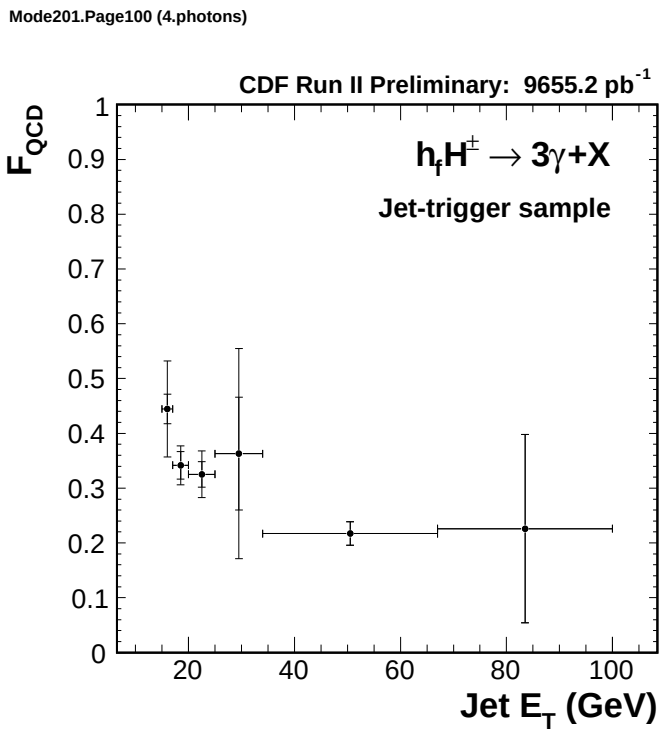

Figure 9: Measurements of the $F_{\rm QCD}$ using the isolation vs. CES-χ^2 method with statistical (inner error-bars) and total errors (outer error-bars) for the combined jet datasets (JET20, JET50, JET70, and JET100).

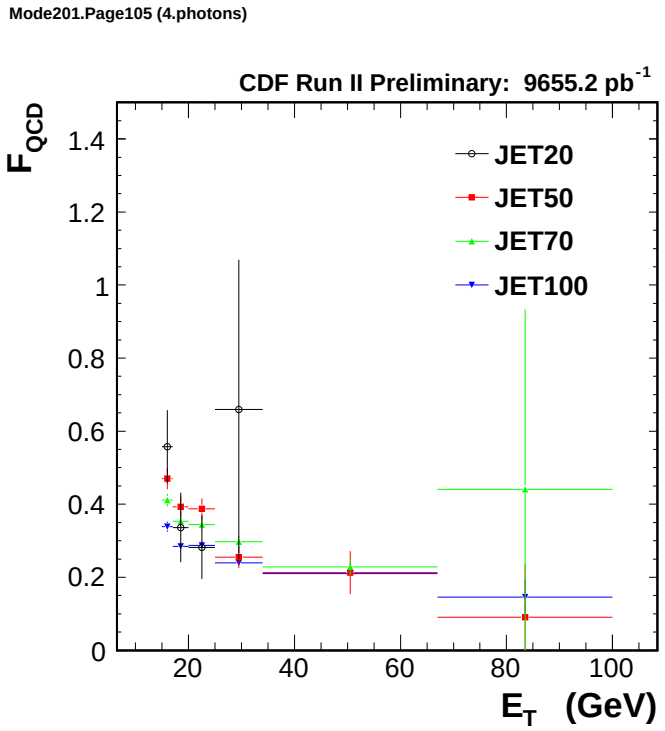

Figure 10: Measurements of the $F_{\rm QCD}$ using the isolation vs. CES-χ^2 method for the different jet datasets (JET20, JET50, JET70, and JET100).

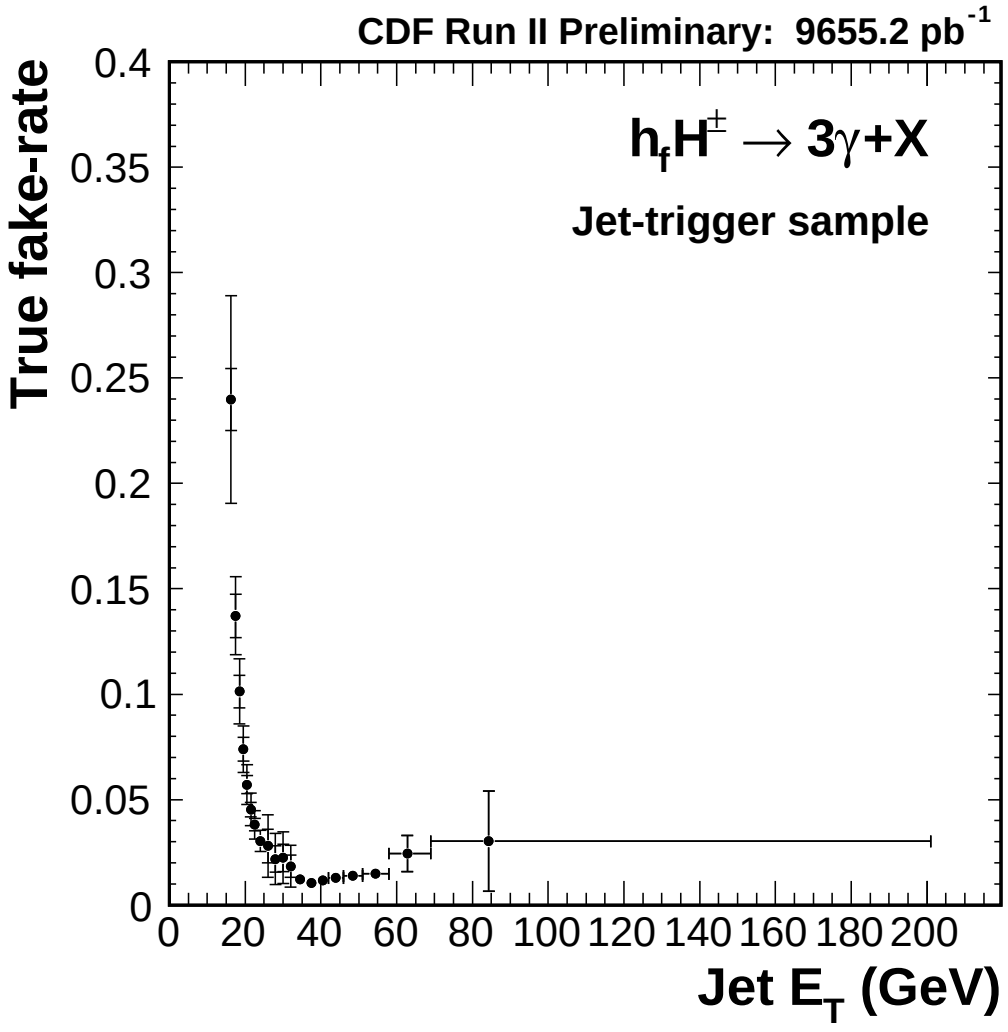

Figure 11: True fake-rates (P_{true}) with statistical errors (inner error-bars) and total errors (outer error-bars) for the combined jet datasets (`JET20`, `JET50`, `JET70`, and `JET100`).

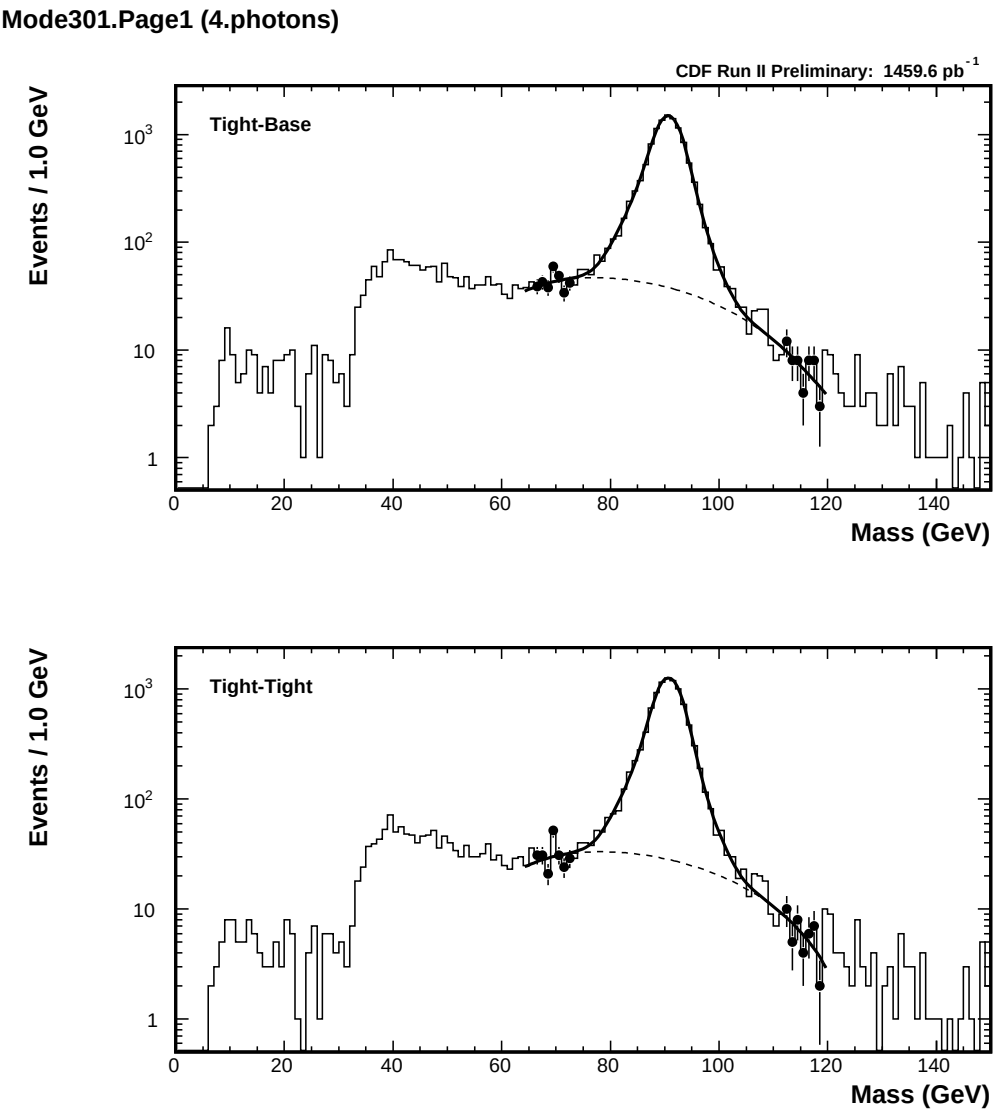

Figure 12: Dielectron invariant-mass distributions for the photon efficiency measurement. The data correspond to the periods 0–9.

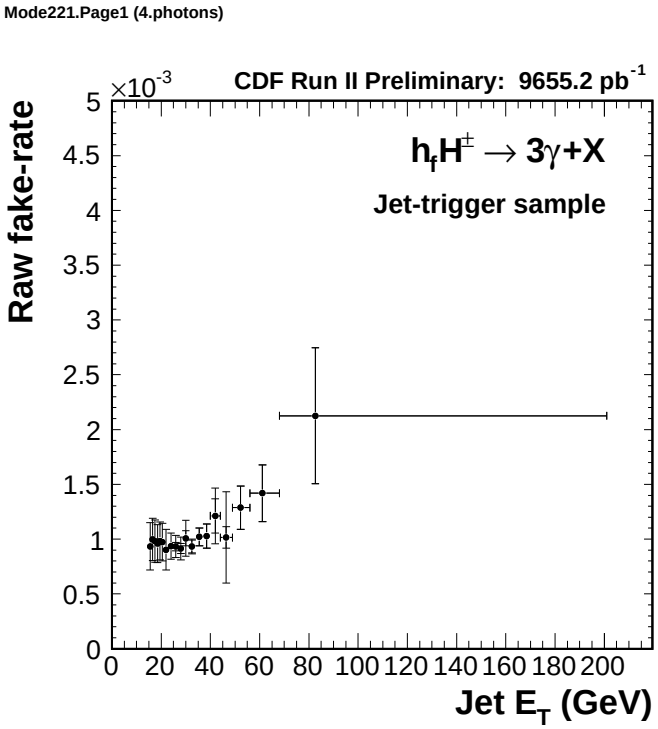

Figure 13: Raw fake-rates corresponding to the loose denominator cuts ($P'_{\rm raw}$) with statistical errors (inner error-bars) and total errors (outer error-bars) for the combined jet datasets (JET20, JET50, JET70, and JET100).

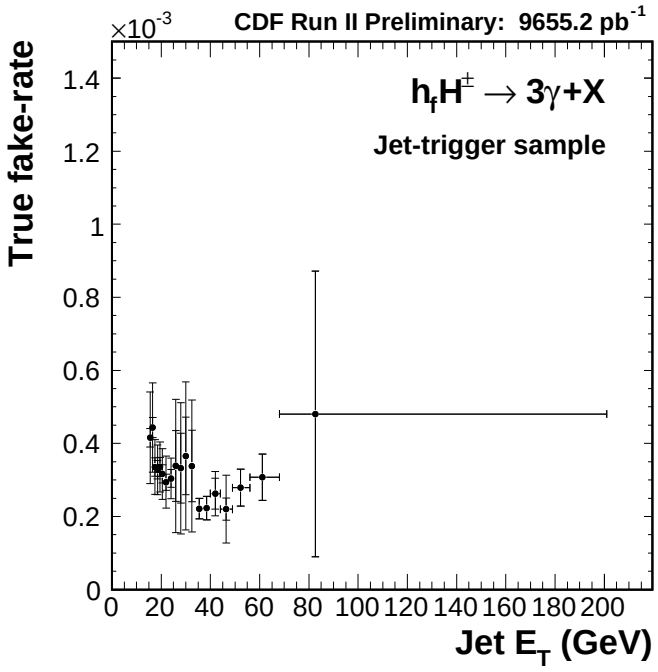

Figure 14: True fake-rates corresponding to the loose denominator cuts ($P'_{\rm true}$) with statistical errors (inner error-bars) and total errors (outer error-bars) for the combined jet datasets (JET20, JET50, JET70, and JET100).

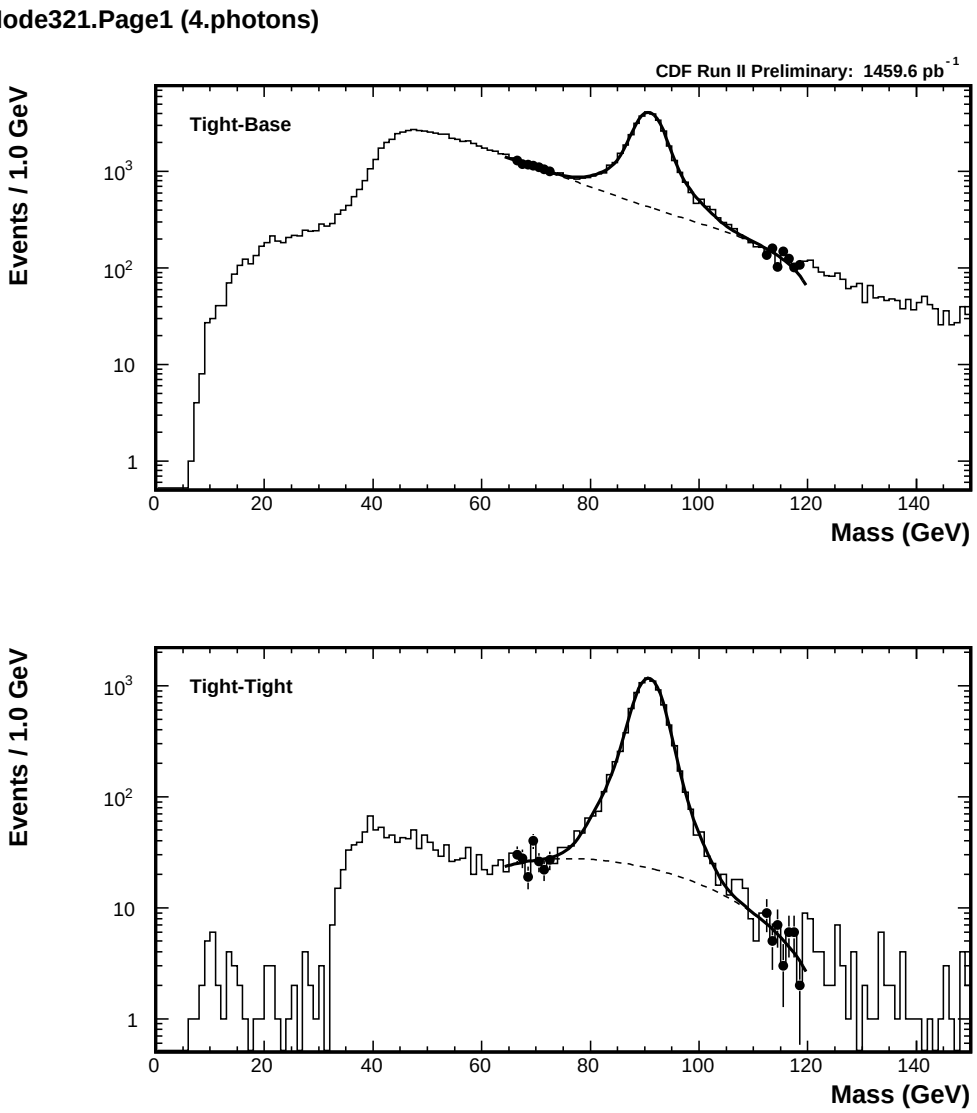

Figure 15: Dielectron invariant-mass distributions for the photon efficiency measurement using the loose denominator cuts. The data correspond to the periods 0–9.

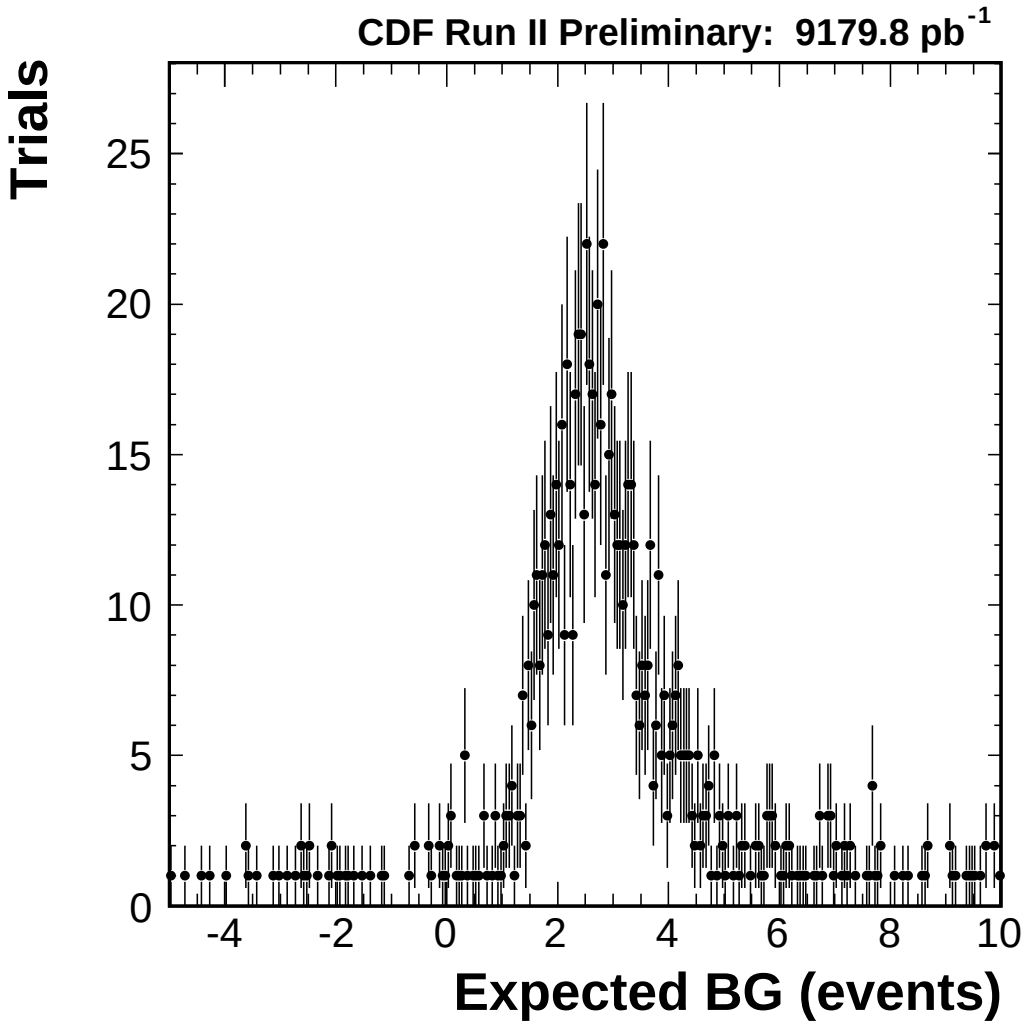

Figure 16: Variation of the estimated number of fake-photon background events in 1000 trials performed to study the effect of the systematic uncertainty originating from the dependence on the quark-gluon composition of the fake rates.

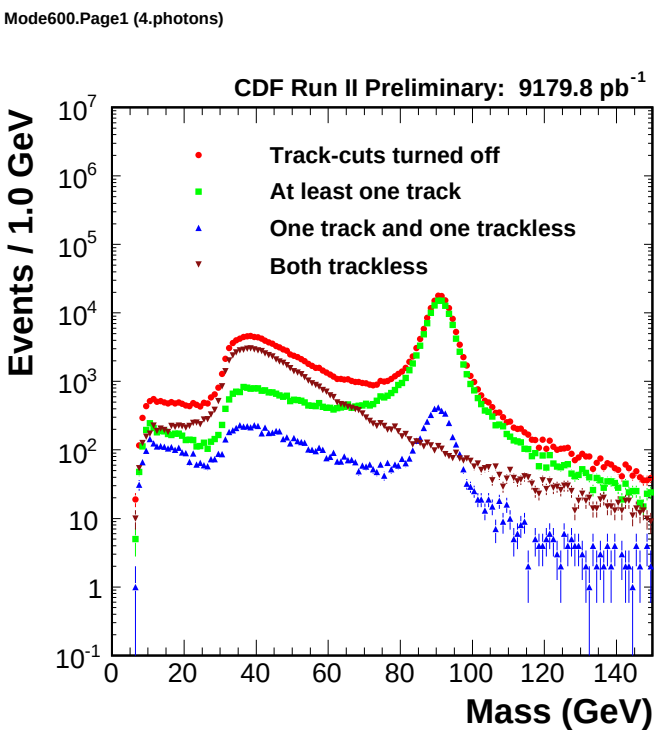

Figure 17: Invariant mass distributions for the events with 2 EM objects.

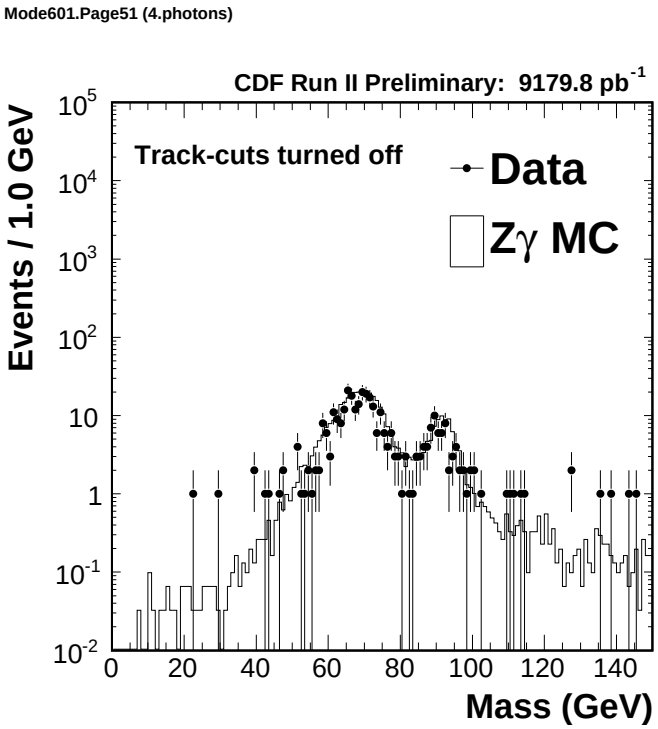

Figure 18: Invariant mass distributions for the events with 3 EM objects.

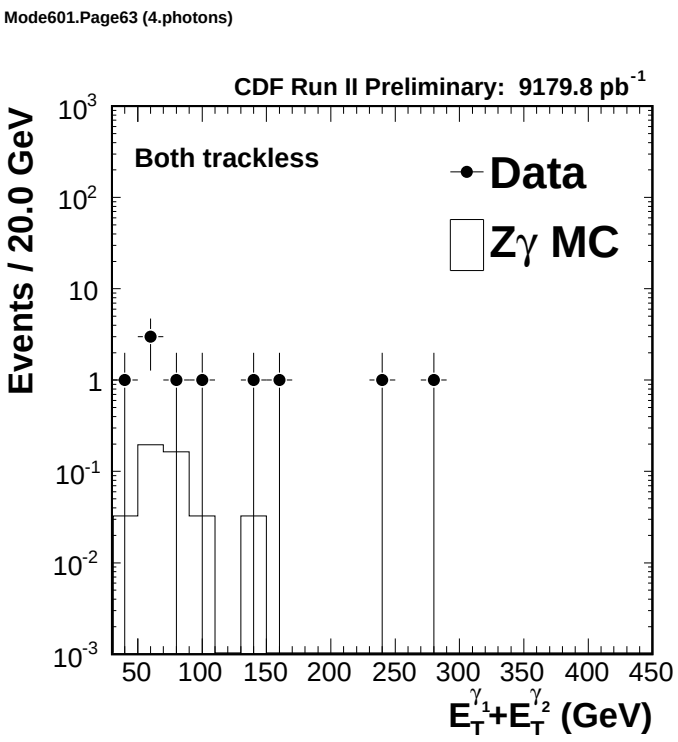

Figure 19: Distributions of $E_T^{\gamma 1} + E_T^{\gamma 2}$ for the real data and $Z(\rightarrow ee)\gamma$ Monte Carlo events.

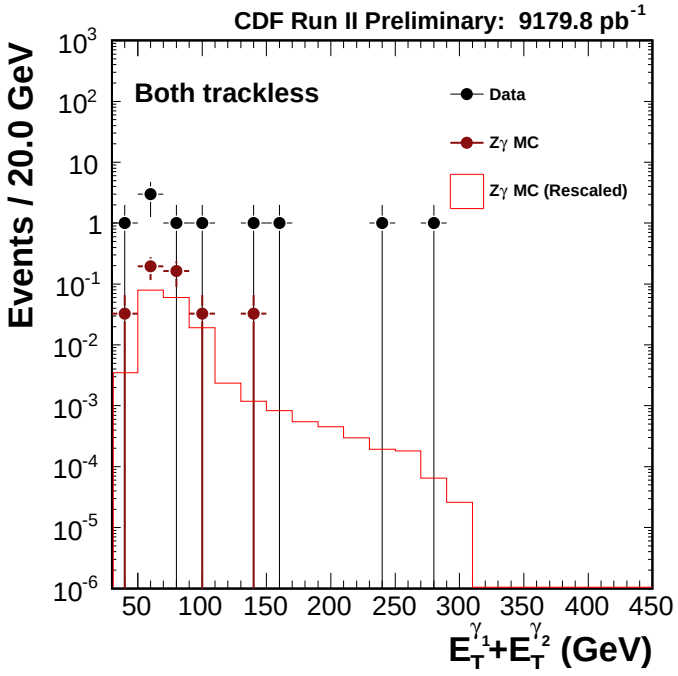

Figure 20: Distributions of $E_T^{\gamma 1} + E_T^{\gamma 2}$ for the real data and $Z(\rightarrow ee)\gamma$ Monte Carlo events.

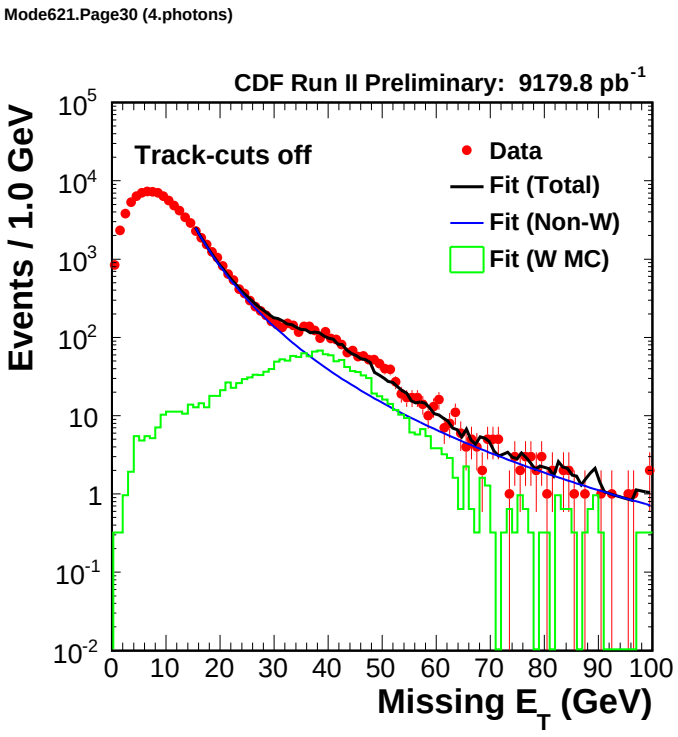

Figure 21: Missing E_T distributions for the real data and $W(\rightarrow e\nu)\gamma$ Monte Carlo events. The real data are fit with the Monte Carlo distribution and an emprical function of the form $p_0 x^{-p_1}$ to model the non-W events.

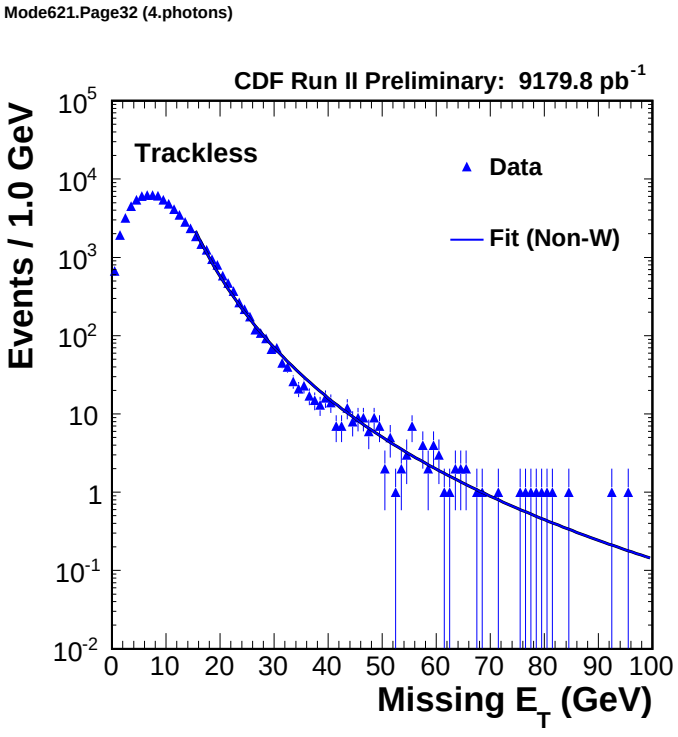

Figure 22: Missing E_T distributions for the real data with 2 EM objects required to have no associated good tracks. We try to fit the data with the non-W function plus the shape of W events based on the Monte Carlo data but the fitting result for the W contribution is zero consistent.

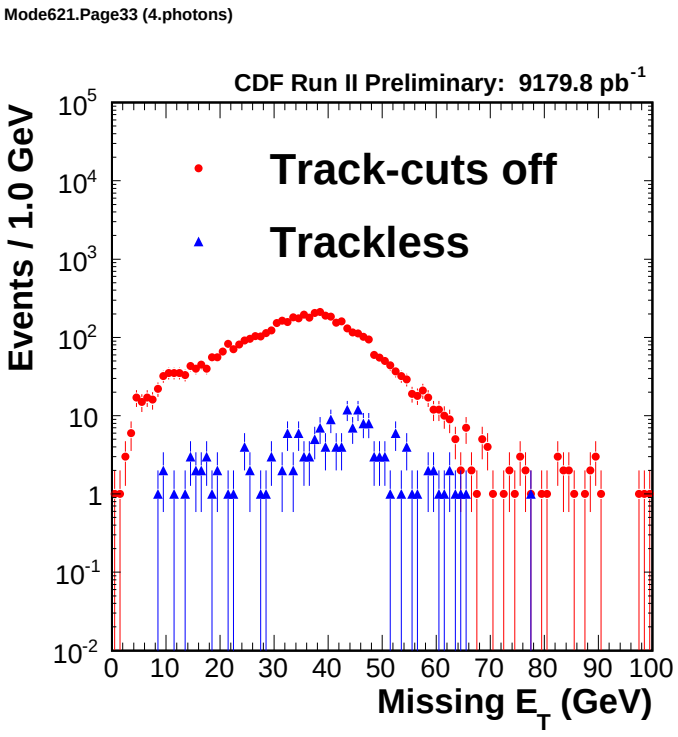

Figure 23: Missing E_T distributions for the $W(\rightarrow e\nu)\gamma$ Monte Carlo data. The 2nd leading EM object is always required to be trackless.

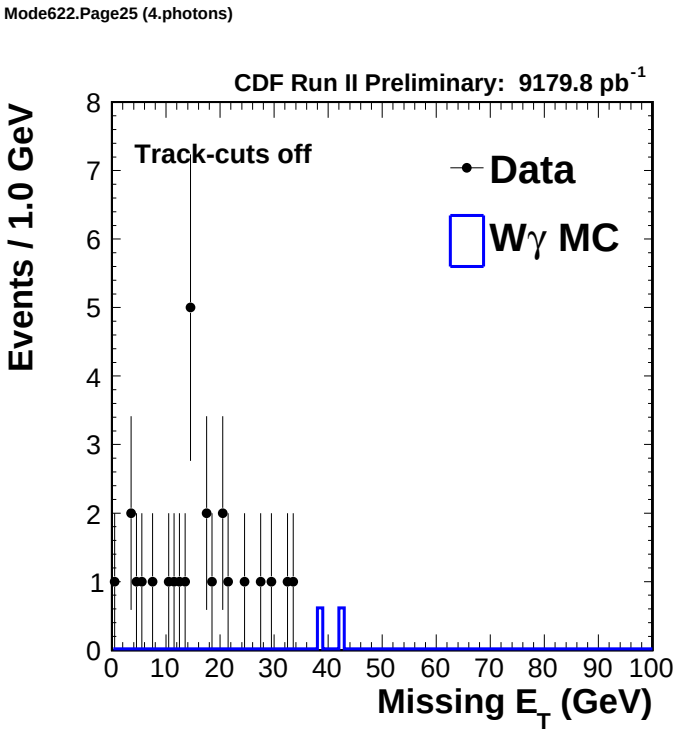

Figure 24: Missing E_T distributions for events with 3 EM objects found in the real data and the $W(\rightarrow e\nu)\gamma$ Monte Carlo data. The track cut is turned off for the leading EM objects, while the 2nd and 3rd EM objects are trackless.

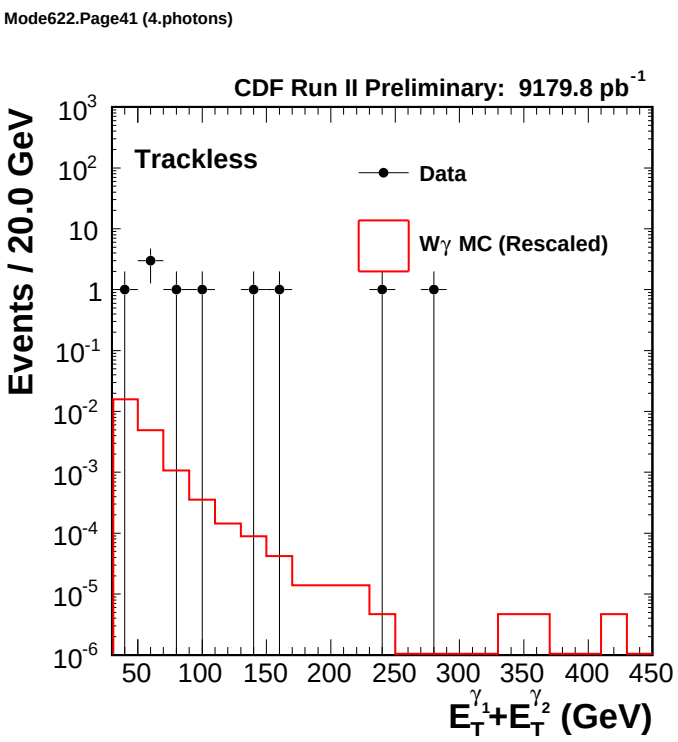

Figure 25: A prediction of $E_T^{\gamma 1} + E_T^{\gamma 2}$ distribution for the $W(\rightarrow e\nu)\gamma$ events.

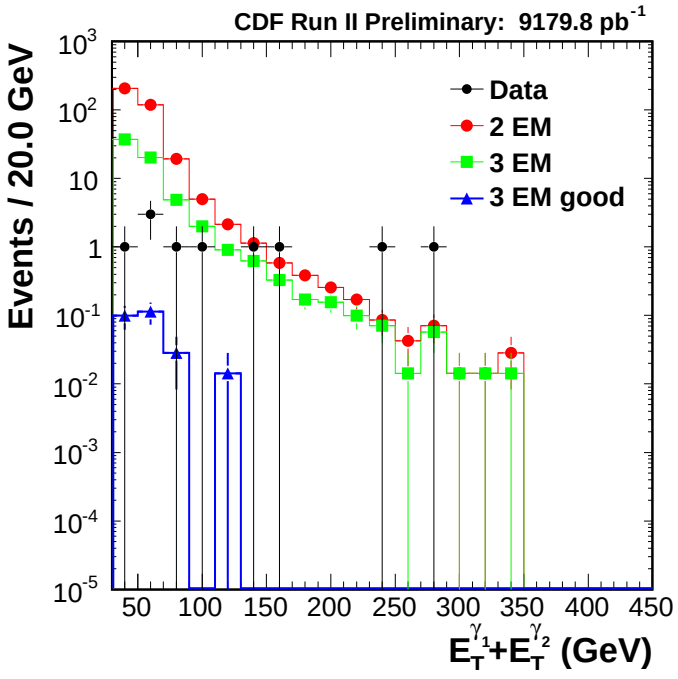

Figure 26: A prediction of $E_T^{\gamma 1} + E_T^{\gamma 2}$ distribution for the $Z(\rightarrow \tau\tau)\gamma$ events.

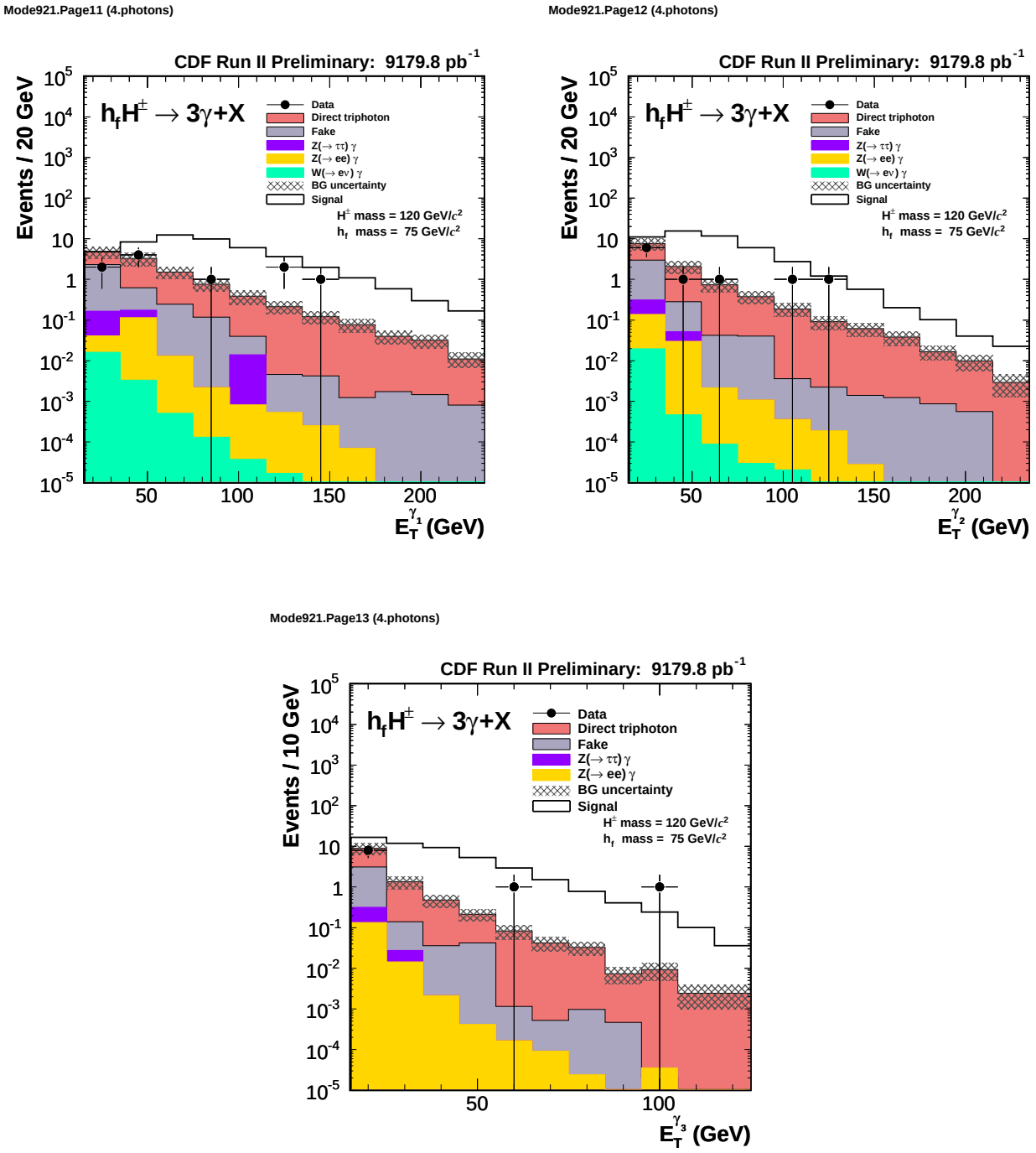

Figure 27: Distributions of each E_T for the $3\gamma + X$ events expected from the SM backgrounds together with the expected signal events for $m_{h_f} = 75$ and $m_{H^\pm} = 120$ GeV.

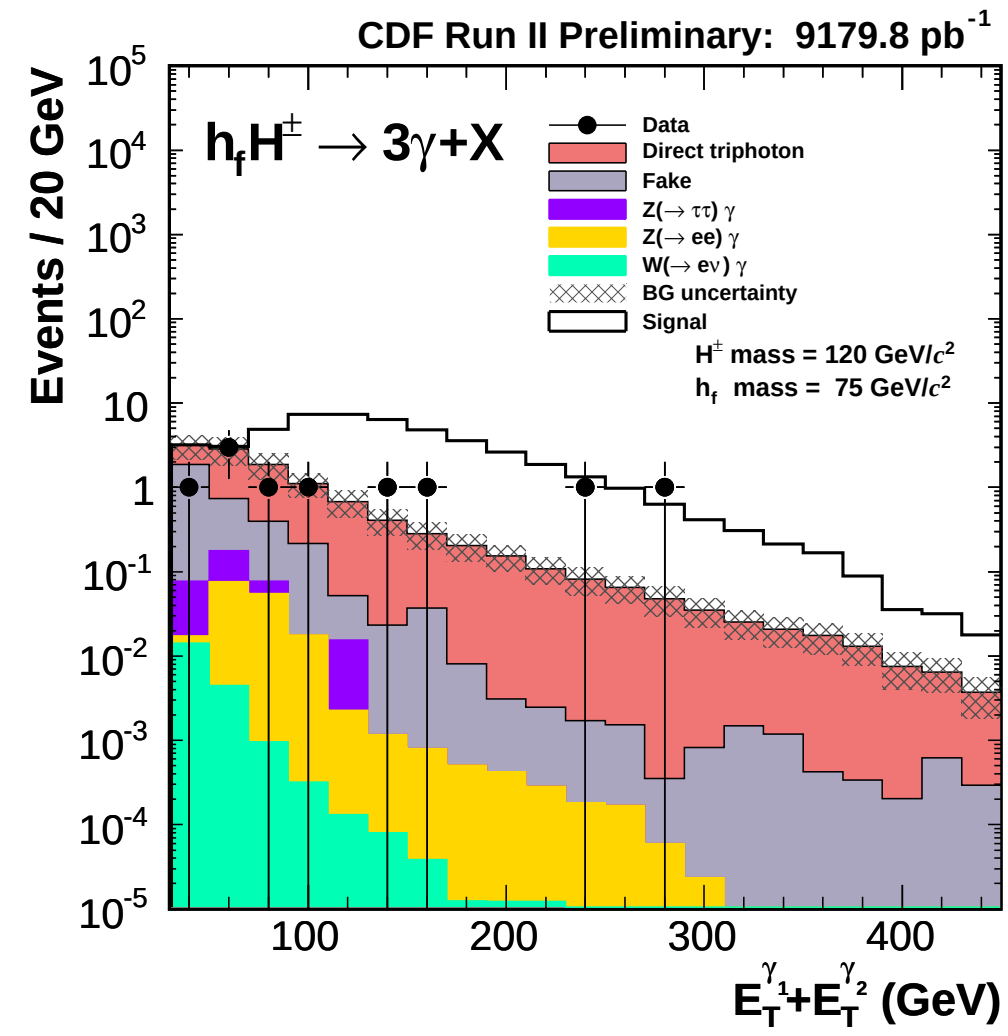

Figure 28: Distribution of $E_T^{\gamma_1} + E_T^{\gamma_2}$ for the $3\gamma + X$ events expected from the SM backgrounds together with the expected signal events for $m_{h_f} = 75$ and $m_{H^\pm} = 120$ GeV.

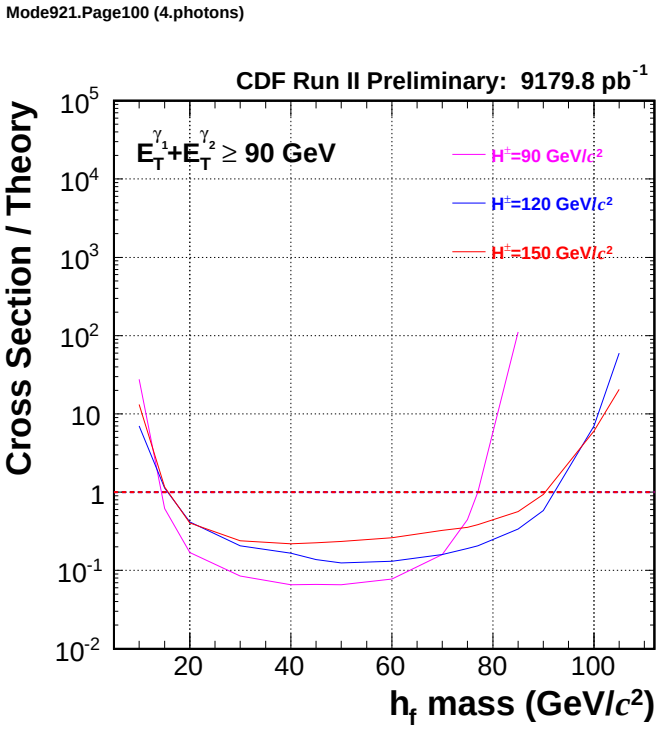

Figure 29: The expected 95% C.L. cross section ratio limit for the case of $E_T^{\gamma 1} + E_T^{\gamma 2} > 90$ GeV (solid lines) and the theoretical cross sections (dashed lines). For $H^{\pm} = 90$ GeV, the excluded region is $m_{h_f} < 76$ GeV.

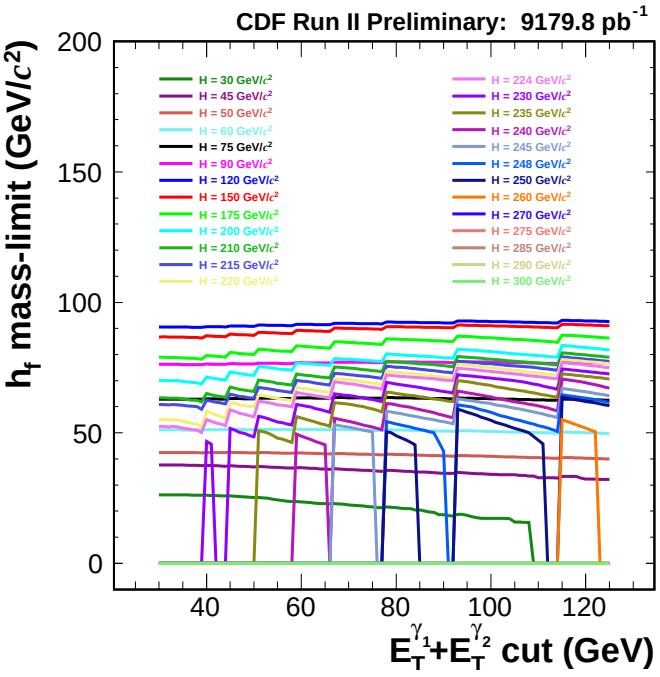

Figure 30: The expected h_f mass-limit as a function of $E_T^{\gamma 1} + E_T^{\gamma 2}$ cut value. The y-axis of this plots are the intersection points between the expected 95% C.L. cross section limit and theoretical cross section. That is the excluded region of the h_f mass as described in Fig. 29. We choose $E_T^{\gamma 1} + E_T^{\gamma 2} > 90$ GeV as this reasonably maximizes and stabilizes the mass limit.

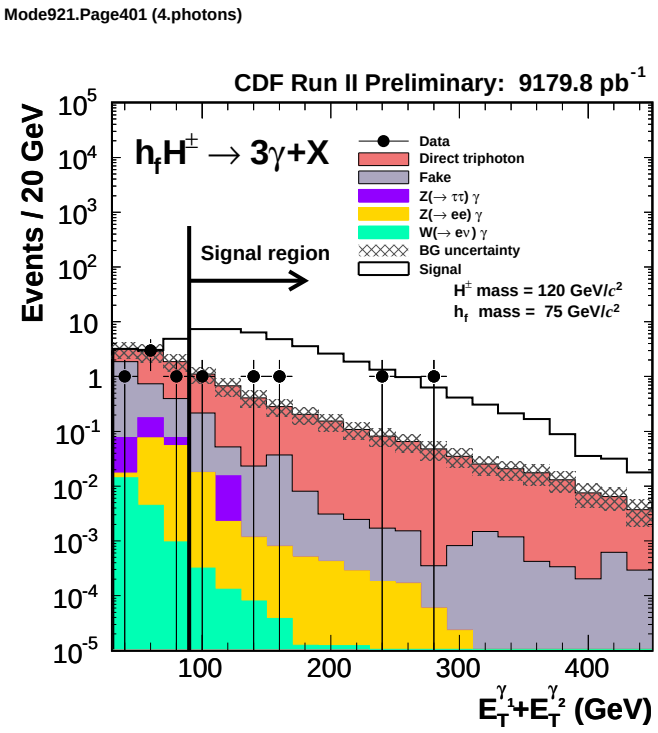

Figure 31: Distribution of $E_T^{\gamma 1} + E_T^{\gamma 2}$ for the $3\gamma + X$ events expected from the SM backgrounds together with the expected signal events for $m_{h_f} = 75$ and $m_{H^\pm} = 120$ GeV.

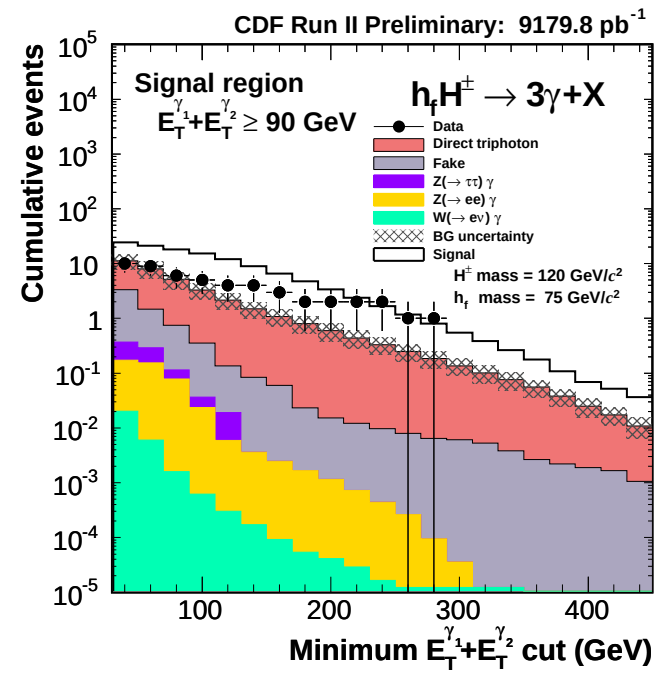

Figure 32: Cumulative distribution of $E_T^{\gamma 1} + E_T^{\gamma 2}$ for the $3\gamma + X$ events expected from the SM backgrounds together with the expected signal events for $m_{h_f} = 75$ and $m_{H^\pm} = 120$ GeV.

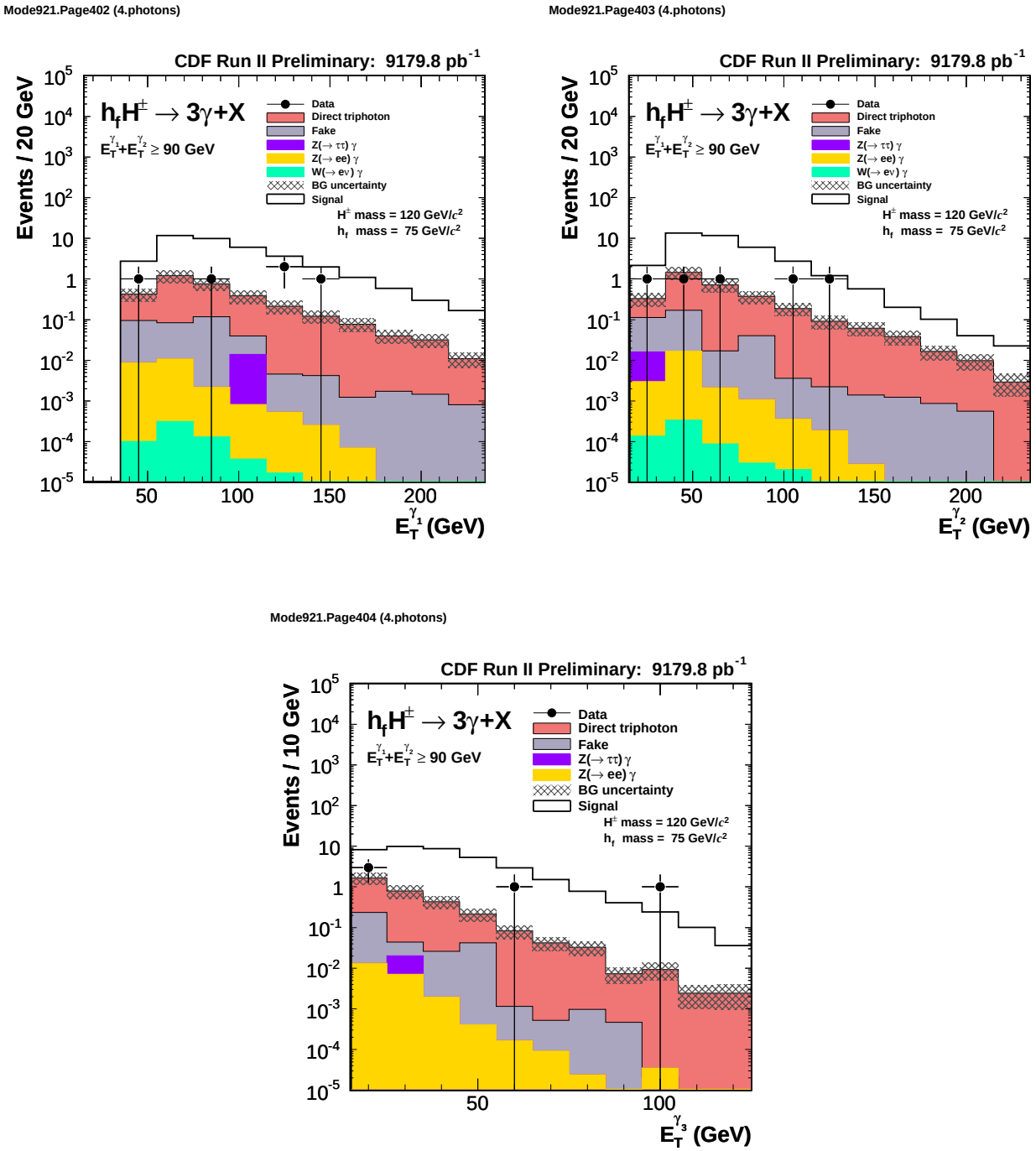

Figure 33: Distributions of each E_T for the $3\gamma + X$ events with $E_T^{\gamma 1} + E_T^{\gamma 2} > 90$ GeV expected from the SM backgrounds and expected signal events for $m_{h_f} = 75$ and $m_{H^\pm} = 120$ GeV.

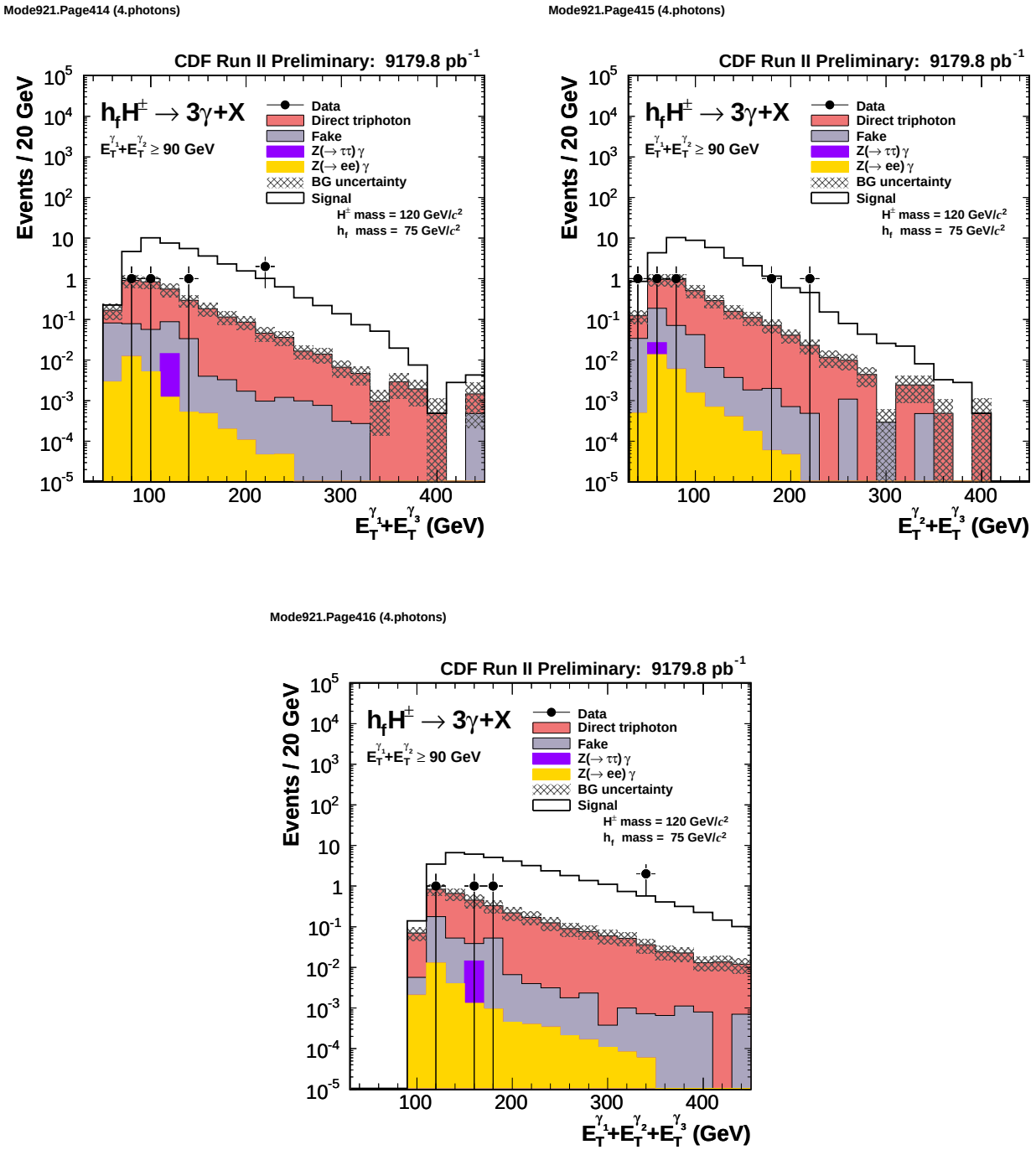

Figure 34: Distributions of various sum of E_T for the $3\gamma + X$ events with $E_T^{\gamma 1} + E_T^{\gamma 2} > 90$ GeV expected from the SM backgrounds and expected signal events for $m_{h_f} = 75$ and $m_{H^\pm} = 120$ GeV.

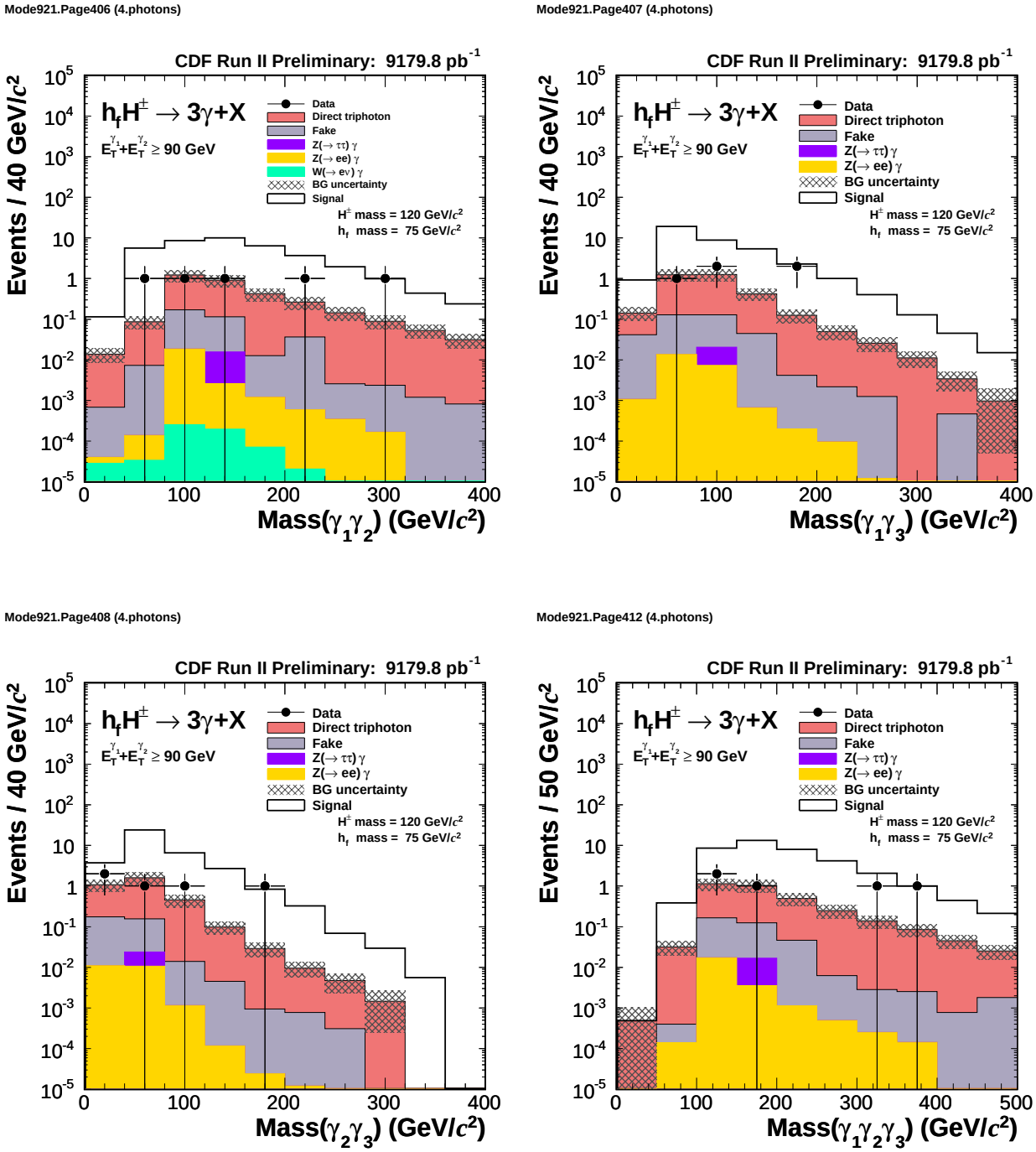

Figure 35: Distributions of invariant mass of each pair of photons (the top two plots and bottom left plot) and three photons (the bottom right plot) for the $3\gamma + X$ events with $E_T^{\gamma 1} + E_T^{\gamma 2} > 90$ GeV expected from the SM backgrounds and expected signal events for $m_{h_f} = 75$ and $m_{H^\pm} = 120$ GeV.

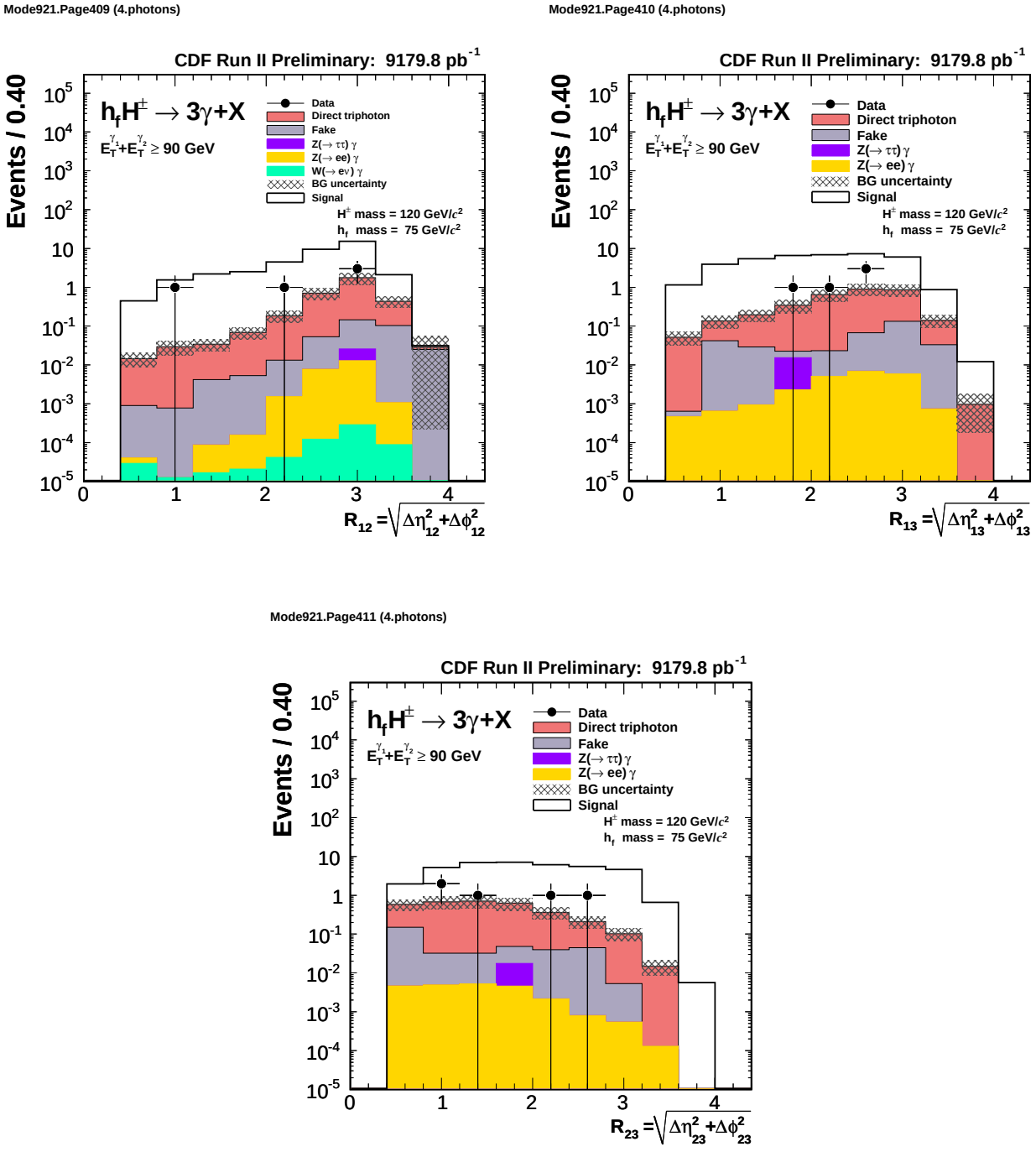

Figure 36: Distributions of R (the distance in the η-ϕ plane between each pair of photons for the $3\gamma + X$ events with $E_T^{\gamma 1} + E_T^{\gamma 2} > 90$ GeV expected from the SM backgrounds and expected signal events for $m_{h_f} = 75$ and $m_{H^\pm} = 120$ GeV.

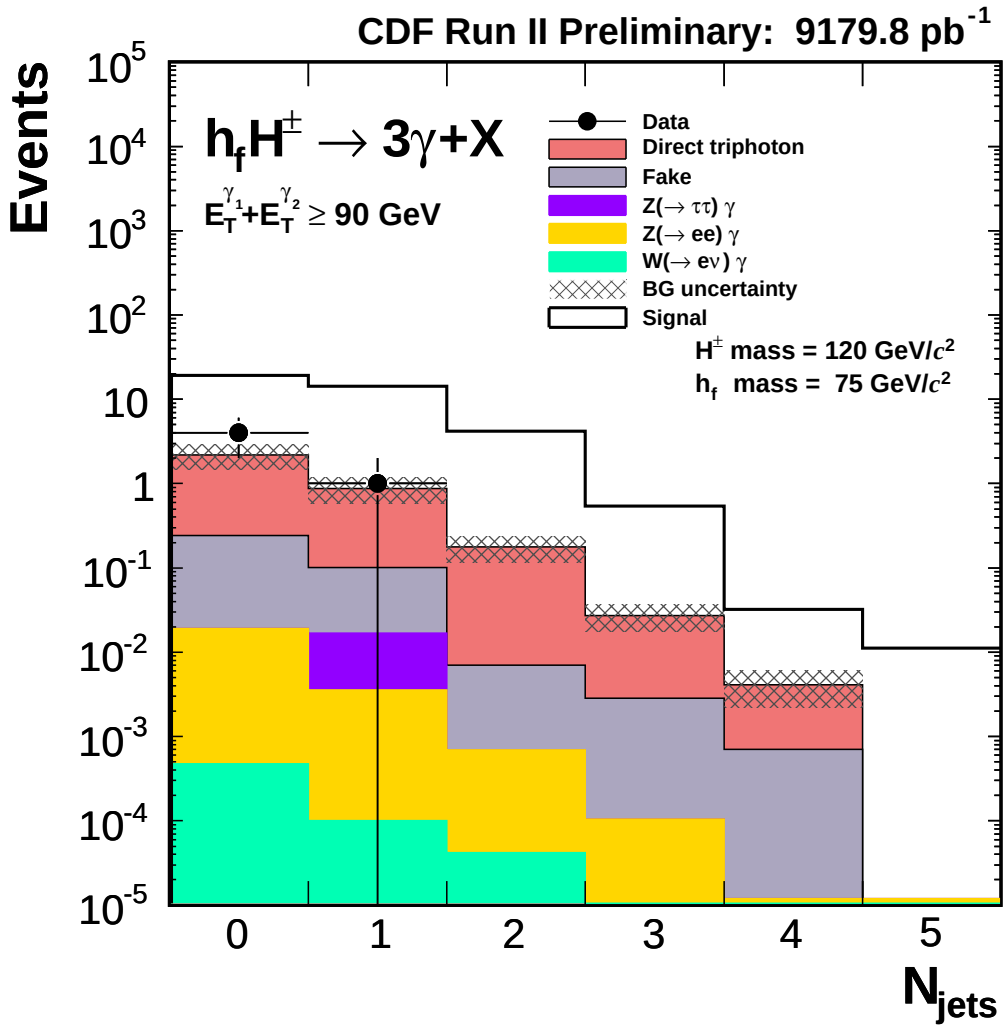

Figure 37: The number of jets in the central region with $E_T > 10$ GeV for the $3\gamma + X$ events with $E_T^{\gamma_1} + E_T^{\gamma_2} > 90$ GeV expected from the SM backgrounds and expected signal events for $m_{h_f} = 75$ and $m_{H^\pm} = 120$ GeV.

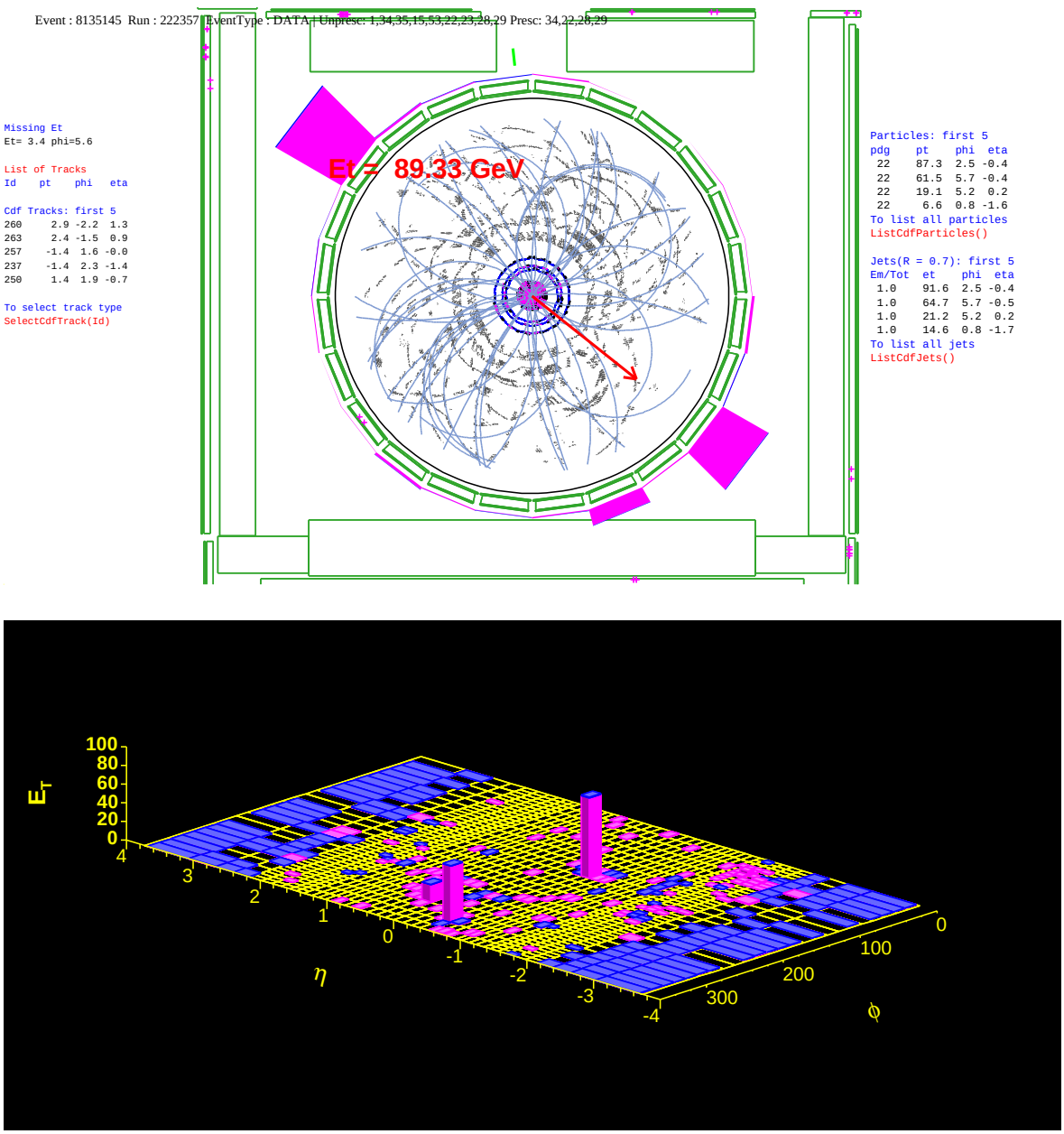

Figure 38: Event display of a candidate event.

Run = 222357, Event = 8135145		
1st (E_T, η, ϕ)	=	$(82\ \text{GeV}, -0.56, 2.53)$
2nd (E_T, η, ϕ)	=	$(56\ \text{GeV}, -0.60, 5.69)$
3rd (E_T, η, ϕ)	=	$(19\ \text{GeV}, +0.06, 5.22)$
Corrected $\not\!\!E_T$	=	14 GeV
$\phi(\not\!\!E_T)$	=	2.63
(M_{12}, M_{23}, M_{31})	=	$(136, 27, 81)$ GeV
Extra jet $(E_T > 10\ \text{GeV})$ (E_T, η, ϕ)	=	$(12\ \text{GeV}, -1.80, 0.78)$

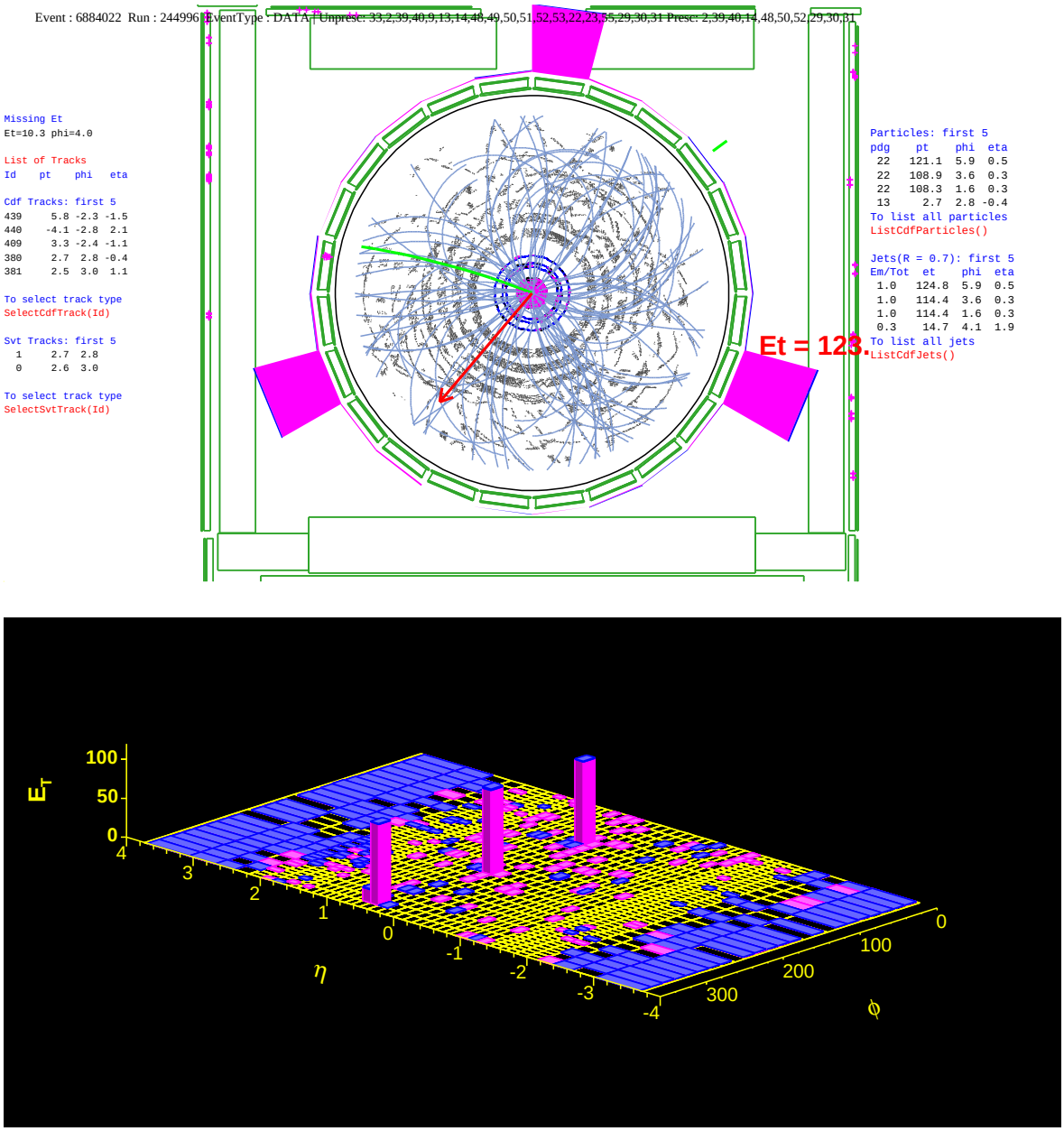

Figure 39: Event display of a candidate event.

Run = 244996, Event = 6884022		
1st (E_T, η, ϕ)	=	$(117\ \text{GeV}, +0.58, 5.87)$
2nd (E_T, η, ϕ)	=	$(106\ \text{GeV}, +0.40, 3.56)$
3rd (E_T, η, ϕ)	=	$(100\ \text{GeV}, +0.44, 1.53)$
Corrected $\not\!\!E_T$	=	18 GeV
$\phi(\not\!\!E_T)$	=	5.12
(M_{12}, M_{23}, M_{31})	=	$(214, 181, 187)$ GeV

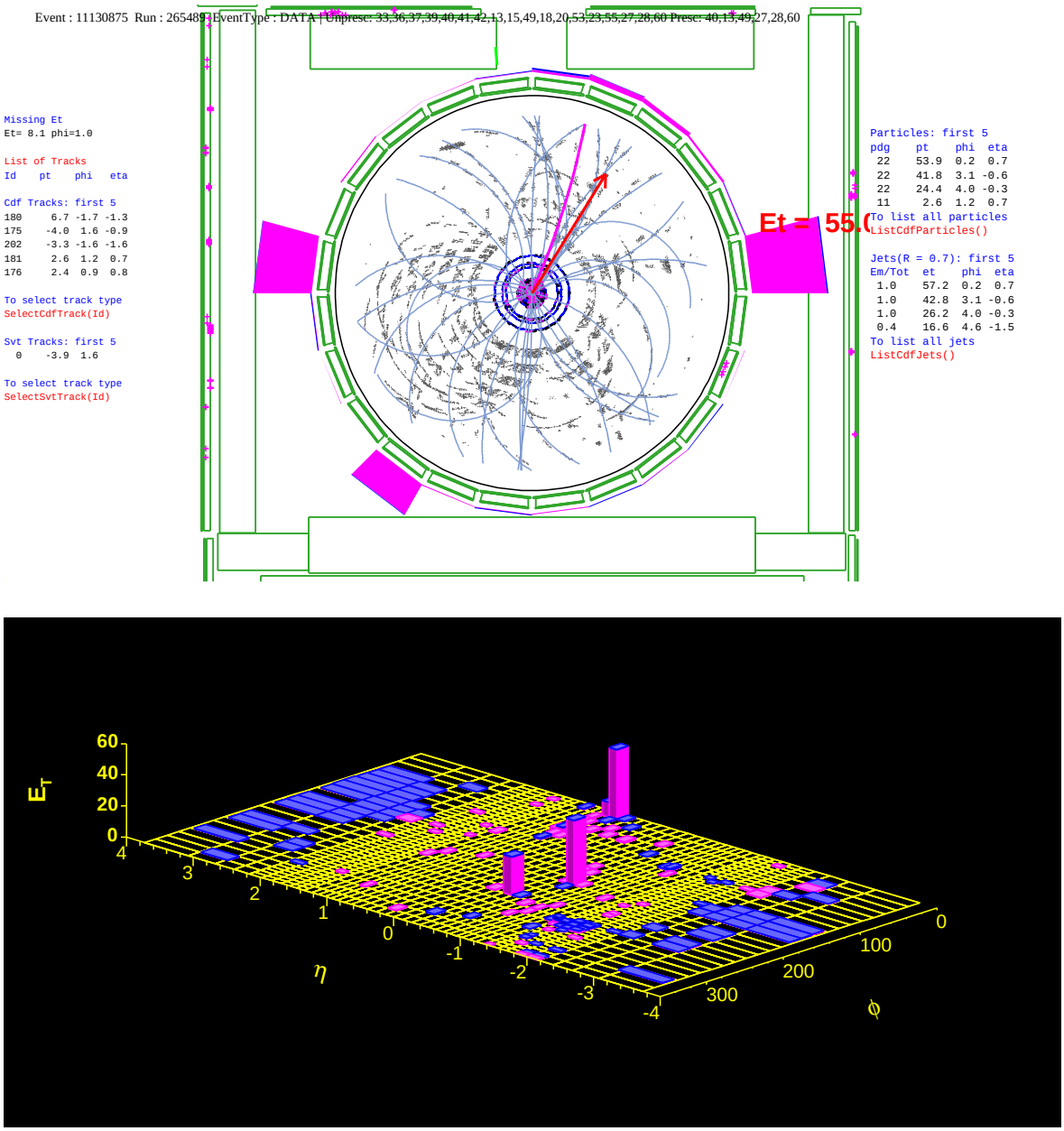

Figure 40: Event display of a candidate event.

Run = 265489, Event = 11130875		
1st (E_T, η, ϕ)	=	$(54\ \text{GeV}, +0.68, 0.19)$
2nd (E_T, η, ϕ)	=	$(40\ \text{GeV}, -0.59, 3.08)$
3rd (E_T, η, ϕ)	=	$(24\ \text{GeV}, -0.36, 4.02)$
Corrected $\not\!\!E_T$	=	24 GeV
$\phi(\not\!\!E_T)$	=	0.70
(M_{12}, M_{23}, M_{31})	=	$(112, 29, 79)$ GeV
Extra jet $(E_T > 10\ \text{GeV})$ (E_T, η, ϕ)	=	$(15\ \text{GeV}, -1.55, 4.63)$

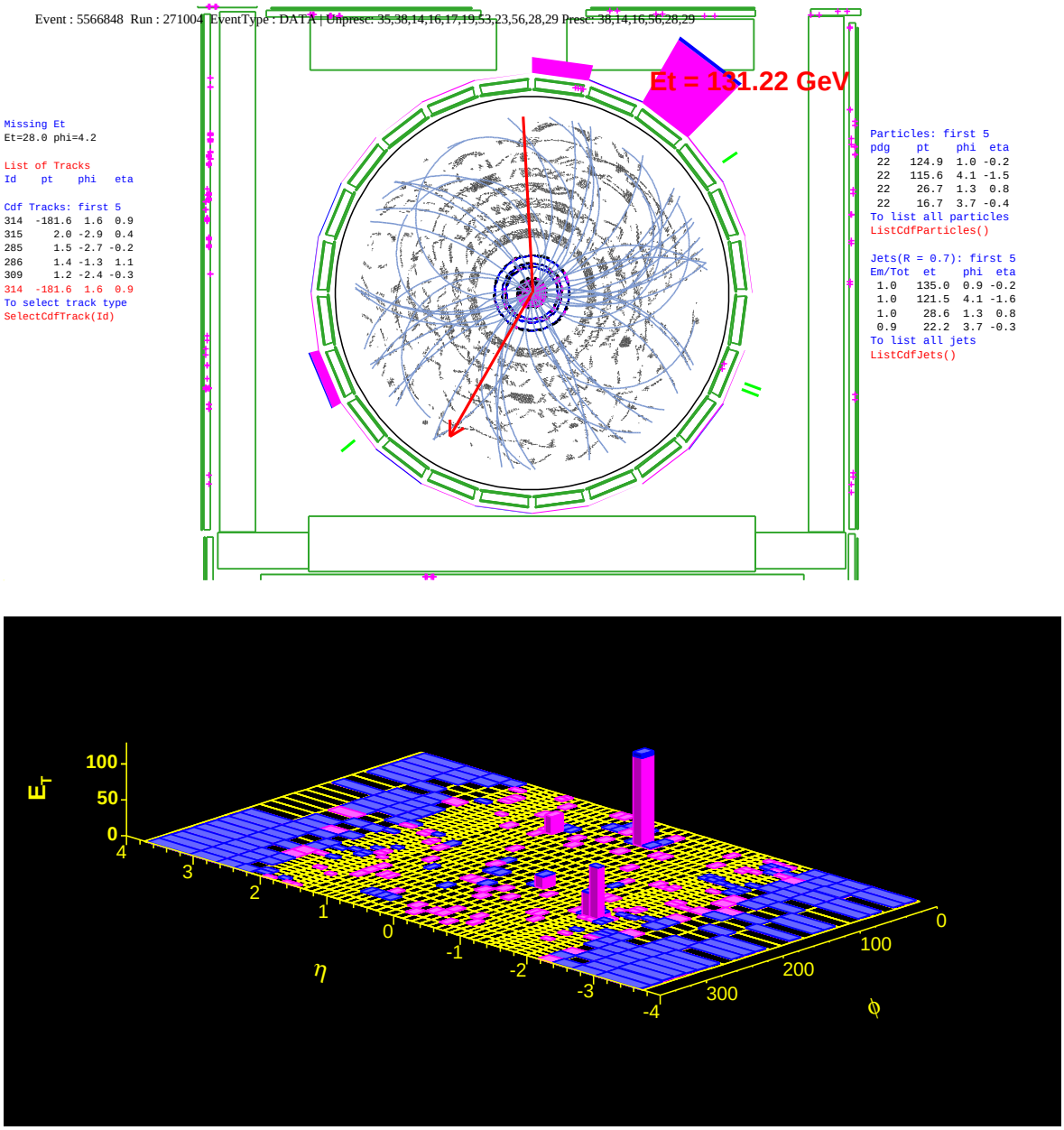

Figure 41: Event display of a candidate event.

Run = 271004, Event = 5566848		
1st (E_T, η, ϕ)	=	$(129 \text{ GeV}, -0.09, 0.94)$
2nd (E_T, η, ϕ)	=	$(24 \text{ GeV}, +0.91, 1.33)$
3rd (E_T, η, ϕ)	=	$(17 \text{ GeV}, -0.28, 3.62)$
Corrected $\not\!\!E_T$	=	20 GeV
$\phi(\not\!\!E_T)$	=	4.48
(M_{12}, M_{23}, M_{31})	=	$(63, 45, 91)$ GeV
Plug EM (E_T, η, ϕ)	=	$(136 \text{ GeV}, -1.40, 4.08)$
(M_{14}, M_{24}, M_{34})	=	$(265, 64, 121)$ GeV
Low quality track (p_T, η, ϕ)	=	$(181 \text{ GeV}/c, +0.94, 1.63)$
Low quality track		29 COT hits (13 axial, 16 stereo), 3 segments.

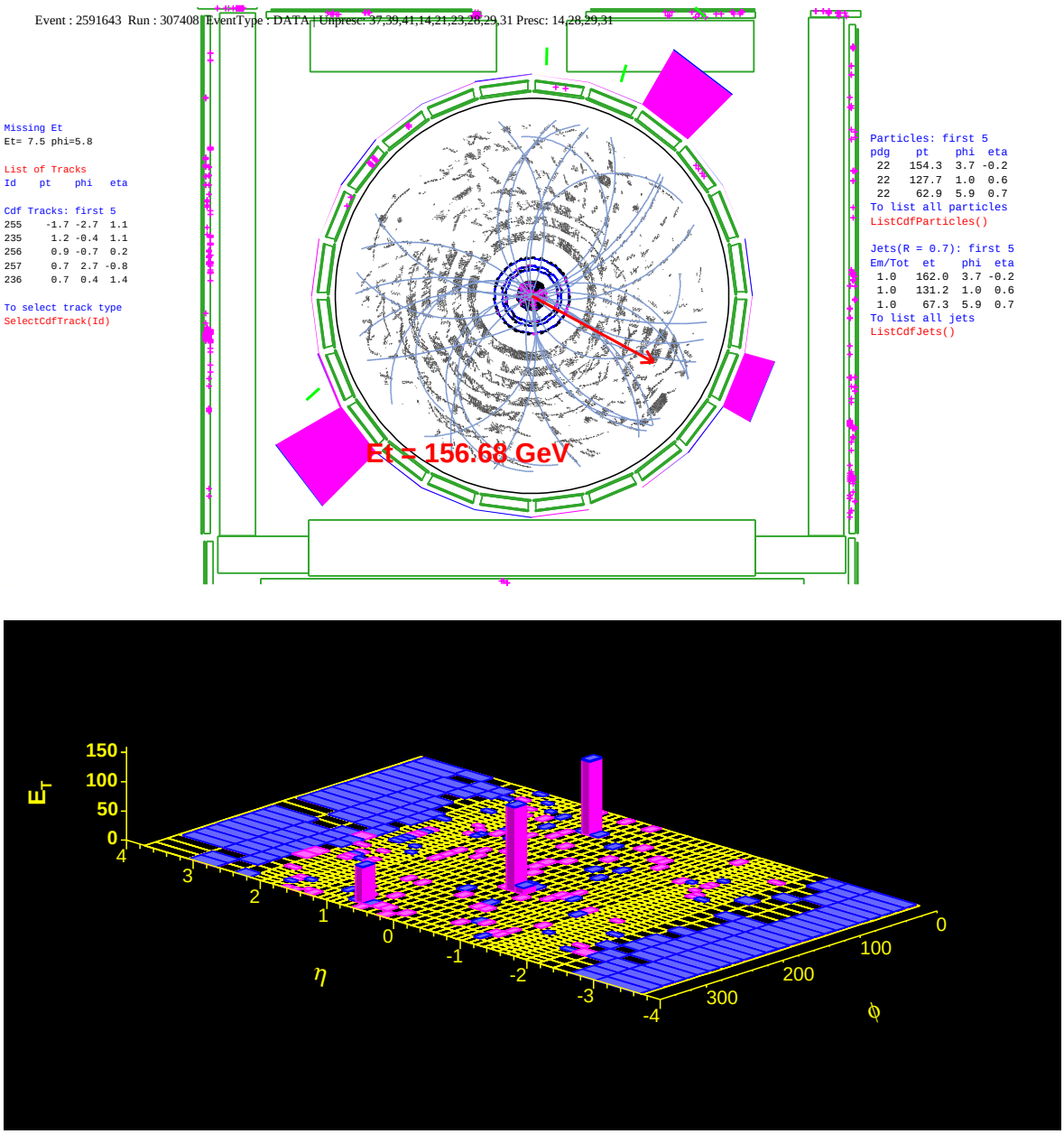

Figure 42: Event display of a candidate event.

Run = 307408, Event = 2591643		
1st (E_T, η, ϕ)	=	$(152\ \text{GeV}, -0.24, 3.69)$
2nd (E_T, η, ϕ)	=	$(128\ \text{GeV}, +0.56, 0.94)$
3rd (E_T, η, ϕ)	=	$(63\ \text{GeV}, +0.69, 5.88)$
Corrected $\not\!\!E_T$	=	27 GeV
$\phi(\not\!\!E_T)$	=	3.77
(M_{12}, M_{23}, M_{31})	=	$(293, 108, 195)$ GeV

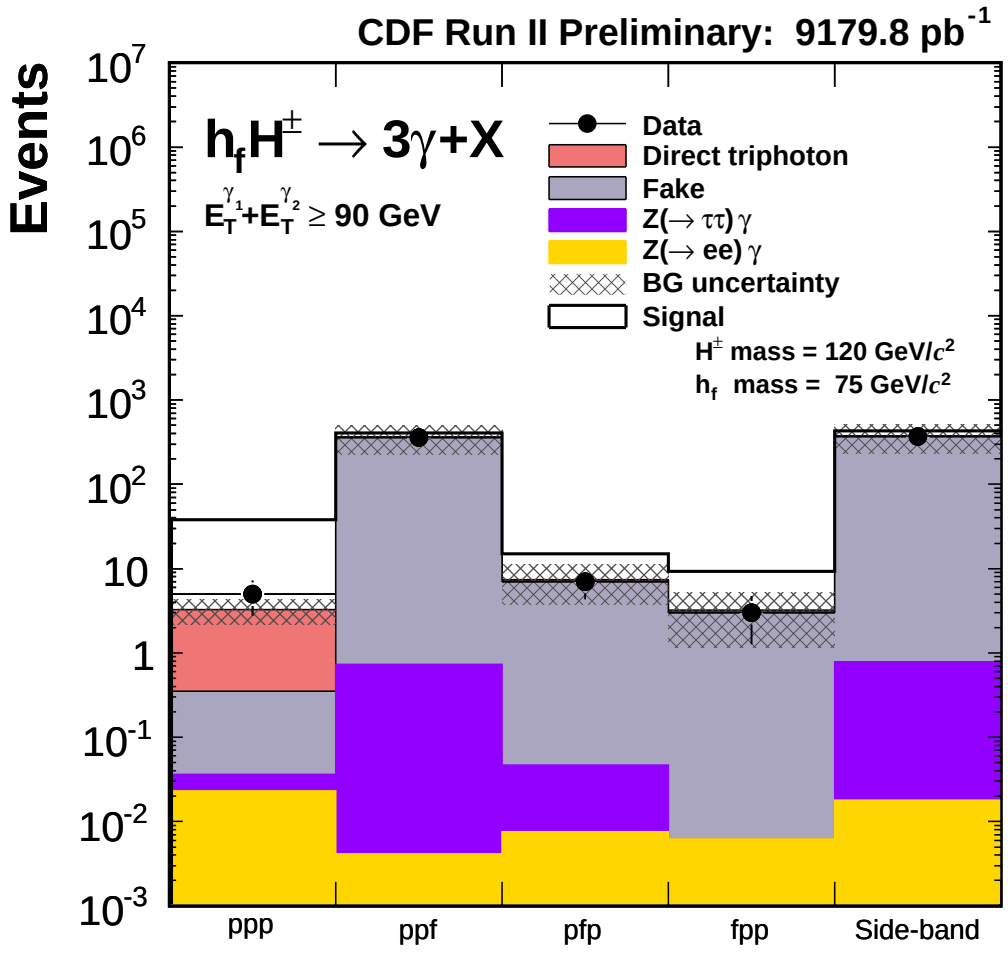

Figure 43: The expected and observed number of events for the 3γ good events (ppp), for each of the pilot component (ppf etc.), and the total of the pilot components. The expected Higgs contributions are also included.

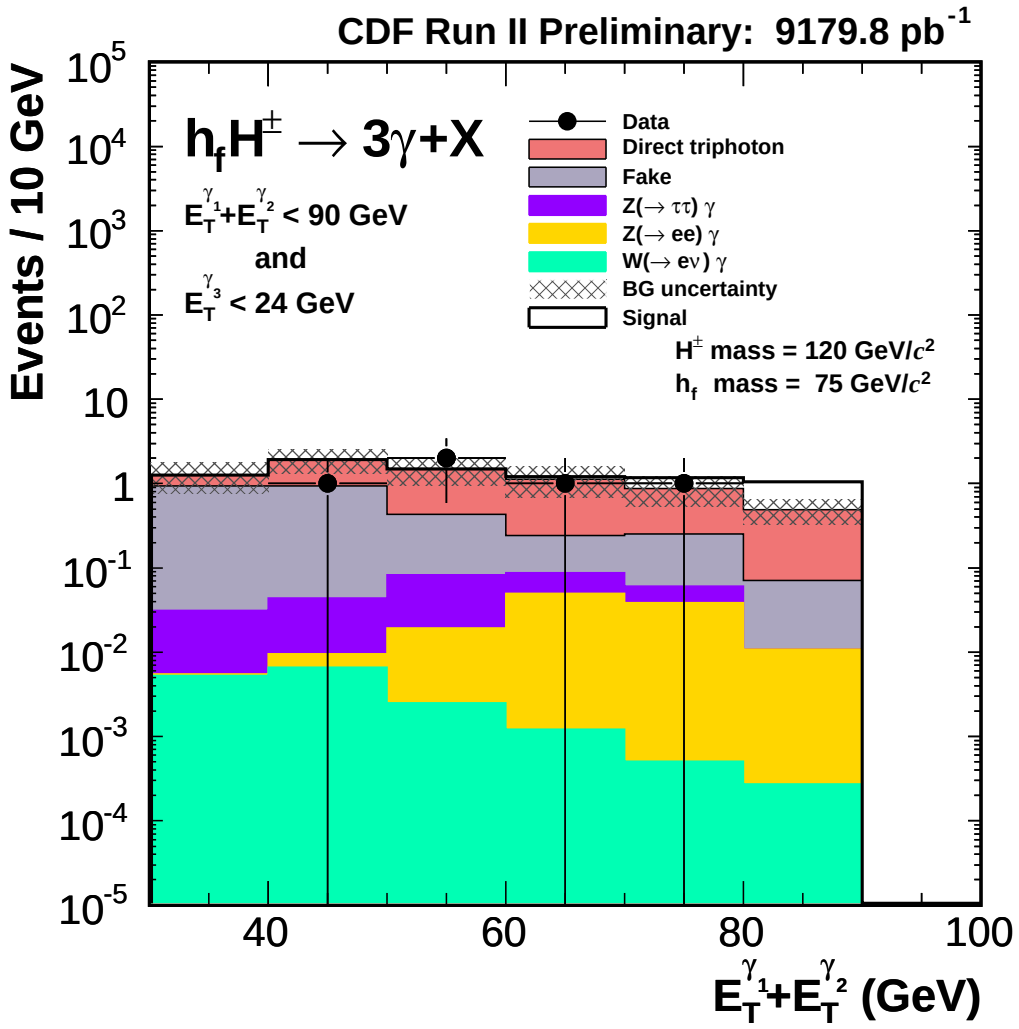

Figure 44: Distribution of $E_T^{\gamma 1} + E_T^{\gamma 2}$ for the $3\gamma + X$ events with $E_T^{\gamma 1} + E_T^{\gamma 2} < 90$ GeV and $E_T^{\gamma 3} < 24$ GeV, expected from the SM backgrounds and expected signal events for $m_{h_f} = 75$ and $m_{H^\pm} = 120$ GeV.

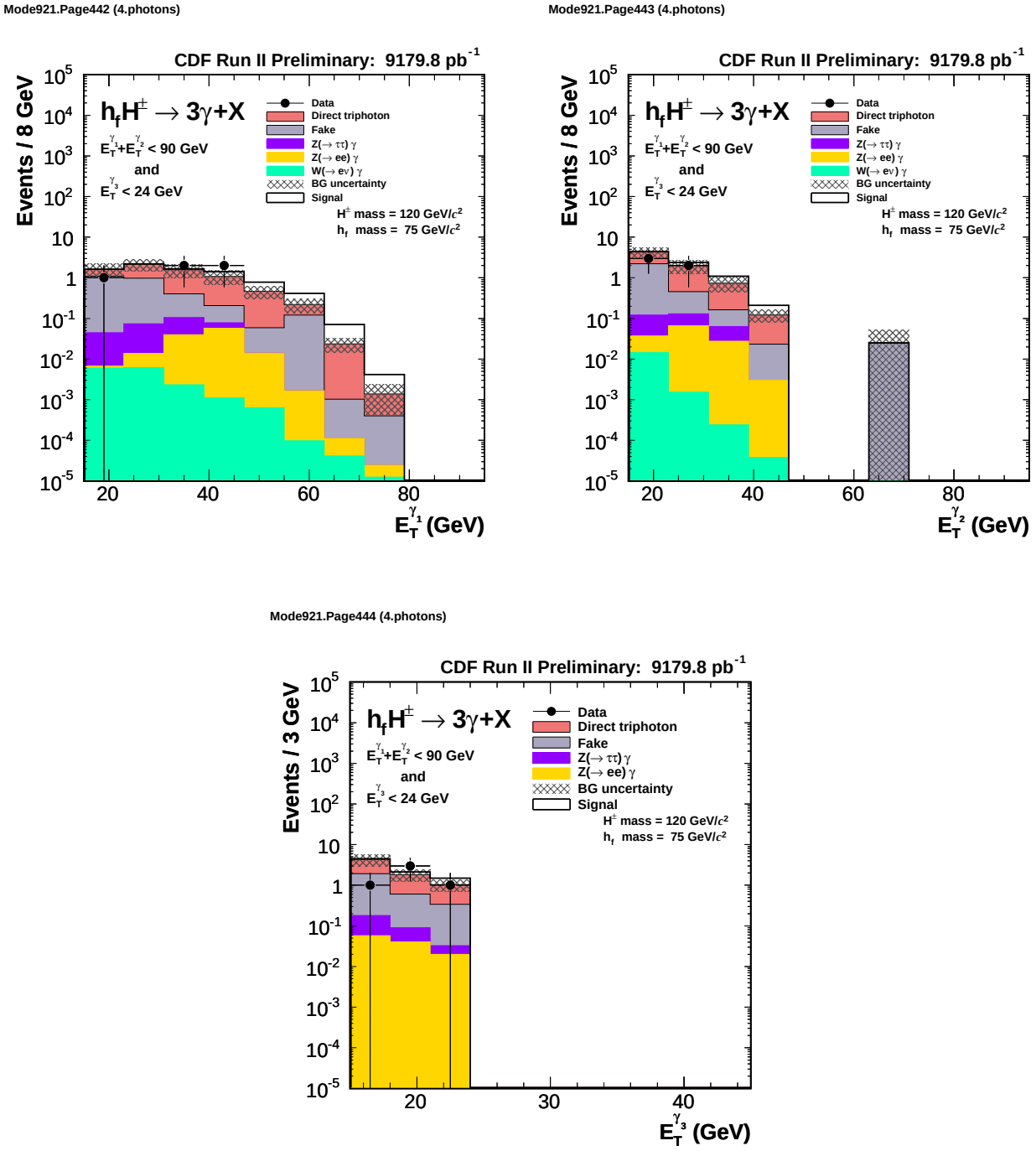

Figure 45: Distributions of each E_T for the $3\gamma + X$ events with $E_T^{\gamma 1} + E_T^{\gamma 2} < 90$ GeV and $E_T^{\gamma 3} < 24$ GeV, expected from the SM backgrounds and expected signal events for $m_{h_f} = 75$ and $m_{H^\pm} = 120$ GeV.

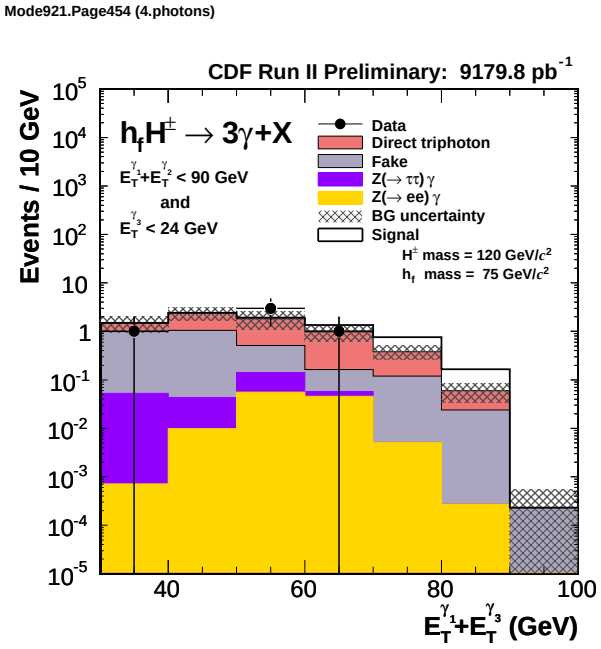

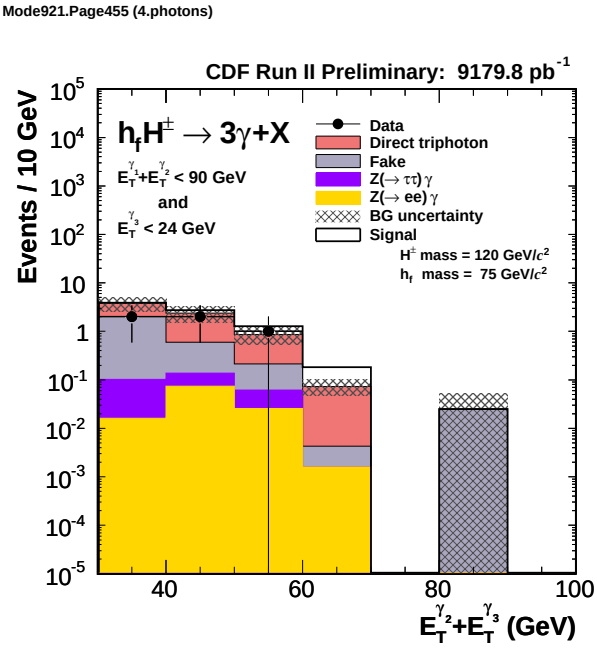

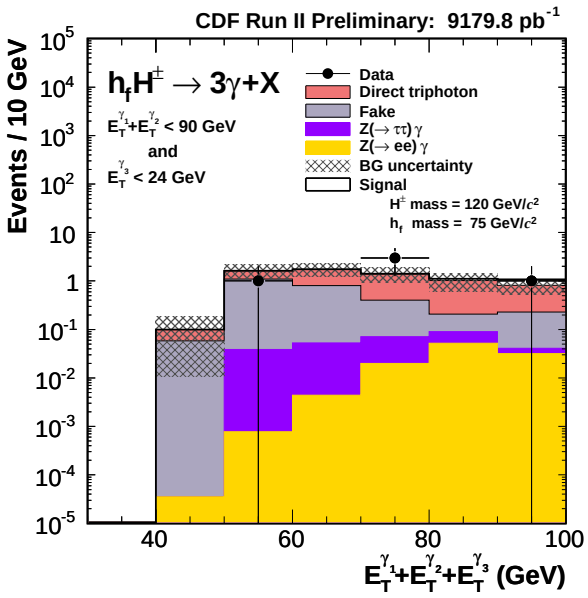

Figure 46: Distributions of various sum of E_T for the $3\gamma + X$ events with $E_T^{\gamma 1} + E_T^{\gamma 2} < 90$ GeV and $E_T^{\gamma 3} < 24$ GeV, expected from the SM backgrounds and expected signal events for $m_{h_f} = 75$ and $m_{H^{\pm}} = 120$ GeV.

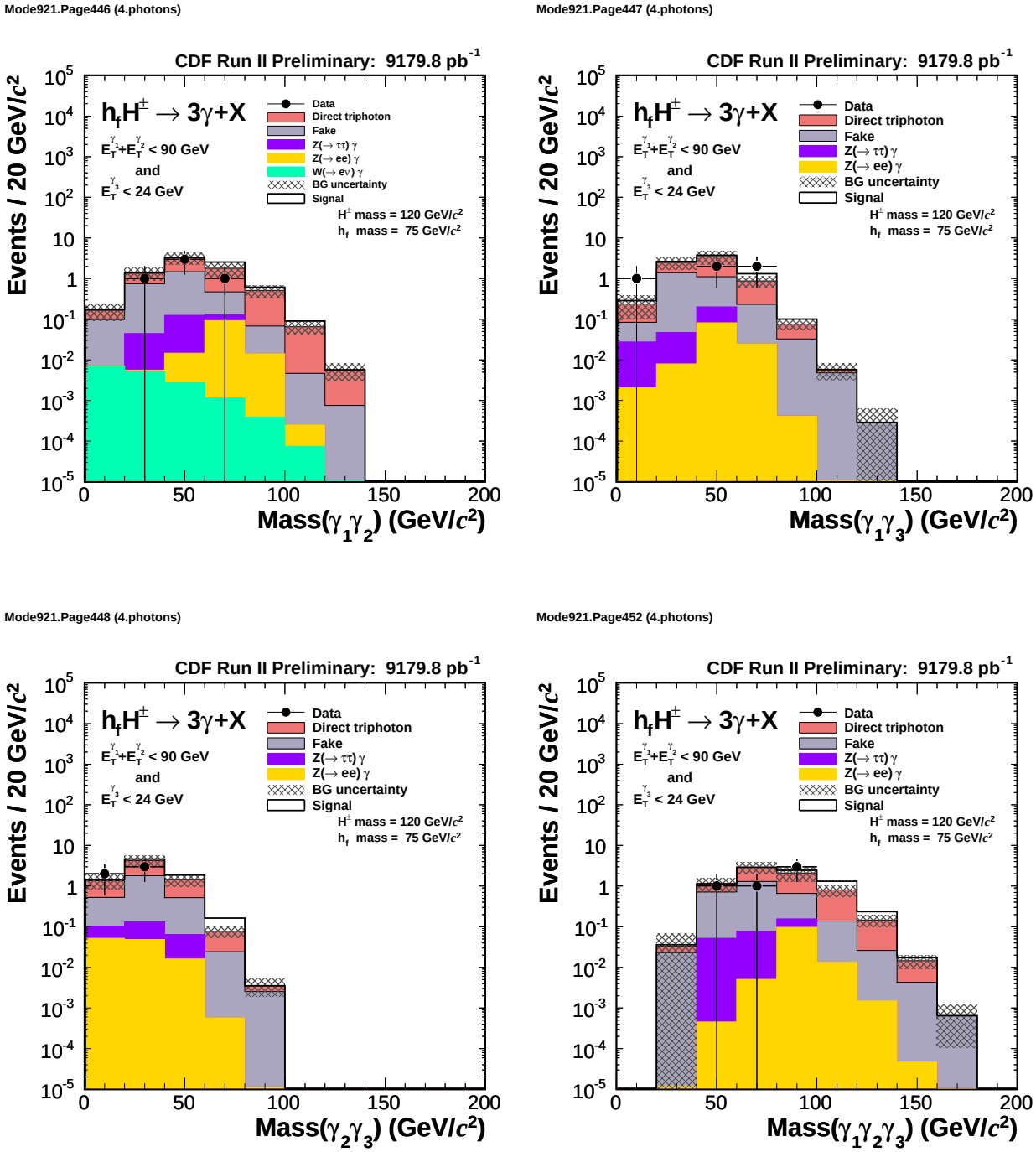

Figure 47: Distributions of invariant mass of each pair of photons (the top two plots and bottom left plot) and three photons (the bottom right plot) for the $3\gamma + X$ events with $E_T^{\gamma 1} + E_T^{\gamma 2} < 90$ GeV and $E_T^{\gamma 3} < 24$ GeV, expected from the SM backgrounds and expected signal events for $m_{h_f} = 75$ and $m_{H^\pm} = 120$ GeV.

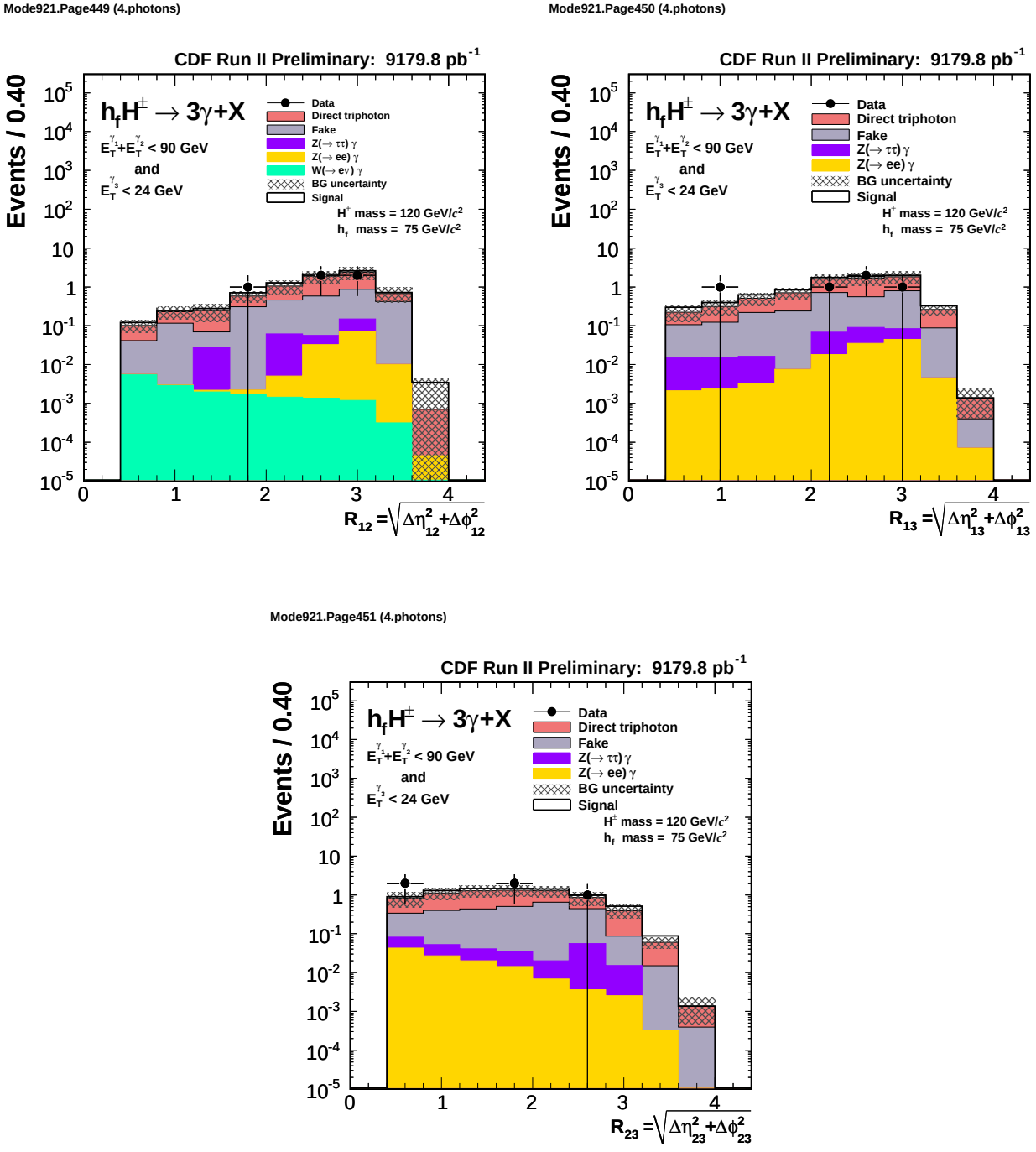

Figure 48: Distributions of R (the distance in the η-ϕ plane between each pair of photons for the $3\gamma + X$ events with $E_T^{\gamma 1} + E_T^{\gamma 2} < 90$ GeV and $E_T^{\gamma 3} < 24$ GeV, expected from the SM backgrounds and expected signal events for $m_{h_f} = 75$ and $m_{H^\pm} = 120$ GeV.

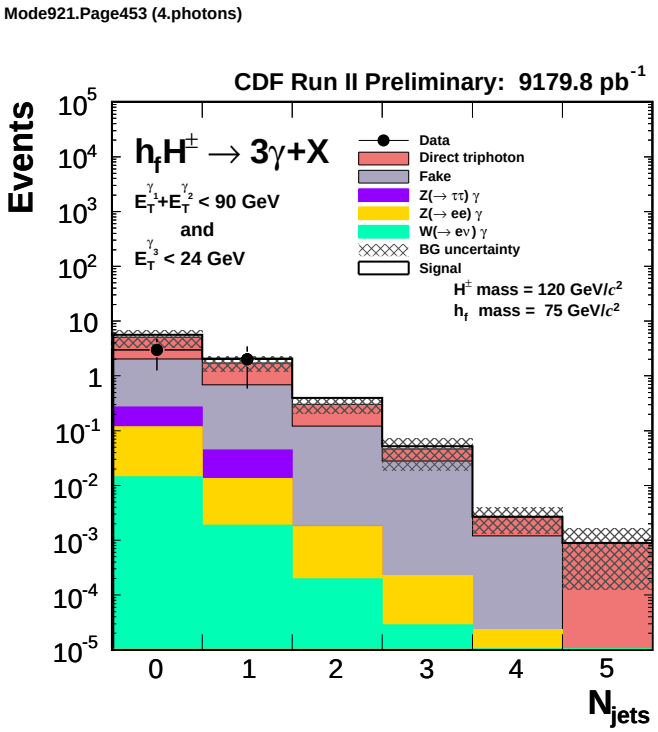

Figure 49: The number of jets in the central region with $E_T > 10$ GeV for the $3\gamma + X$ events with $E_T^{\gamma 1} + E_T^{\gamma 2} < 90$ GeV and $E_T^{\gamma 3} < 24$ GeV, expected from the SM backgrounds and expected signal events for $m_{h_f} = 75$ and $m_{H^\pm} = 120$ GeV.

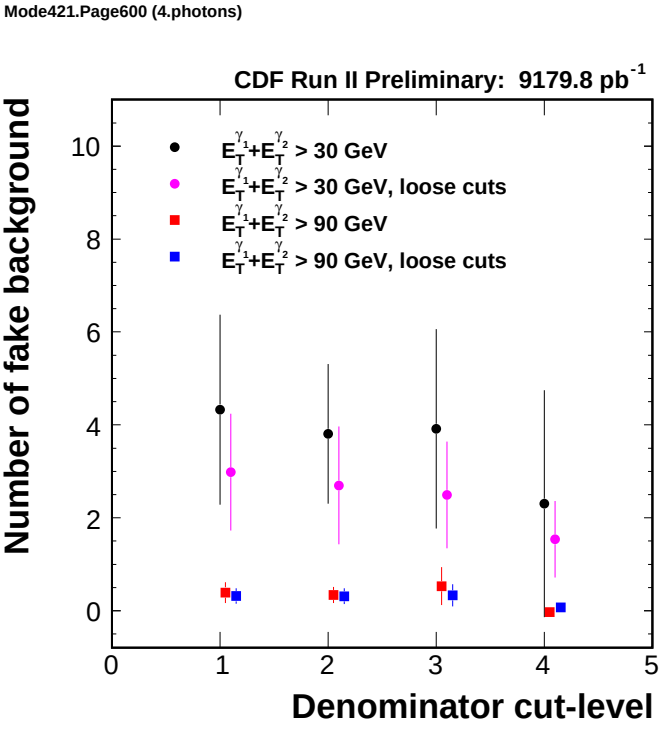

Figure 50: The numbers of expected fake-backgrounds obtained by changing the tightness of the cuts for denominator objects as explained in the texts. Our nominal analysis corresponds to the cut-level of 1 with using the loose cuts.

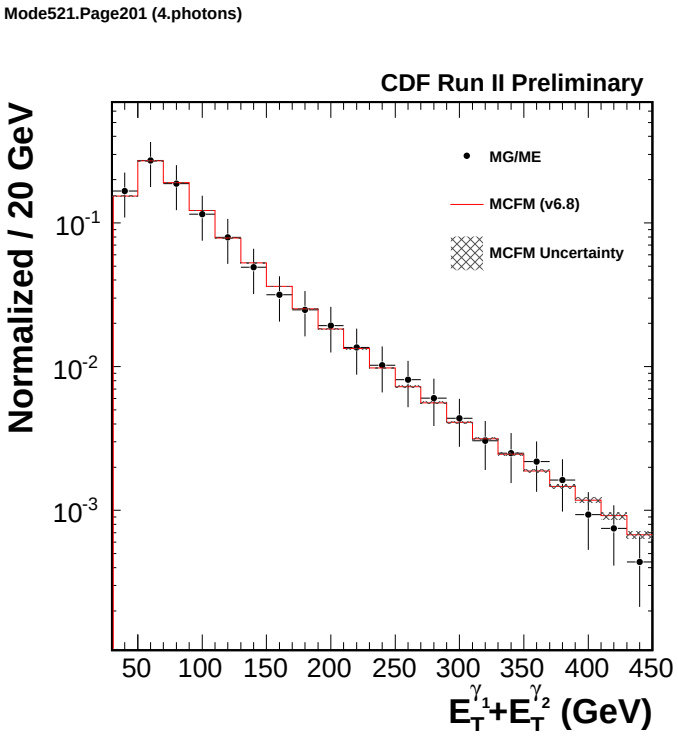

Figure 51: Comparison of $E_T^{\gamma 1} + E_T^{\gamma 2}$ distributions between the `MadGraph`/`MadEvent` and `MCFM`.

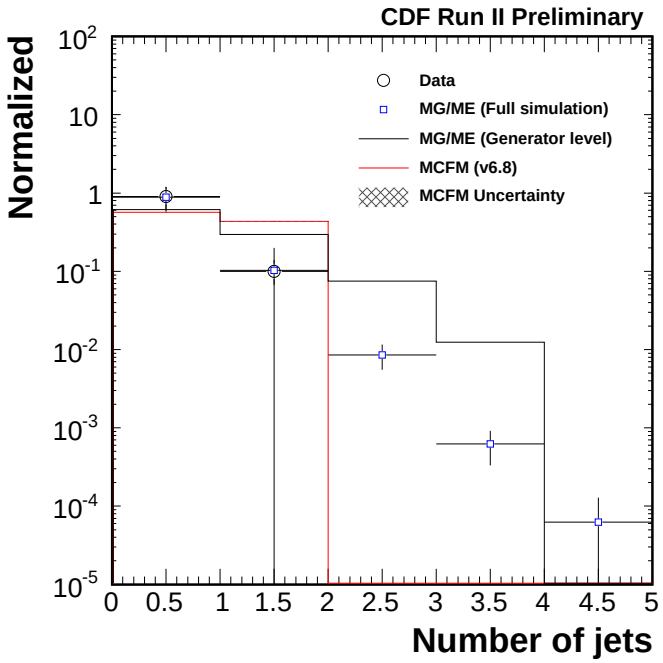

Figure 52: Jet multiplicity.

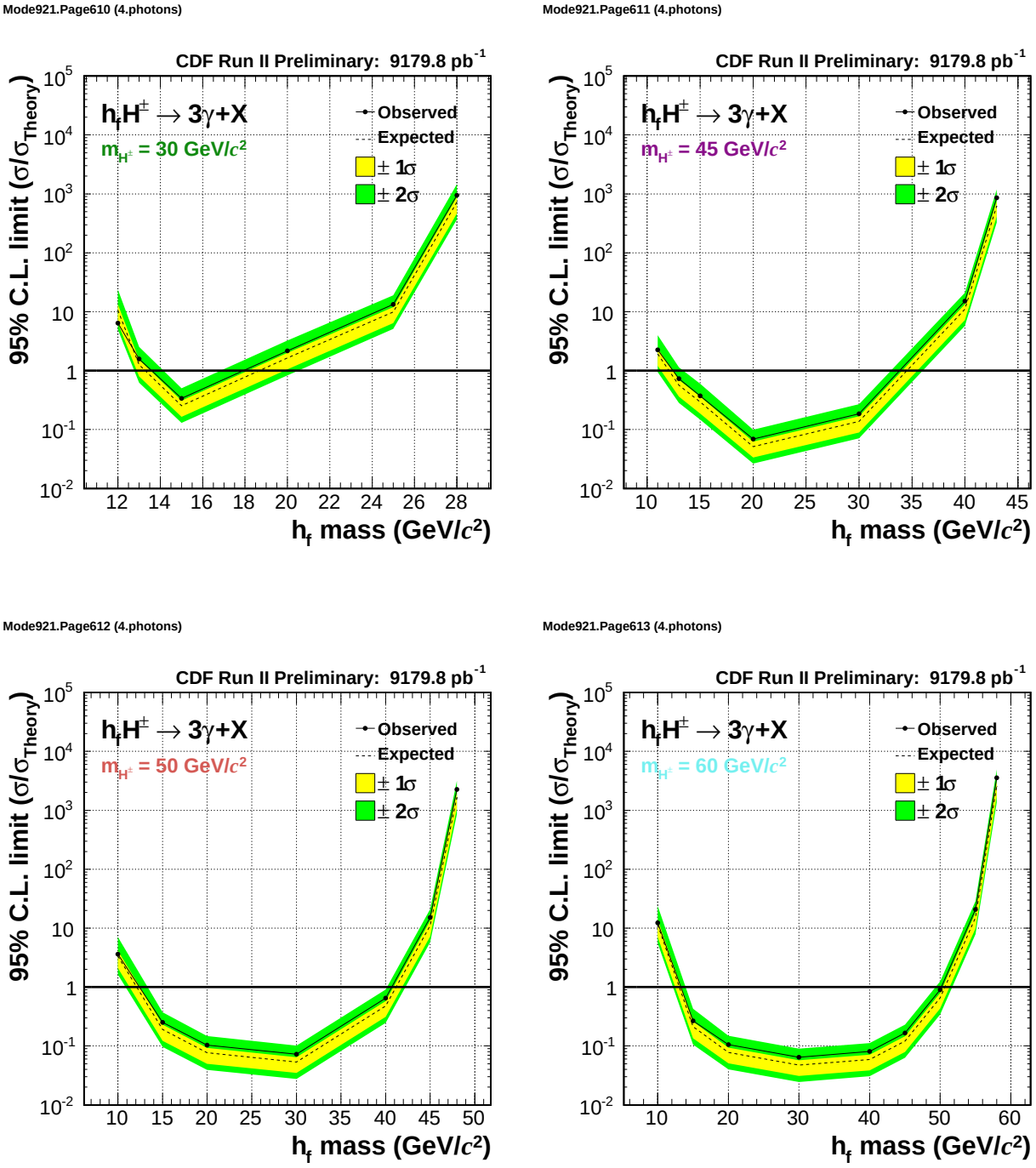

Figure 53: The expected 95% C.L. cross section limits (solid lines) and theoretical cross sections (dashed lines) calculated for the case of applying $E_T^{\gamma 1} + E_T^{\gamma 2} > 90$ GeV.

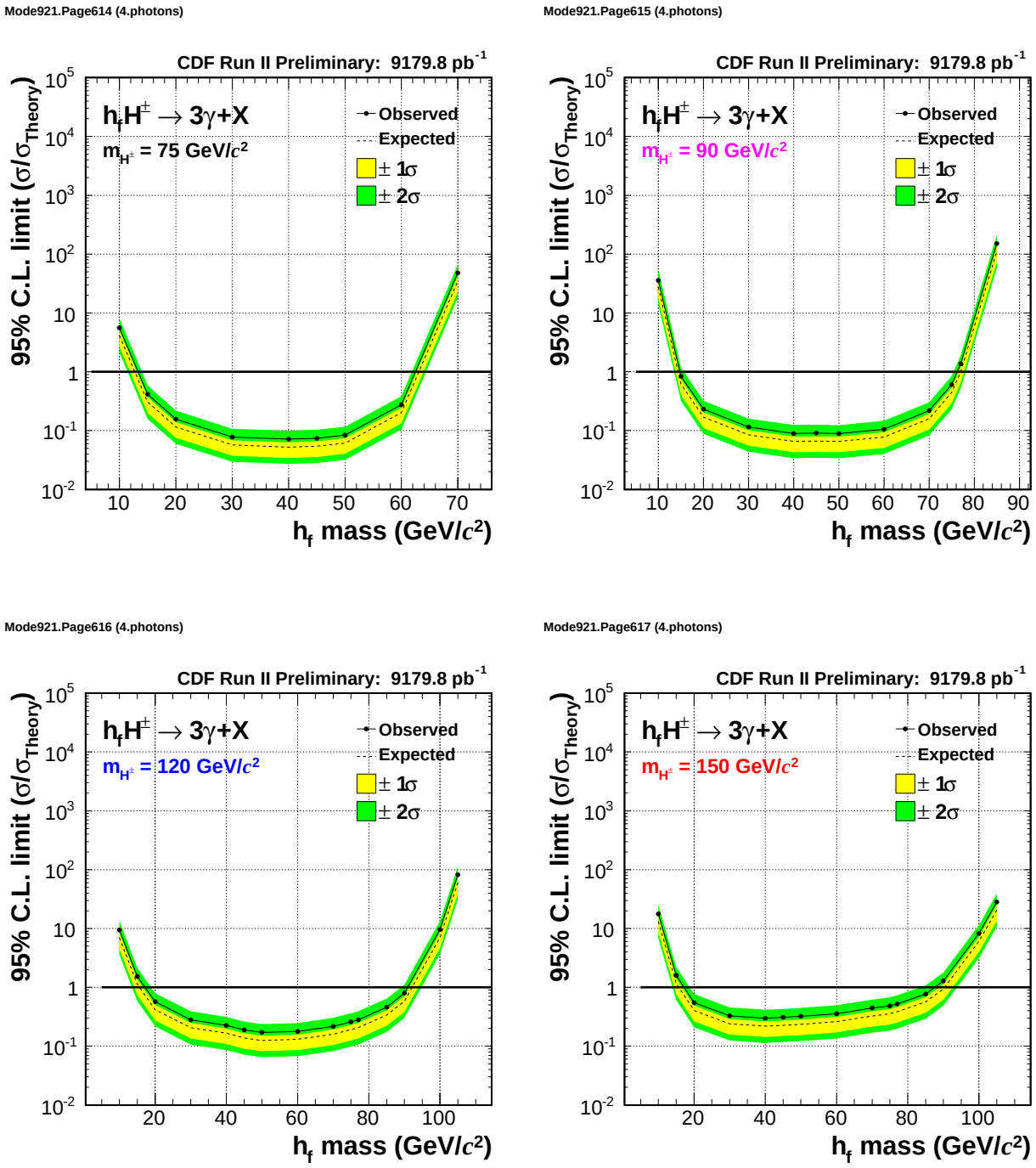

Figure 54: The expected 95% C.L. cross section limits (solid lines) and theoretical cross sections (dashed lines) calculated for the case of applying $E_T^{\gamma 1} + E_T^{\gamma 2} > 90$ GeV.

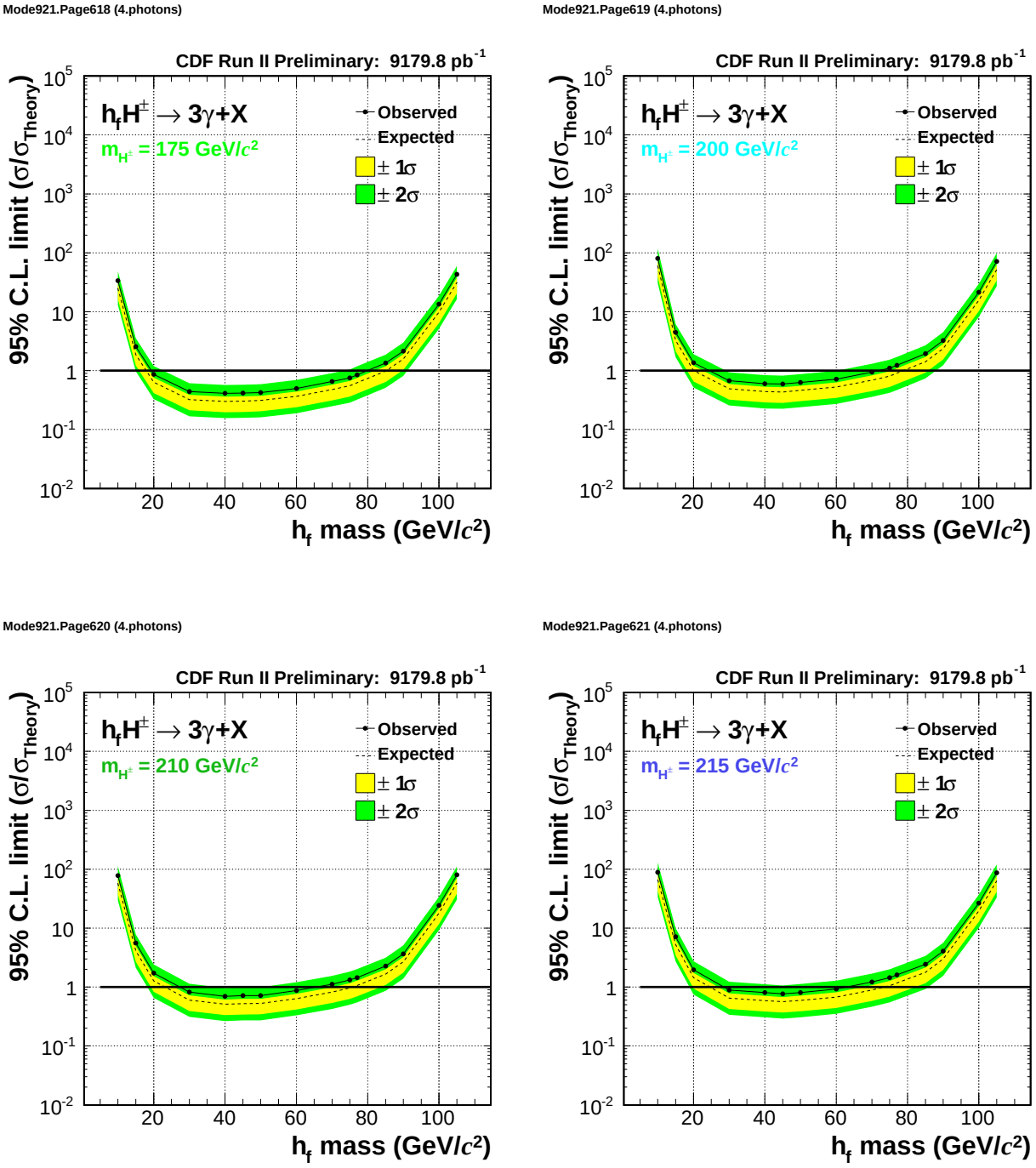

Figure 55: The expected 95% C.L. cross section limits (solid lines) and theoretical cross sections (dashed lines) calculated for the case of applying $E_T^{\gamma 1} + E_T^{\gamma 2} > 90$ GeV.

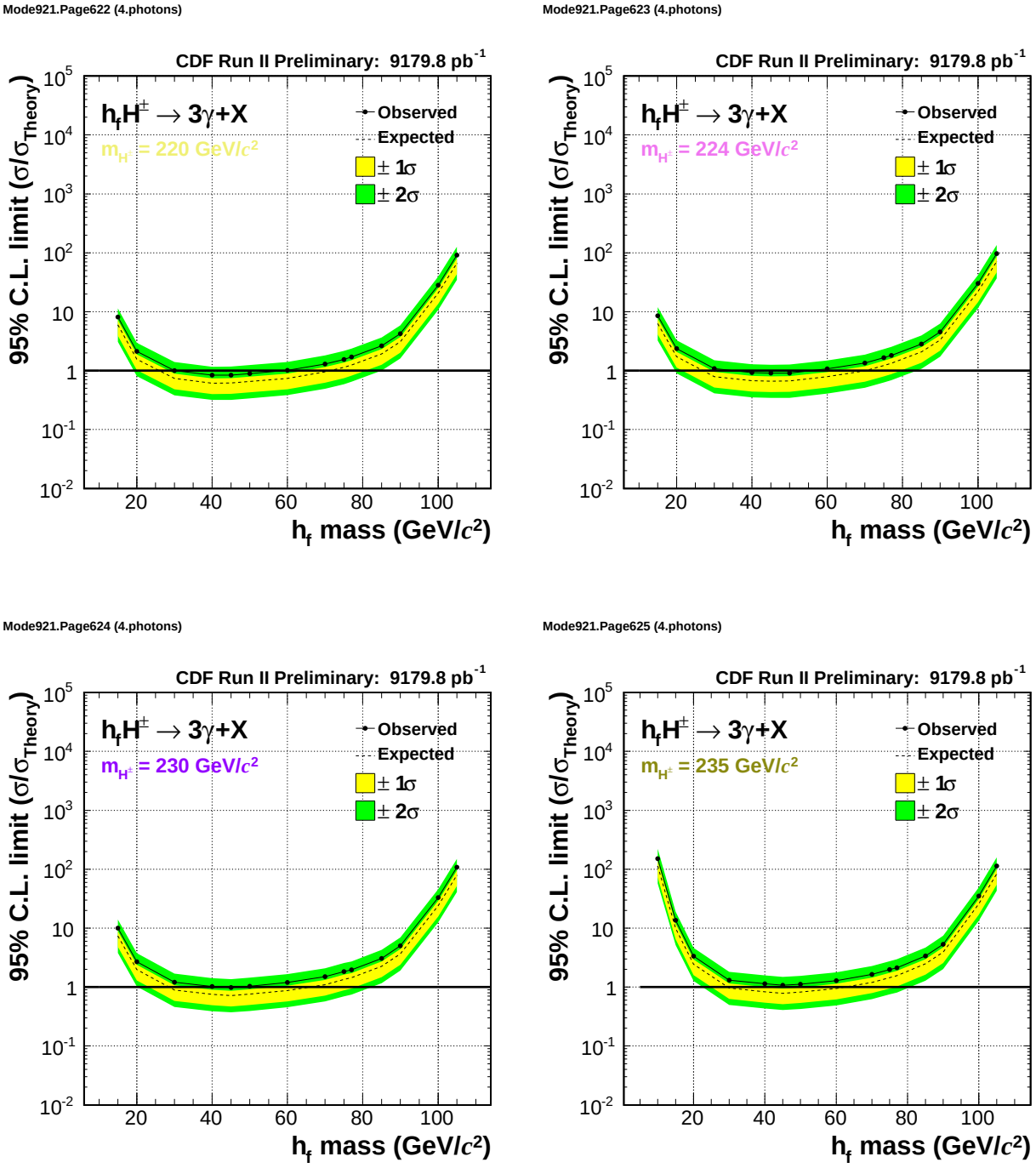

Figure 56: The expected 95% C.L. cross section limits (solid lines) and theoretical cross sections (dashed lines) calculated for the case of applying $E_T^{\gamma 1} + E_T^{\gamma 2} > 90$ GeV.

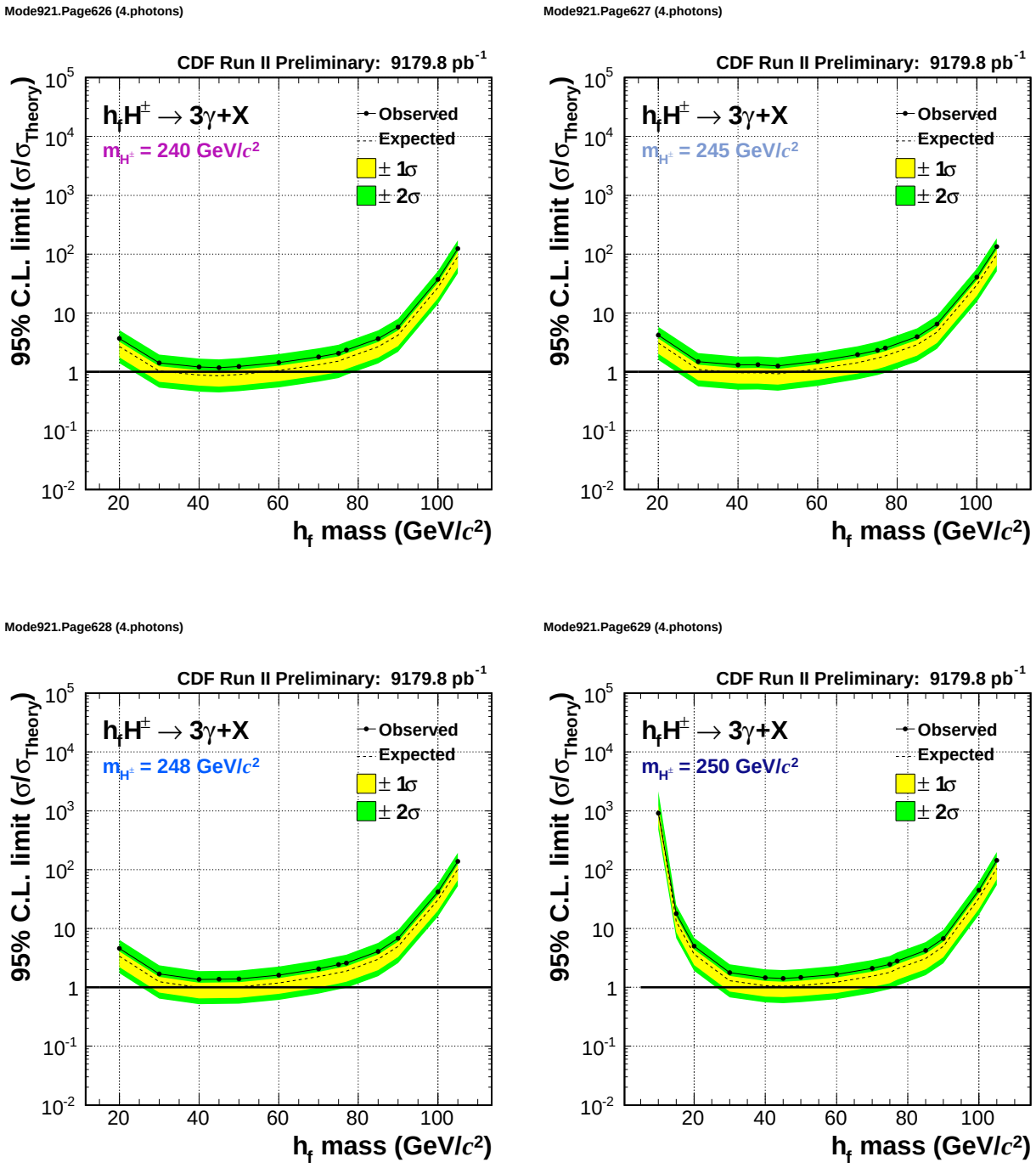

Figure 57: The expected 95% C.L. cross section limits (solid lines) and theoretical cross sections (dashed lines) calculated for the case of applying $E_T^{\gamma 1} + E_T^{\gamma 2} > 90$ GeV.

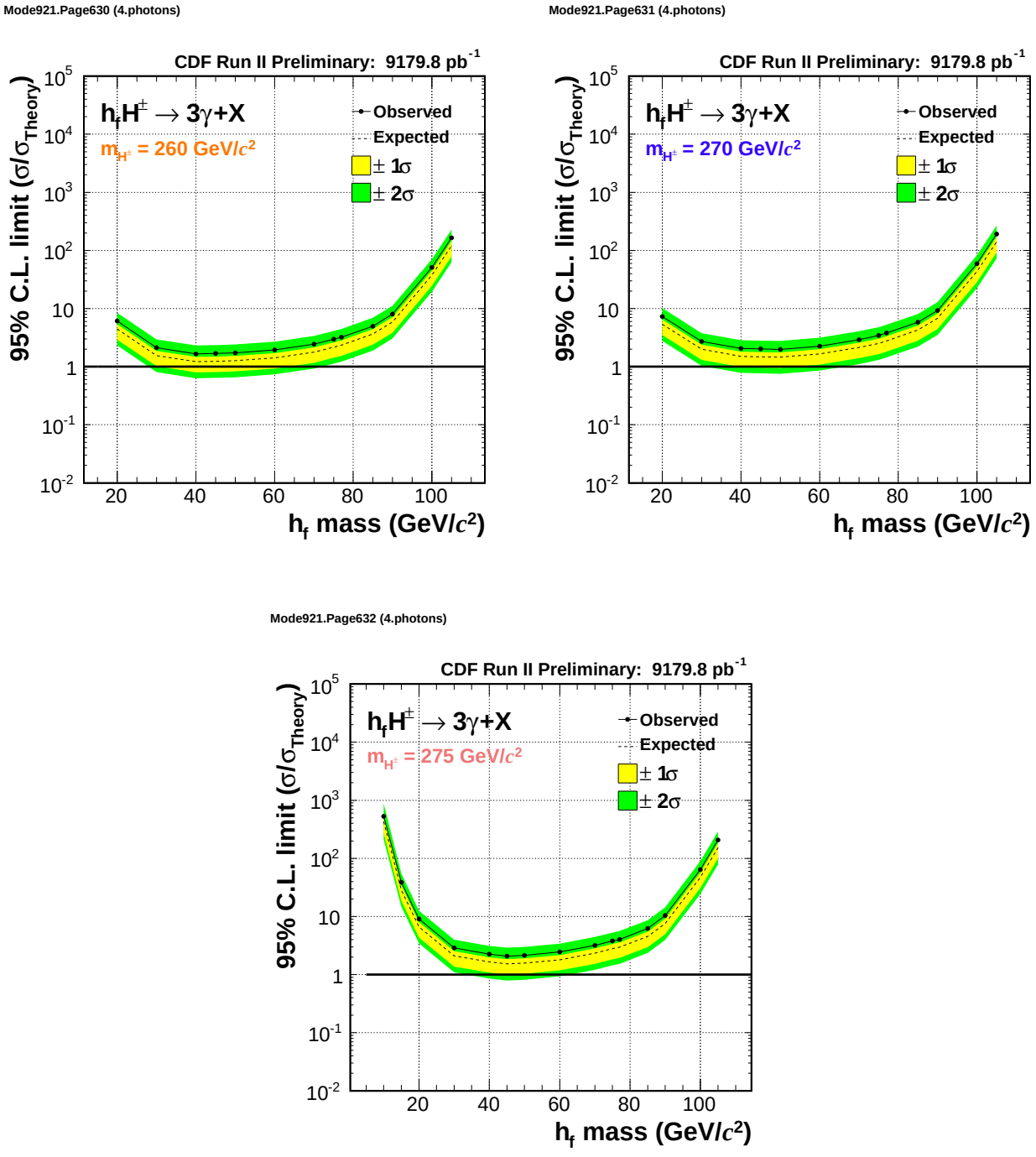

Figure 58: The expected 95% C.L. cross section limits (solid lines) and theoretical cross sections (dashed lines) calculated for the case of applying $E_T^{\gamma 1} + E_T^{\gamma 2} > 90$ GeV.

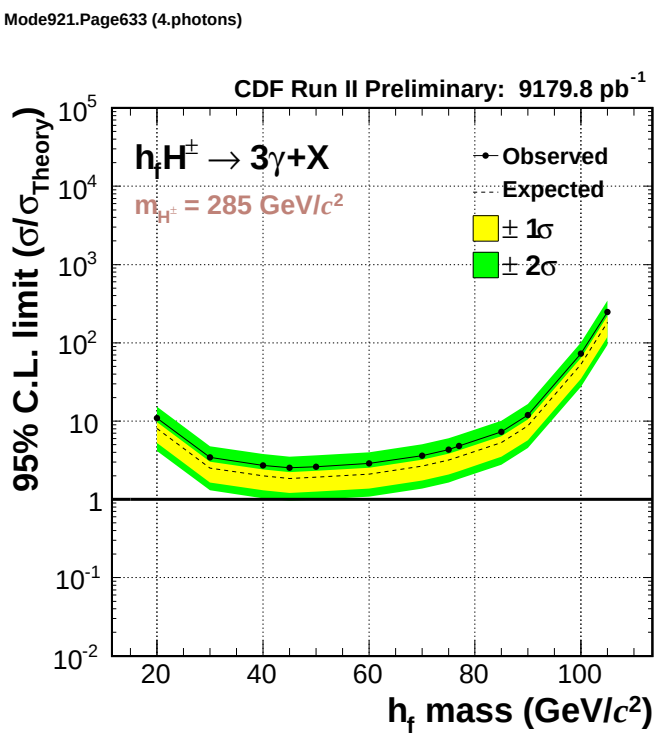

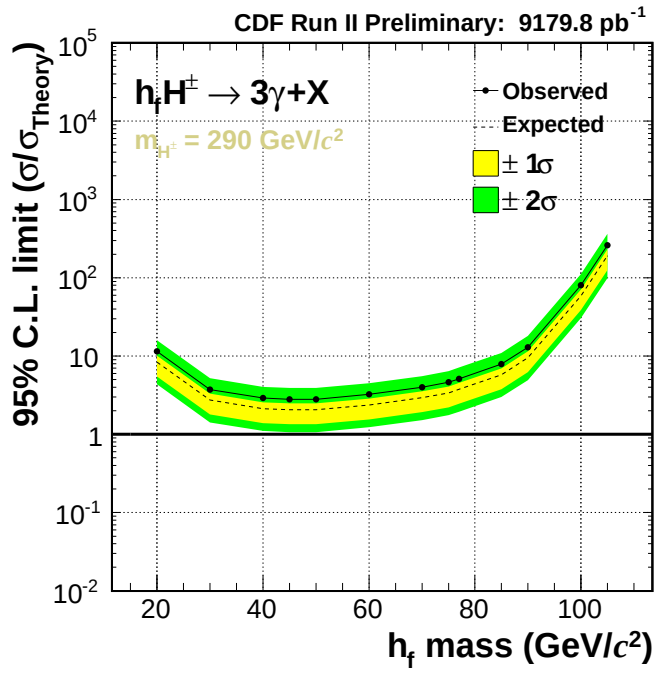

Figure 59: The expected 95% C.L. cross section limits (solid lines) and theoretical cross sections (dashed lines) calculated for the case of applying $E_T^{\gamma 1} + E_T^{\gamma 2} > 90$ GeV.

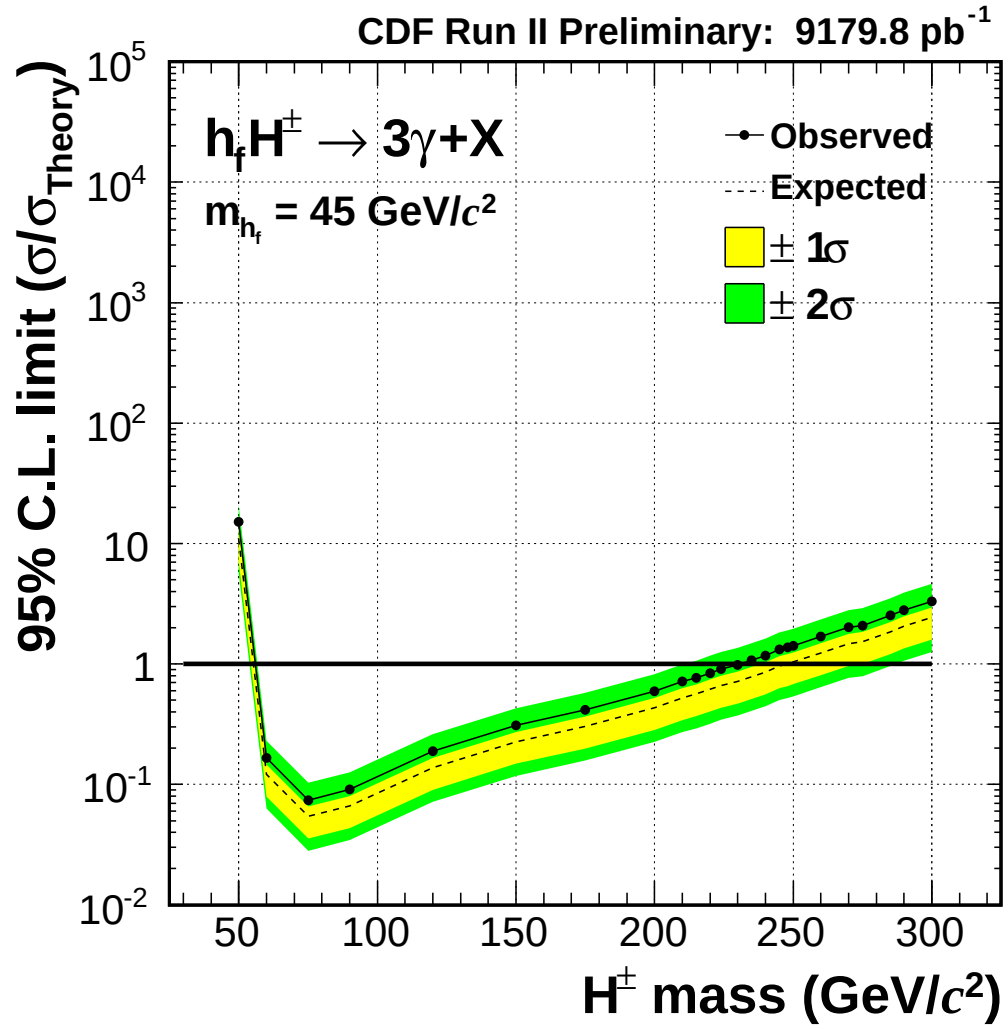

Figure 60: The expected 95% C.L. cross section limits (solid lines) and theoretical cross sections (dashed lines) calculated for the case of applying $E_T^{\gamma_1} + E_T^{\gamma_2} > 90$ GeV.

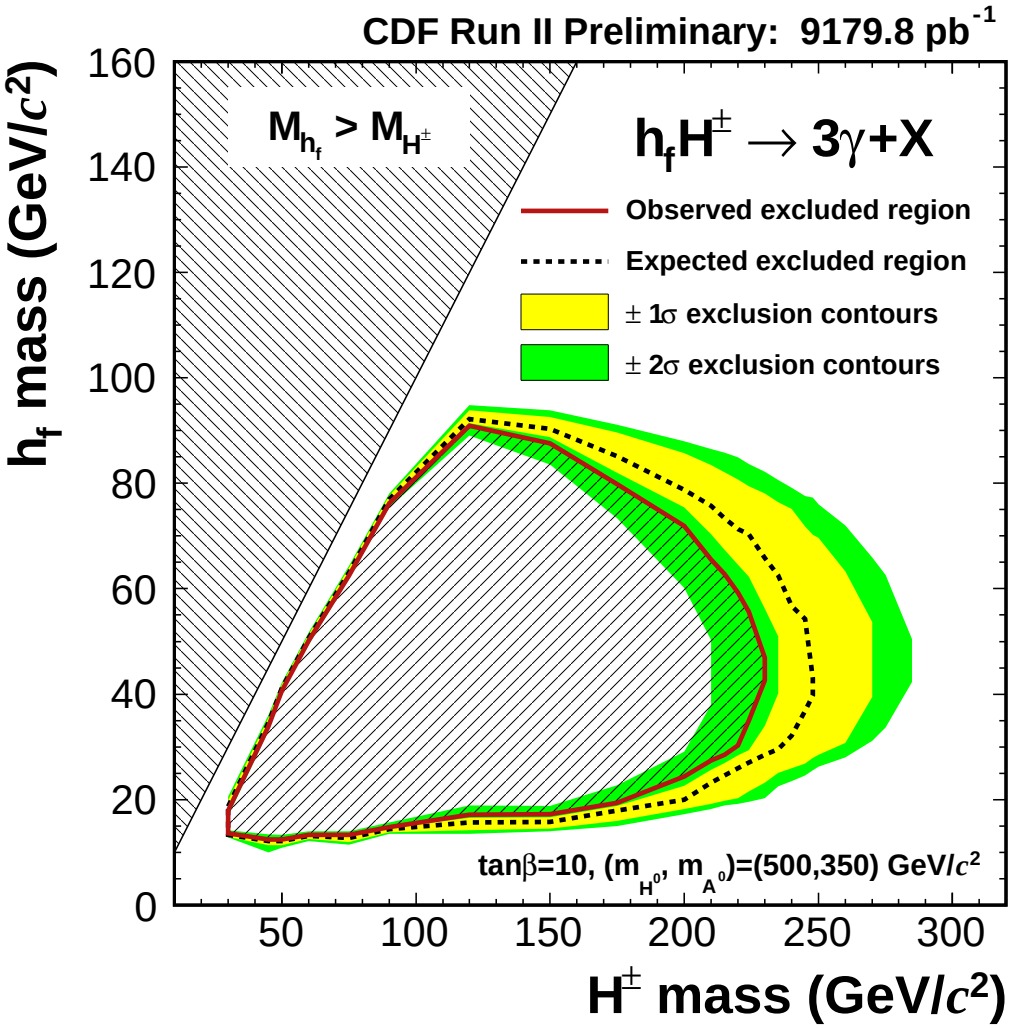

Figure 61: The expected and observed 95% C.L. excluded mass region calculated for the case of applying $E_T^{\gamma_1} + E_T^{\gamma_2} > 90$ GeV.

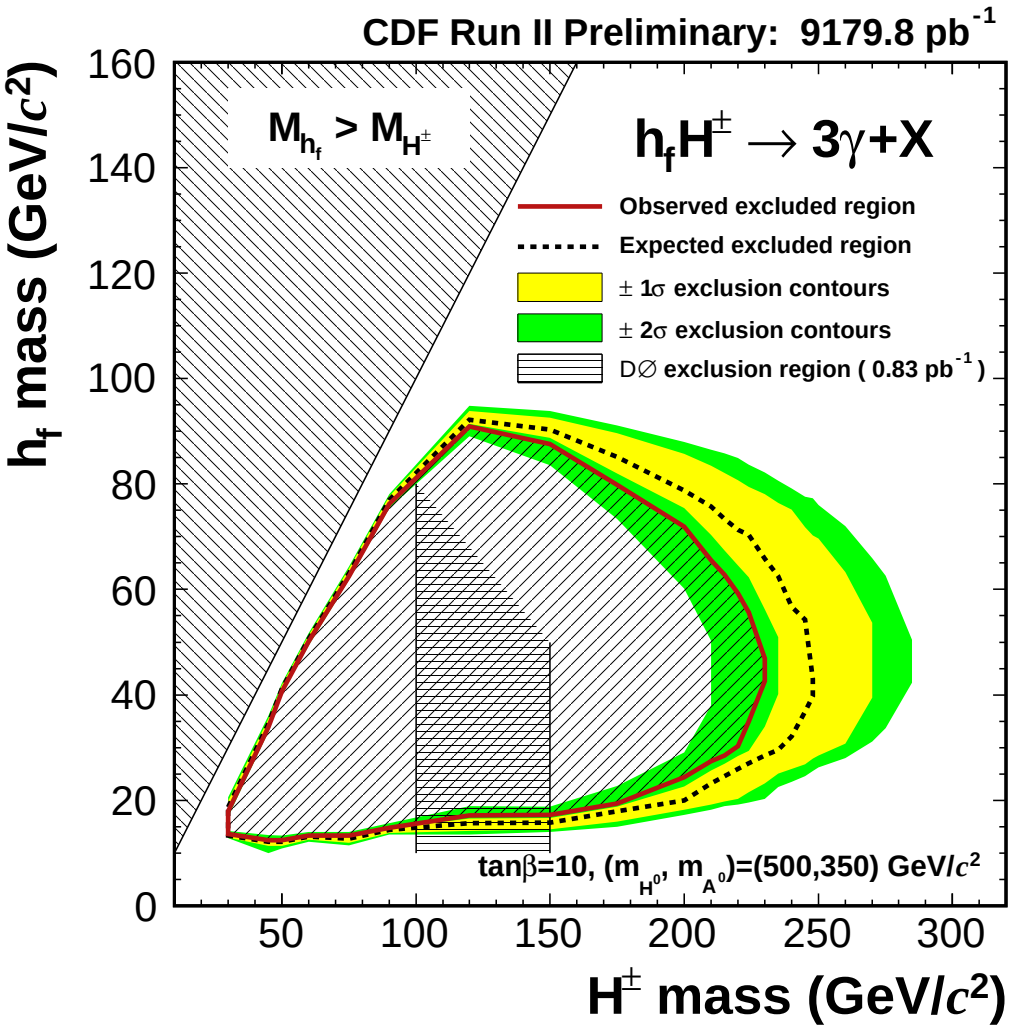

Figure 62: The expected and observed 95% C.L. excluded mass region calculated for the case of applying $E_T^{\gamma_1} + E_T^{\gamma_2} > 90$ GeV. As a reference, the excluded h_f masses by the DØ analysis for $\tan\beta = 30$ is also shown in terms of two vertical lines. The shaded region between the lines are considered to be naturally excluded.

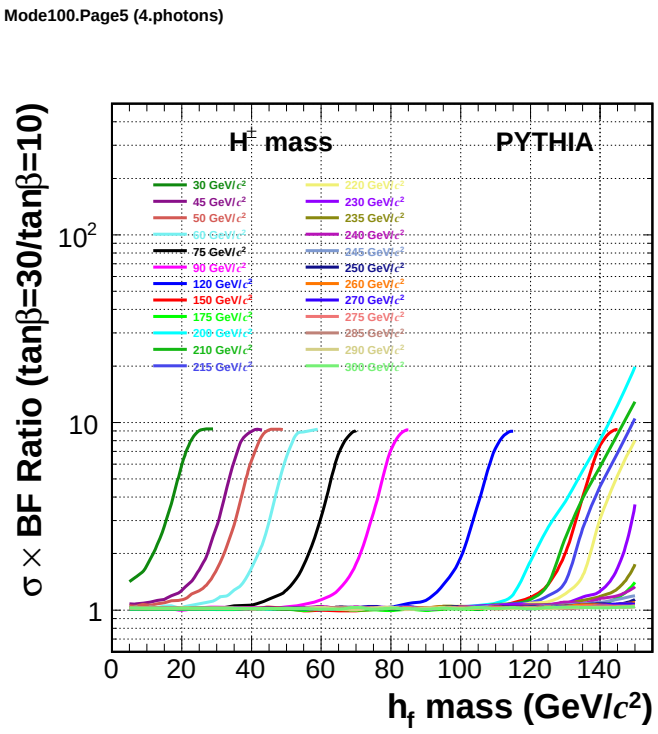

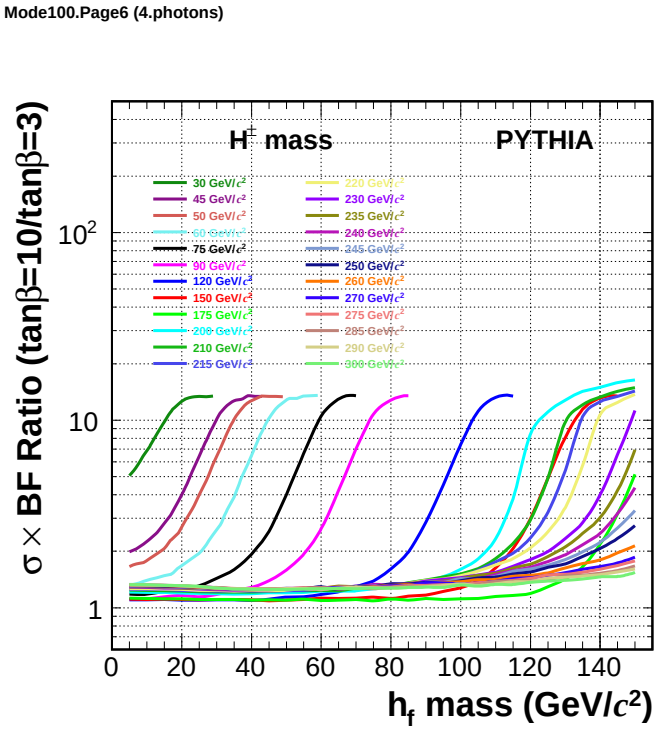

Figure 63: The ratio of the $\sigma(p\bar{p} \to h_f H^{\pm}) \times \mathcal{B}(H^{\pm} \to h_f W^*) \times [\mathcal{B}(h_f \to 2\gamma)]^2$ between the cases of $\tan\beta = 30$ and $\tan\beta = 10$ (the top plot), and between the cases of $\tan\beta = 10$ and $\tan\beta = 3$ (the bottom plot).

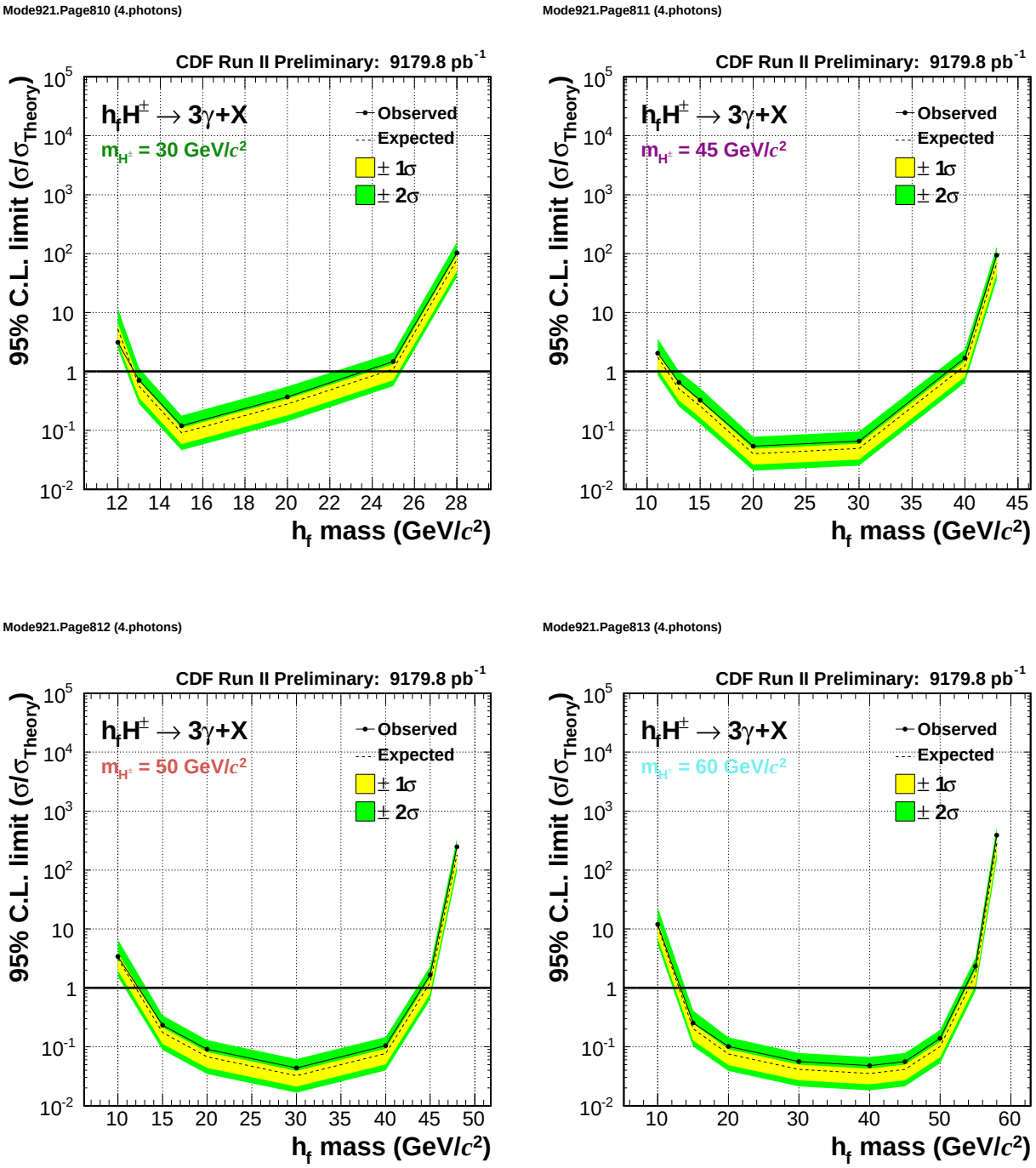

Figure 64: The expected 95% C.L. cross section limits (solid lines) and theoretical cross sections (dashed lines) calculated for the case of applying $E_T^{\gamma 1} + E_T^{\gamma 2} > 90$ GeV and $\tan\beta = 30$.

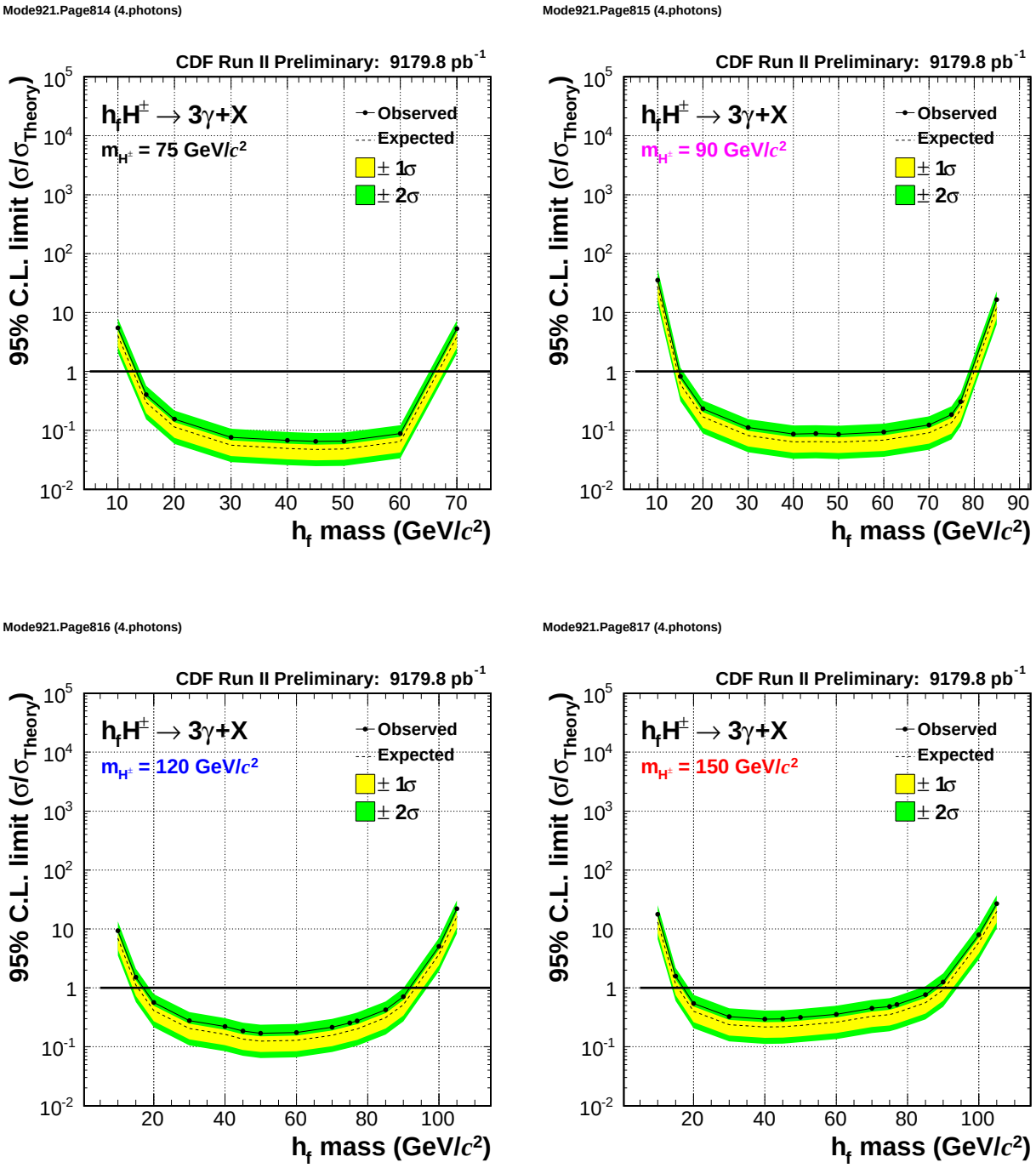

Figure 65: The expected 95% C.L. cross section limits (solid lines) and theoretical cross sections (dashed lines) calculated for the case of applying $E_T^{\gamma 1} + E_T^{\gamma 2} > 90$ GeV and $\tan\beta = 30$.

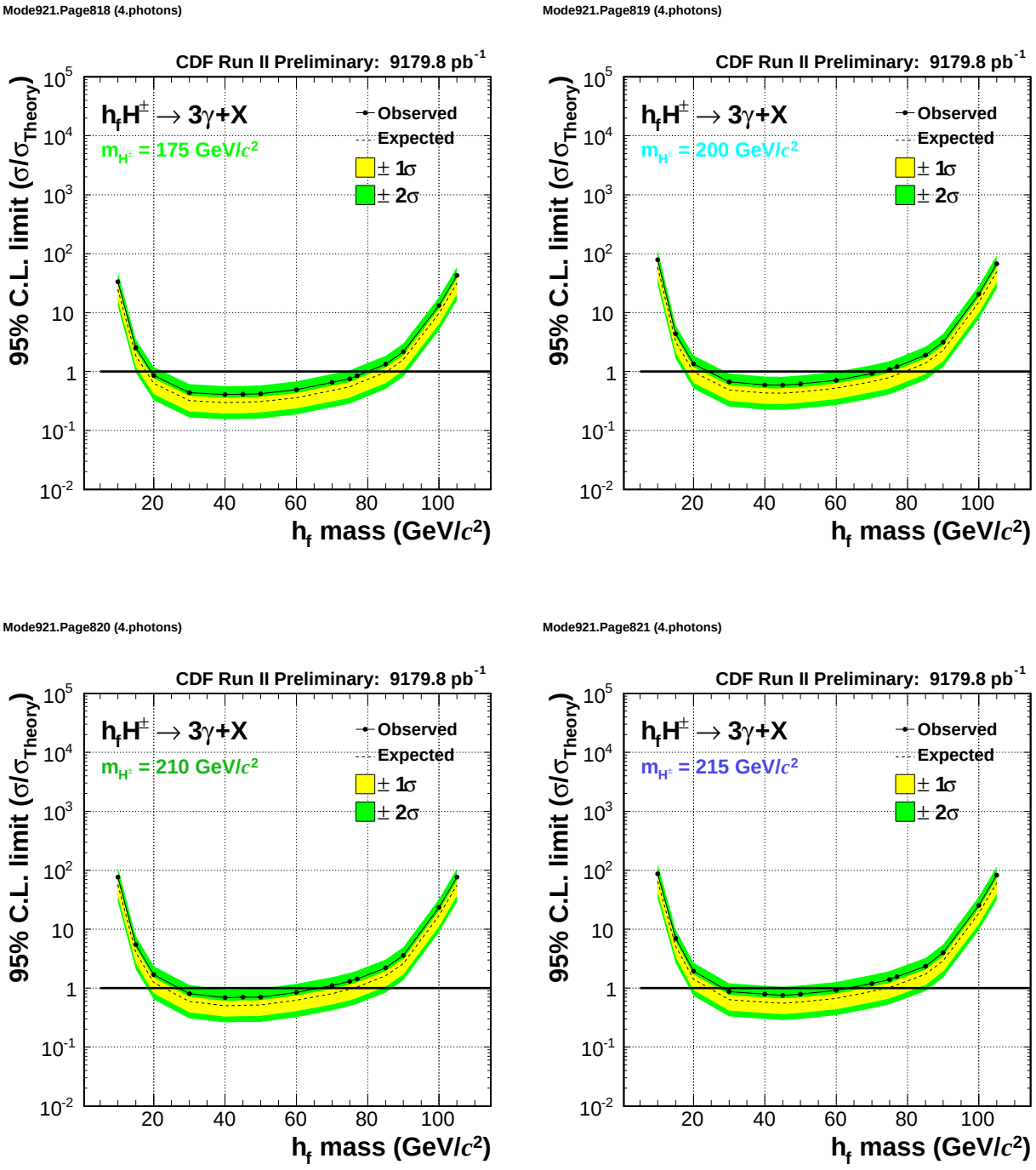

Figure 66: The expected 95% C.L. cross section limits (solid lines) and theoretical cross sections (dashed lines) calculated for the case of applying $E_T^{\gamma 1} + E_T^{\gamma 2} > 90$ GeV and $\tan\beta = 30$.

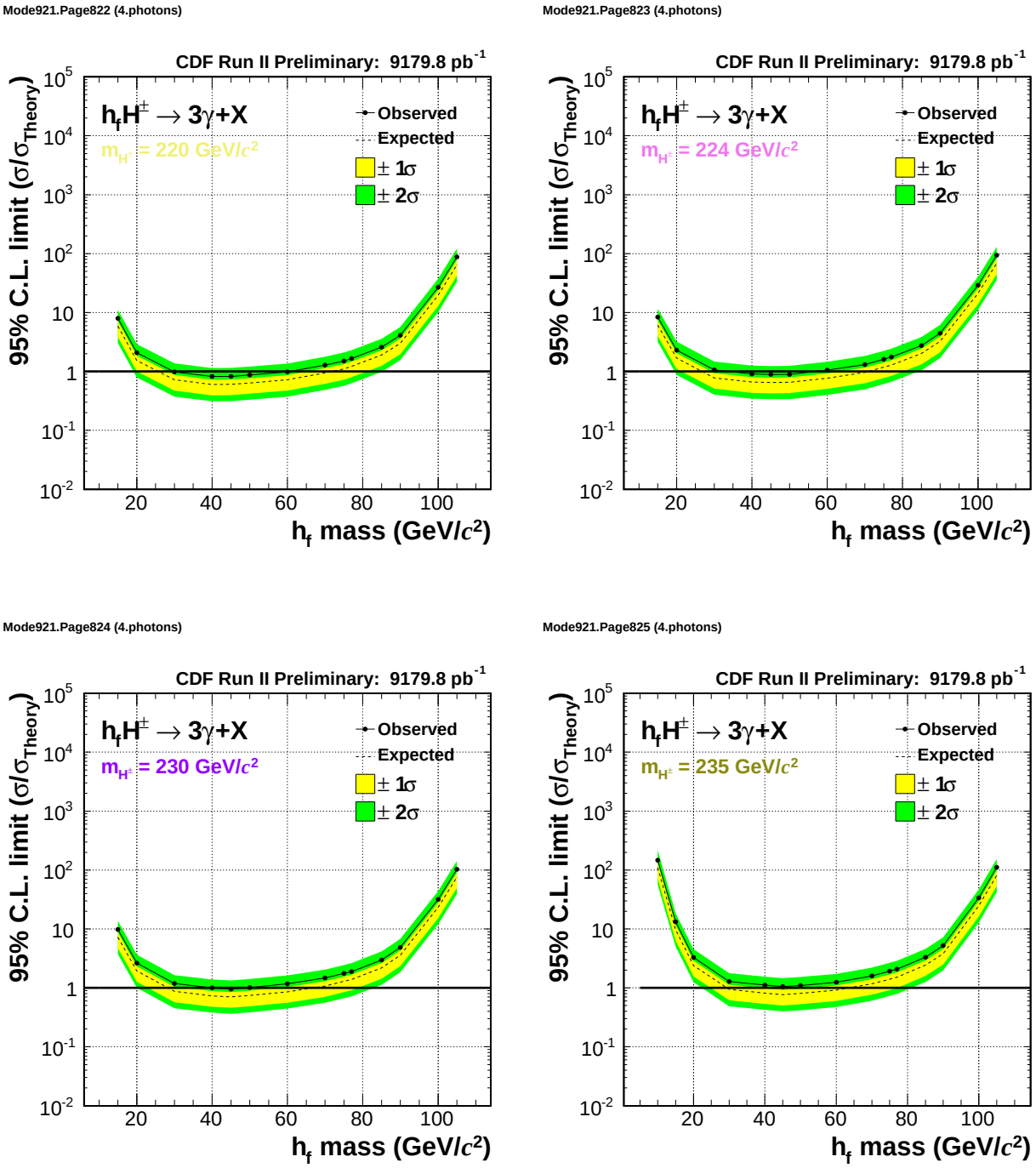

Figure 67: The expected 95% C.L. cross section limits (solid lines) and theoretical cross sections (dashed lines) calculated for the case of applying $E_T^{\gamma 1} + E_T^{\gamma 2} > 90$ GeV and $\tan\beta = 30$.

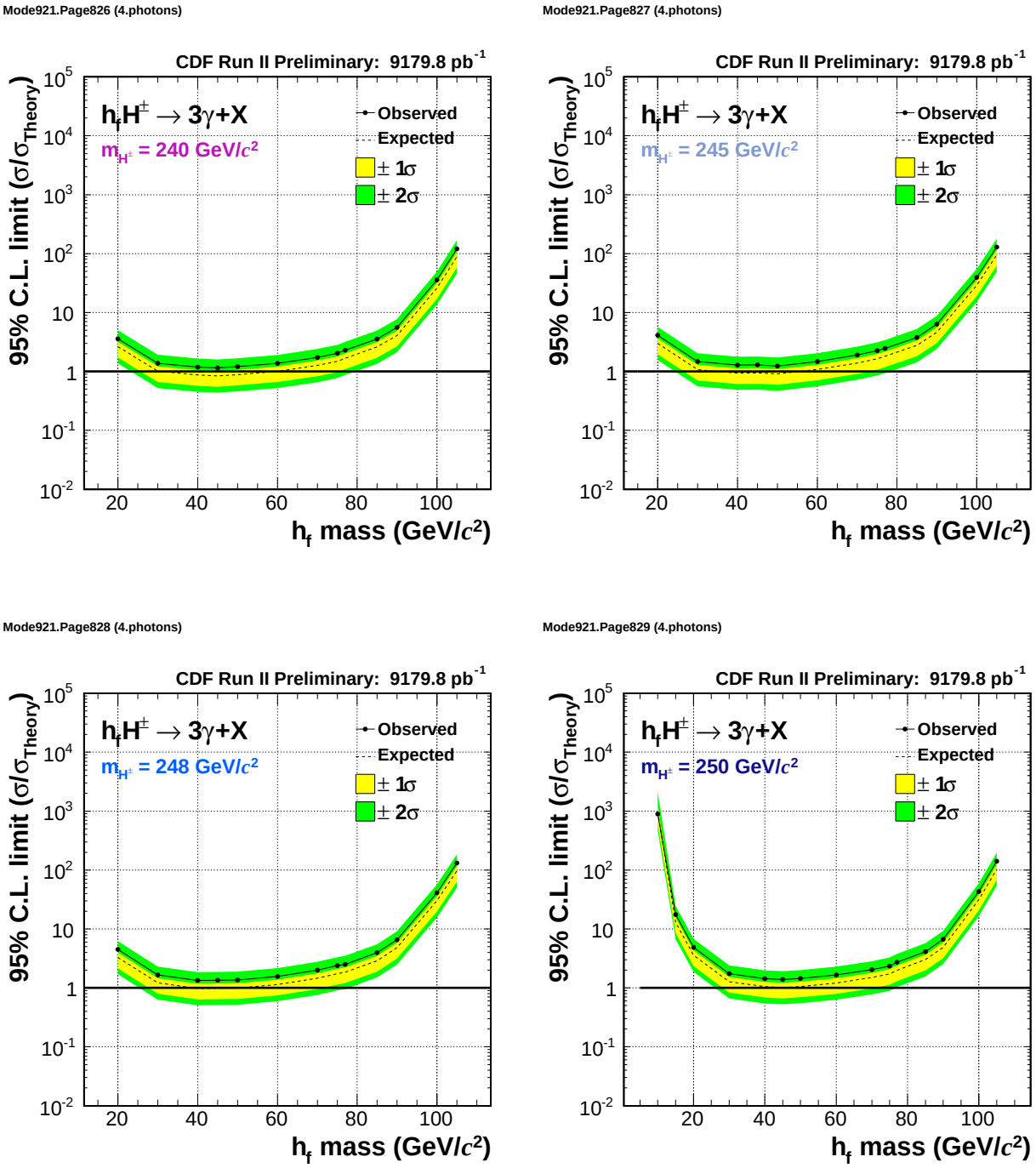

Figure 68: The expected 95% C.L. cross section limits (solid lines) and theoretical cross sections (dashed lines) calculated for the case of applying $E_T^{\gamma 1} + E_T^{\gamma 2} > 90$ GeV and $\tan\beta = 30$.

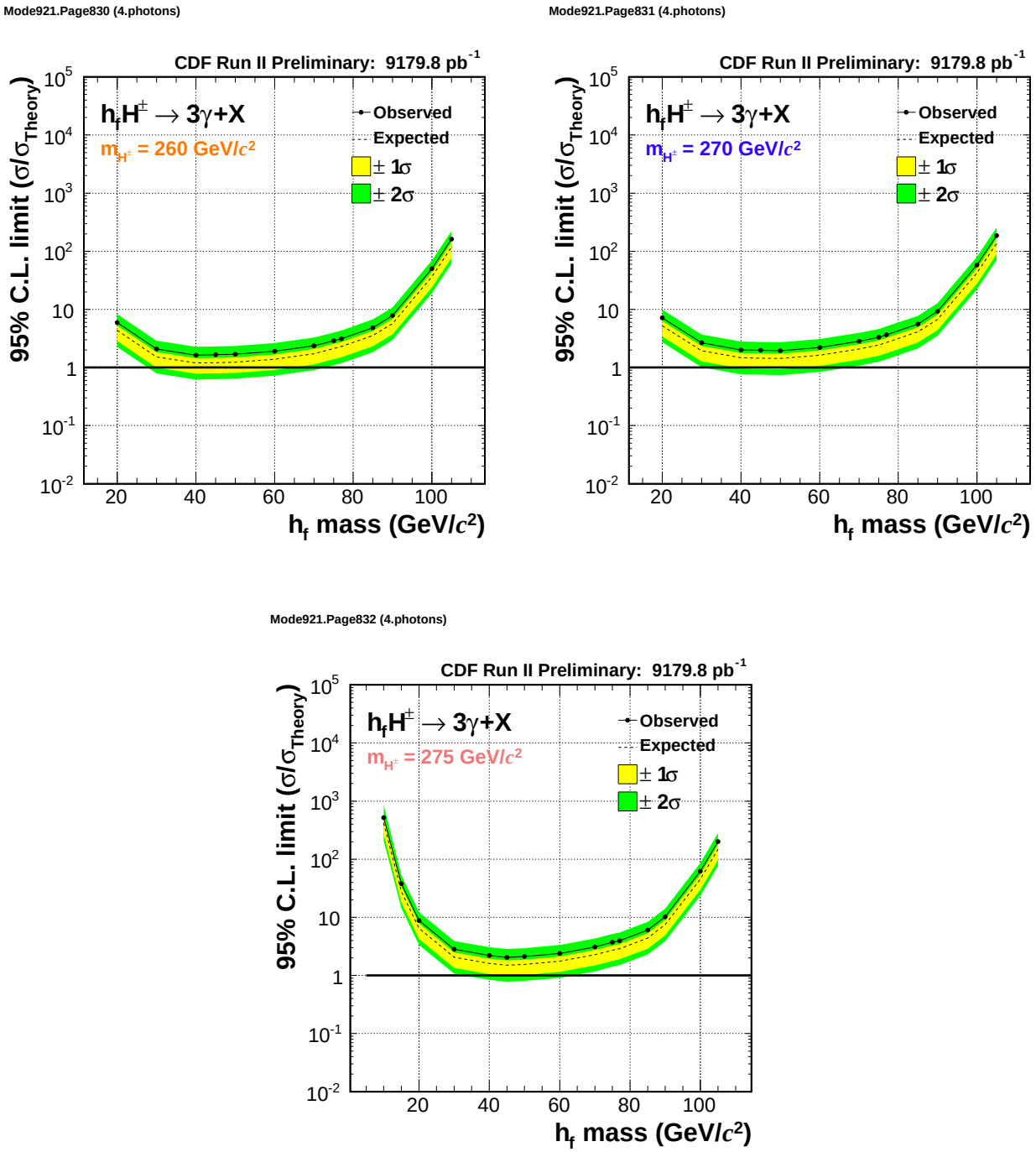

Figure 69: The expected 95% C.L. cross section limits (solid lines) and theoretical cross sections (dashed lines) calculated for the case of applying $E_T^{\gamma_1} + E_T^{\gamma_2} > 90$ GeV and $\tan\beta = 30$.

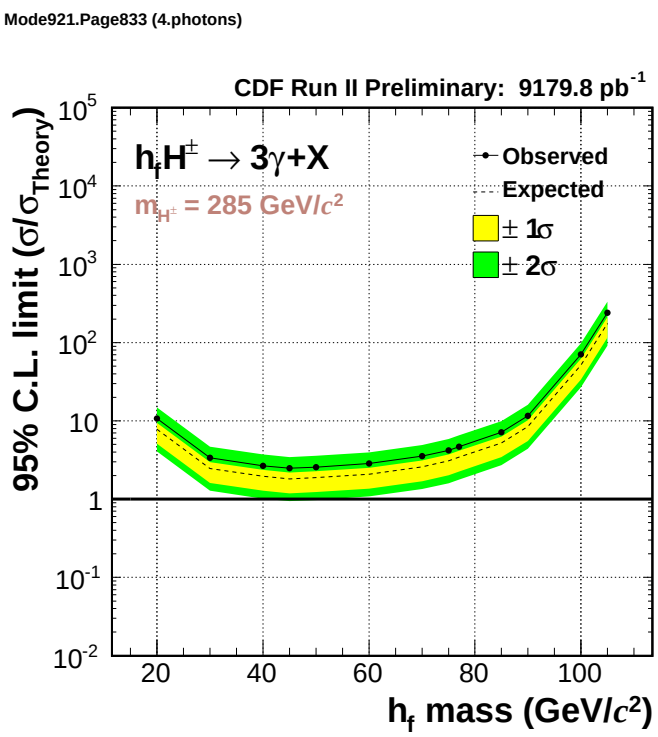

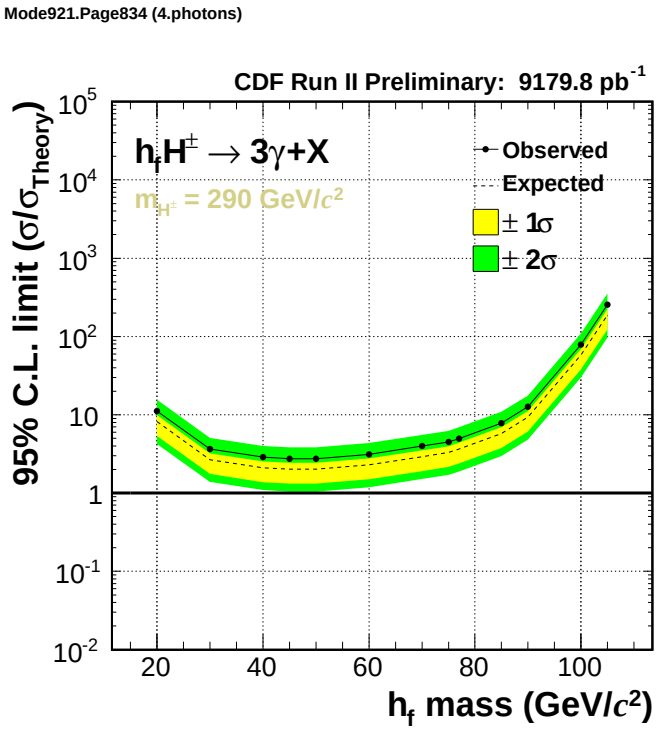

Figure 70: The expected 95% C.L. cross section limits (solid lines) and theoretical cross sections (dashed lines) calculated for the case of applying $E_T^{\gamma 1} + E_T^{\gamma 2} > 90$ GeV and $\tan\beta = 30$.

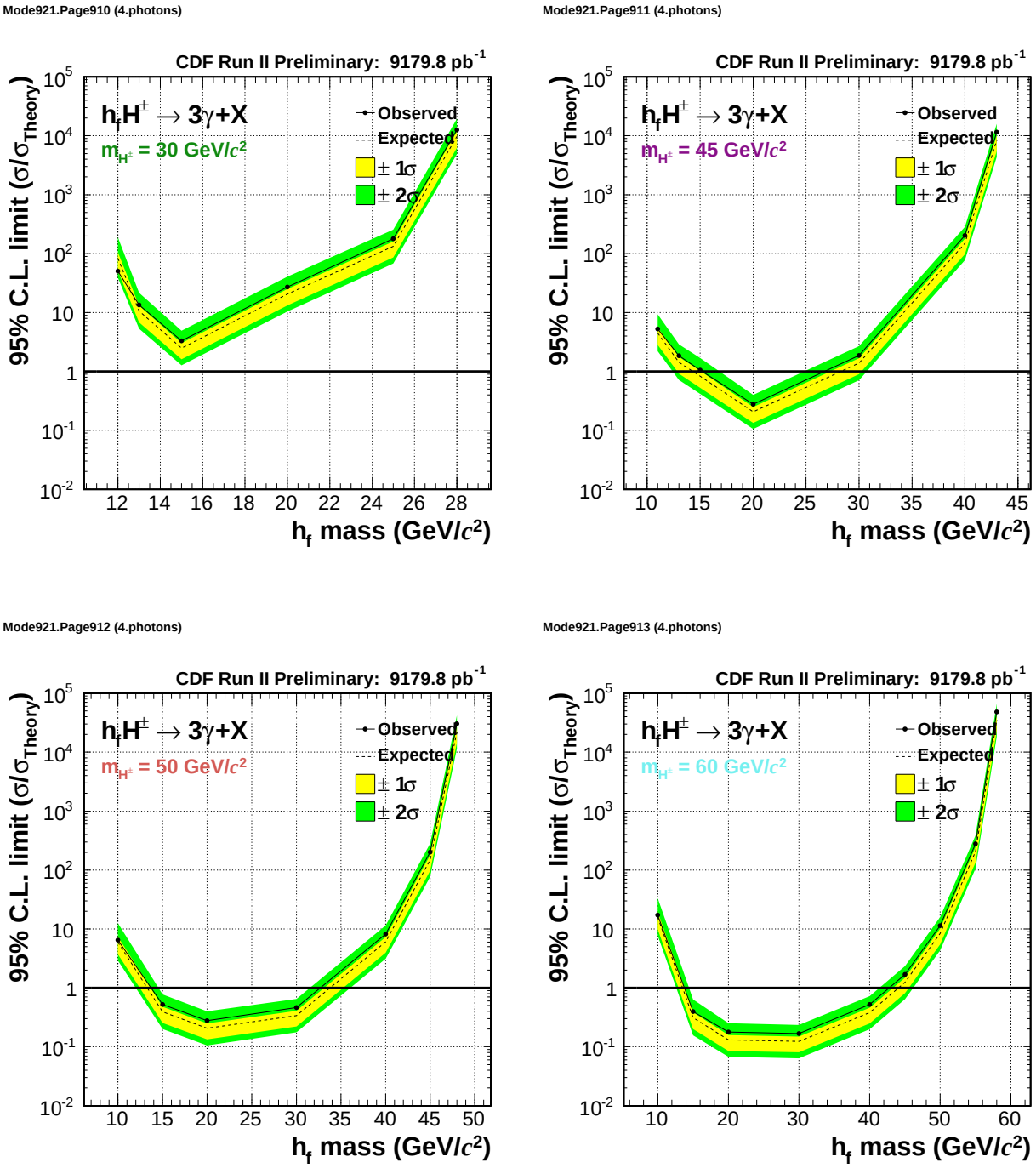

Figure 71: The expected 95% C.L. cross section limits (solid lines) and theoretical cross sections (dashed lines) calculated for the case of applying $E_T^{\gamma 1} + E_T^{\gamma 2} > 90$ GeV and $\tan\beta = 3$.

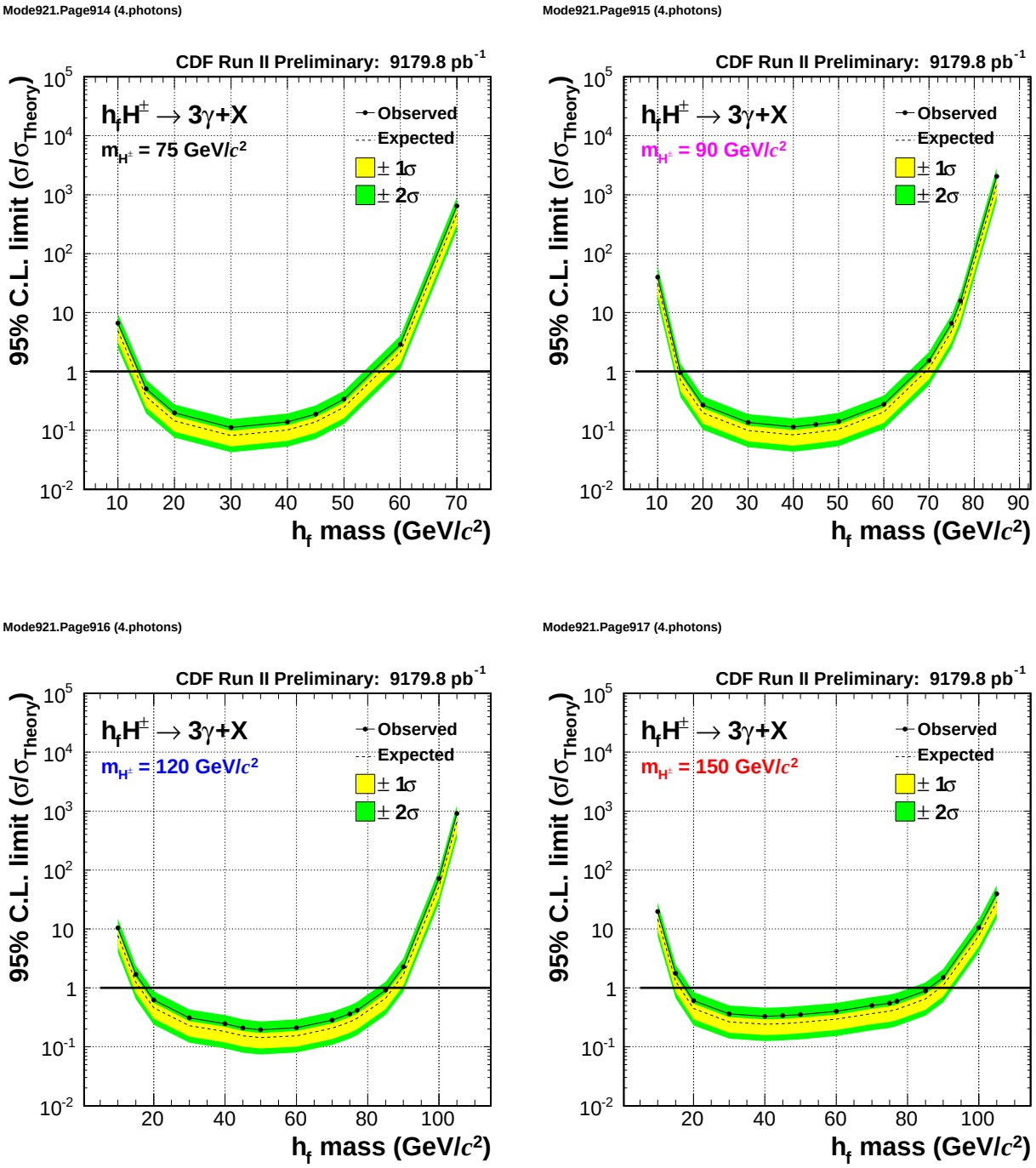

Figure 72: The expected 95% C.L. cross section limits (solid lines) and theoretical cross sections (dashed lines) calculated for the case of applying $E_T^{\gamma 1} + E_T^{\gamma 2} > 90$ GeV and $\tan\beta = 3$.

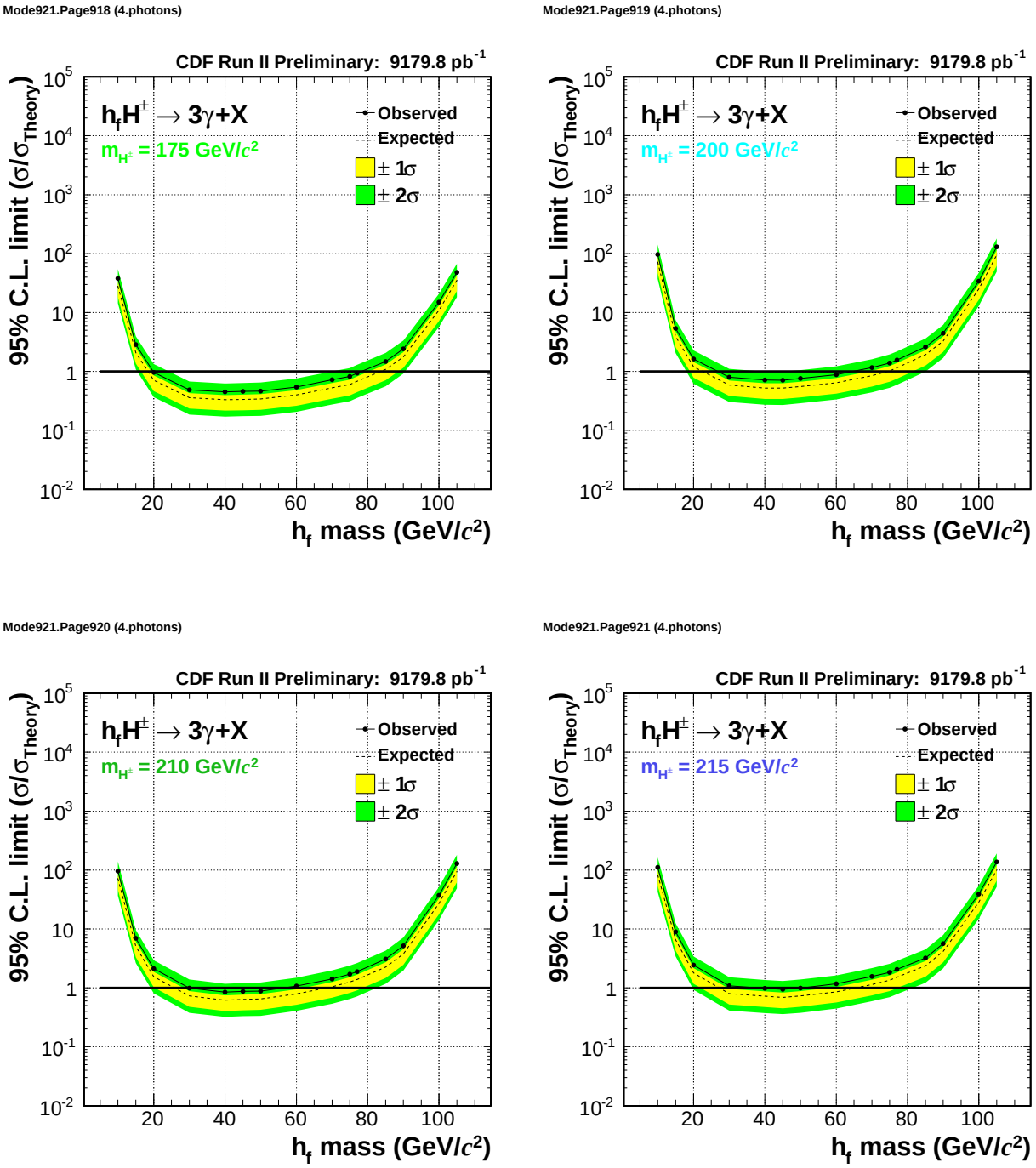

Figure 73: The expected 95% C.L. cross section limits (solid lines) and theoretical cross sections (dashed lines) calculated for the case of applying $E_T^{\gamma 1} + E_T^{\gamma 2} > 90$ GeV and $\tan\beta = 3$.

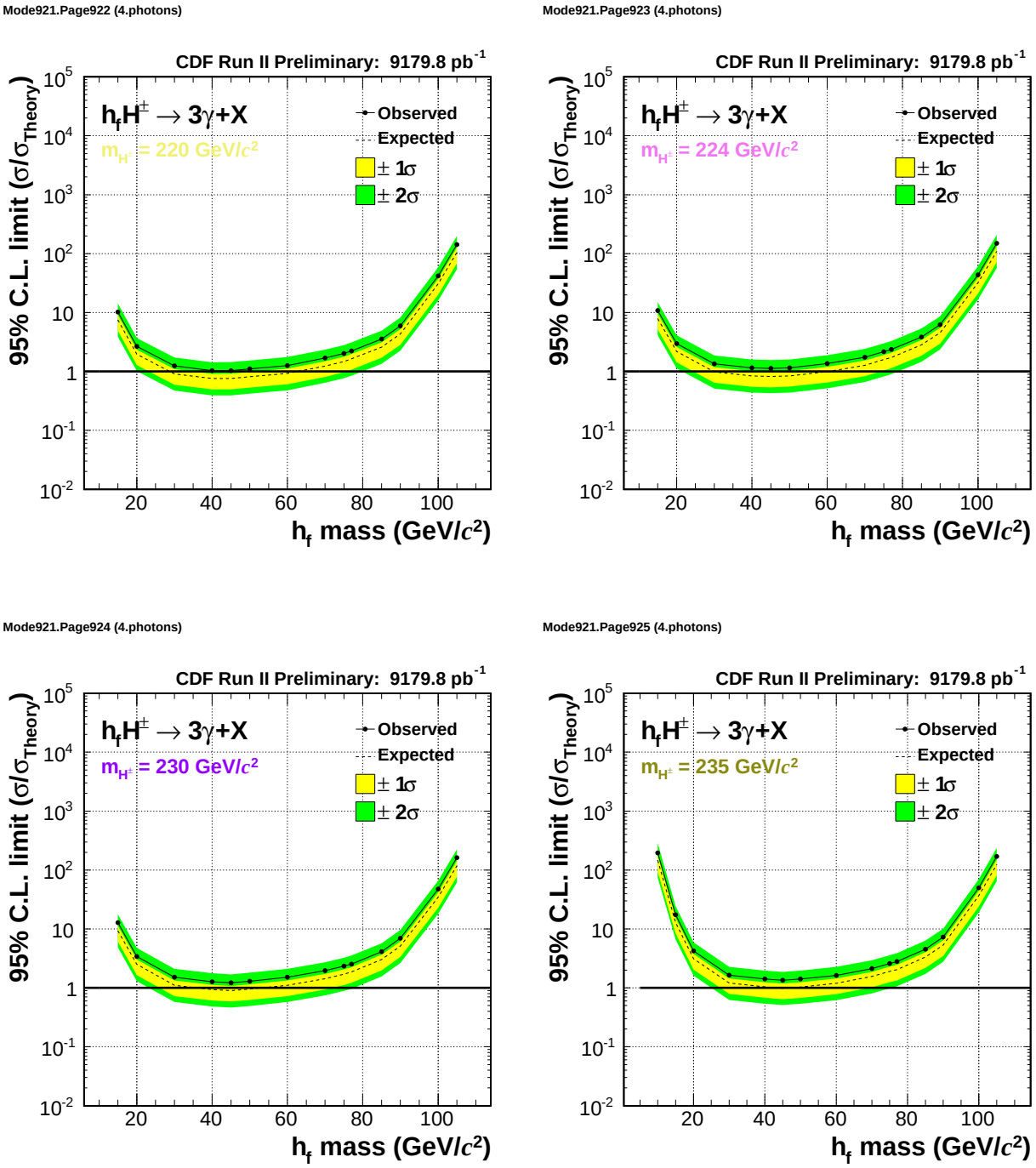

Figure 74: The expected 95% C.L. cross section limits (solid lines) and theoretical cross sections (dashed lines) calculated for the case of applying $E_T^{\gamma 1} + E_T^{\gamma 2} > 90$ GeV and $\tan\beta = 3$.

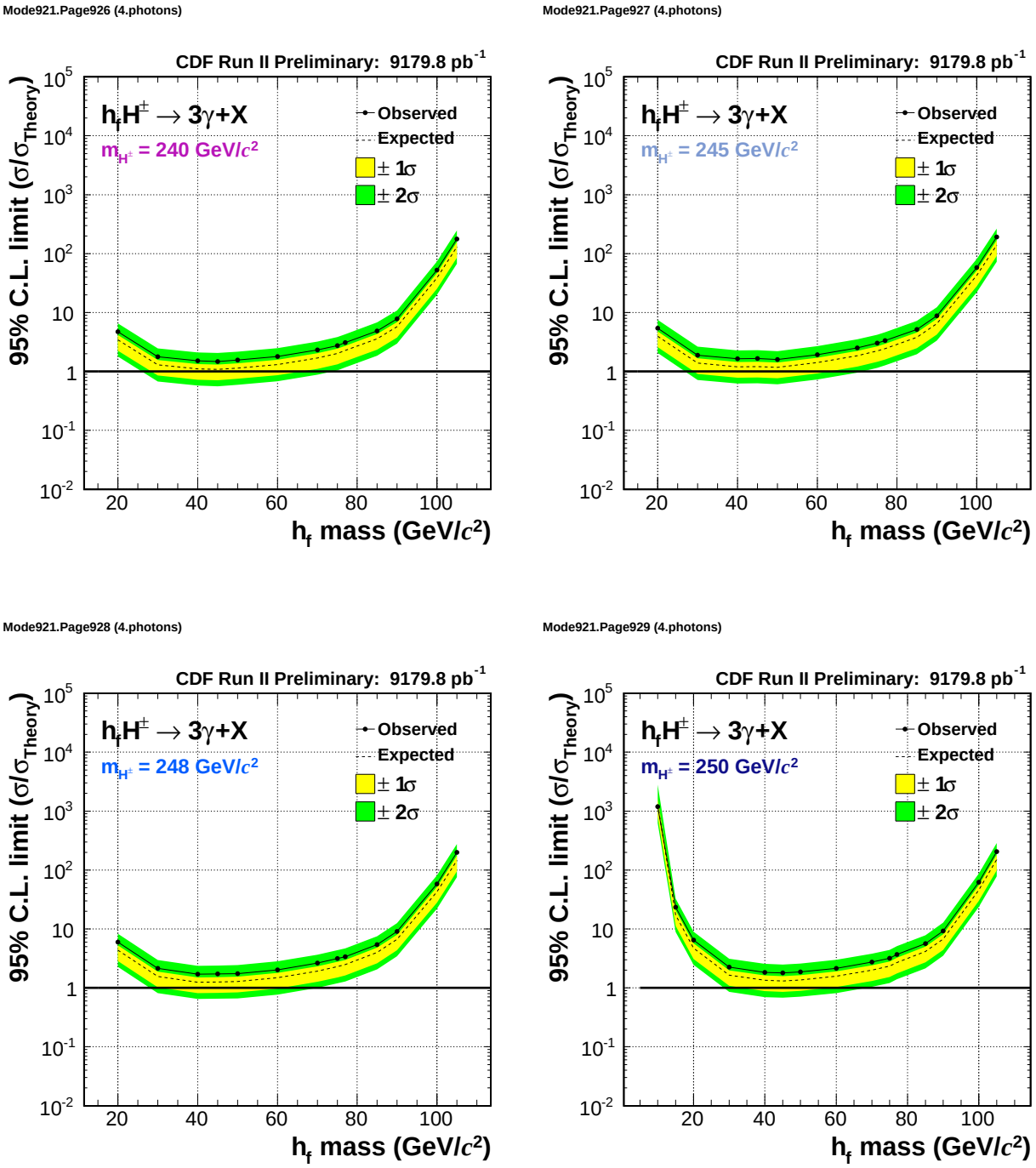

Figure 75: The expected 95% C.L. cross section limits (solid lines) and theoretical cross sections (dashed lines) calculated for the case of applying $E_T^{\gamma 1} + E_T^{\gamma 2} > 90$ GeV and $\tan\beta = 3$.

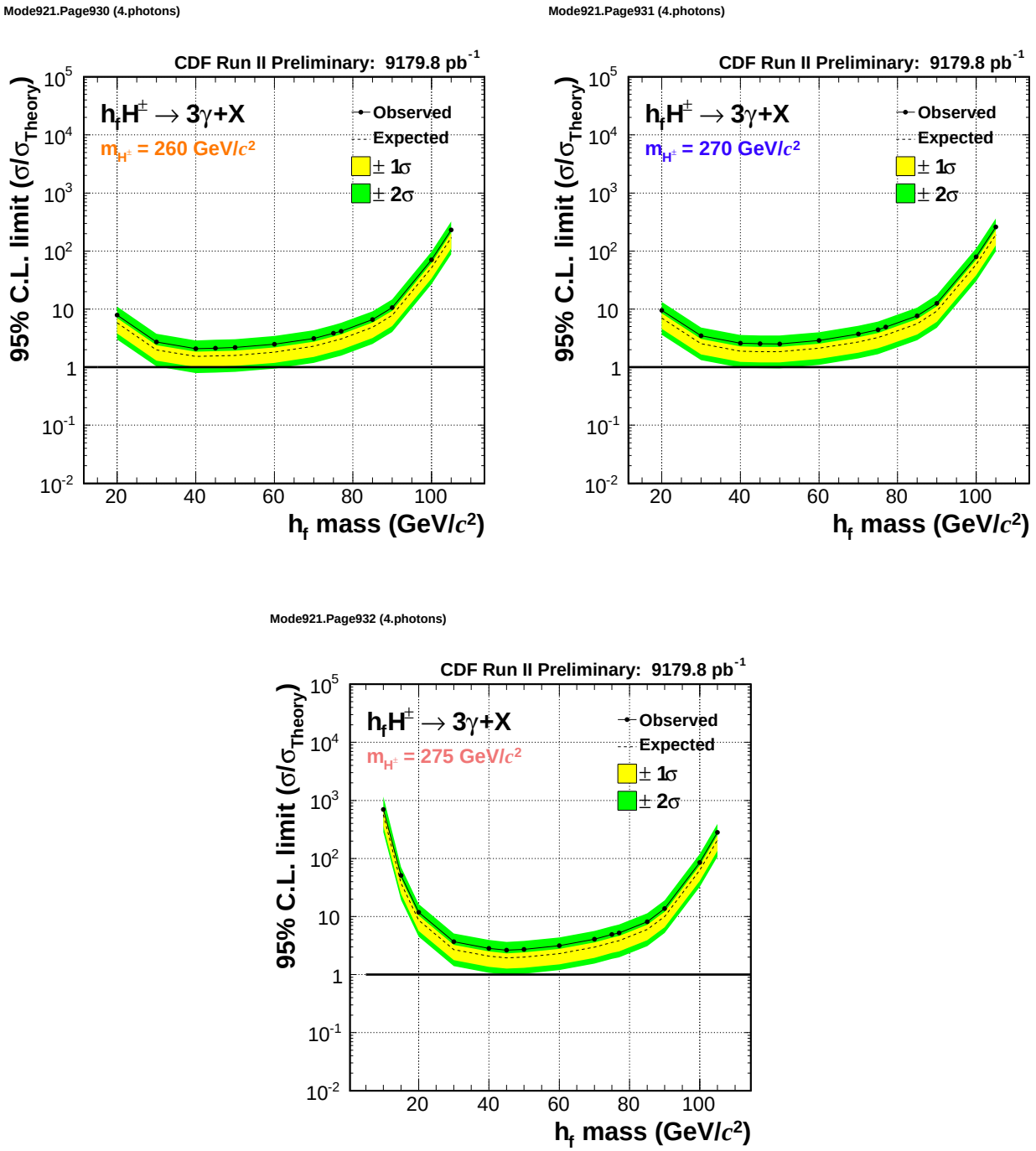

Figure 76: The expected 95% C.L. cross section limits (solid lines) and theoretical cross sections (dashed lines) calculated for the case of applying $E_T^{\gamma 1} + E_T^{\gamma 2} > 90$ GeV and $\tan\beta = 3$.

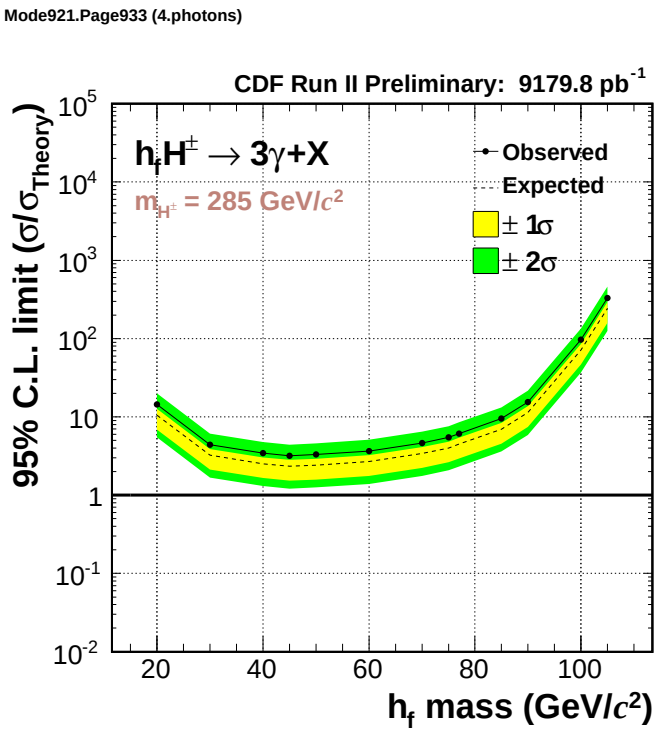

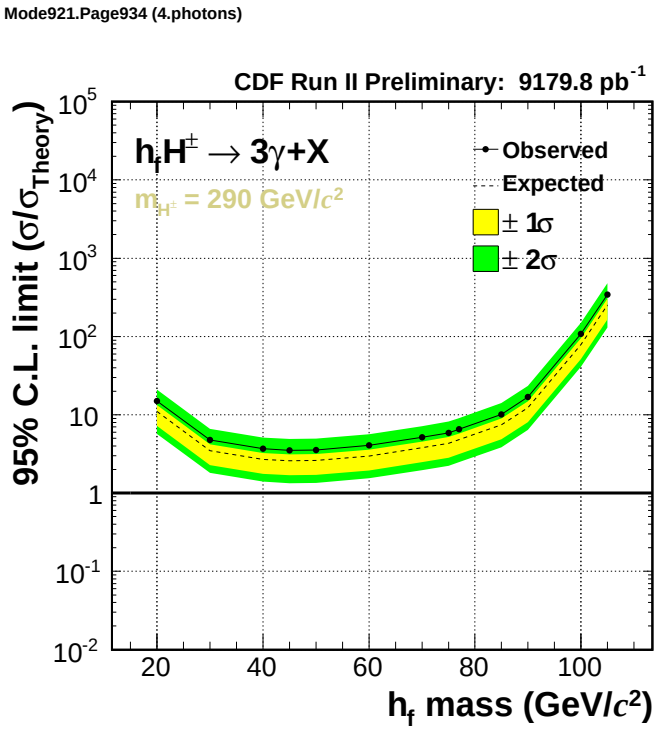

Figure 77: The expected 95% C.L. cross section limits (solid lines) and theoretical cross sections (dashed lines) calculated for the case of applying $E_T^{\gamma 1} + E_T^{\gamma 2} > 90$ GeV and $\tan\beta = 3$.

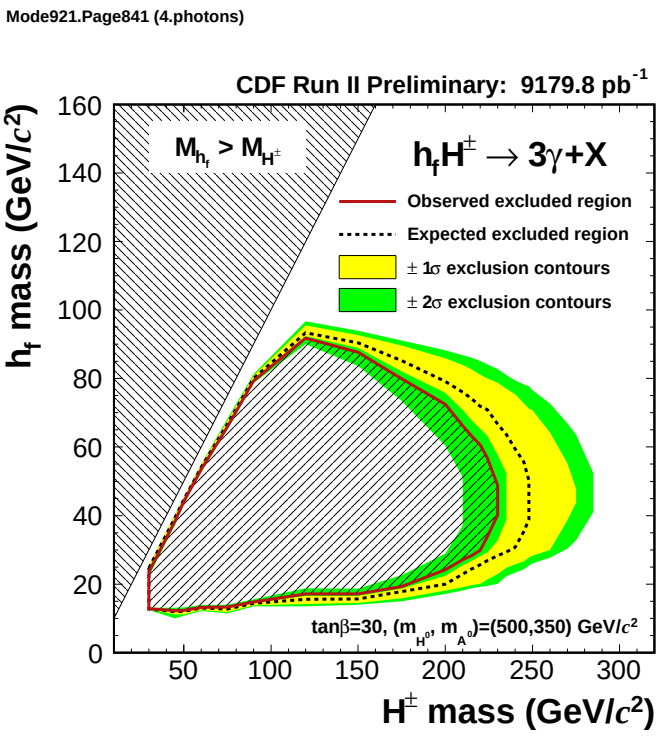

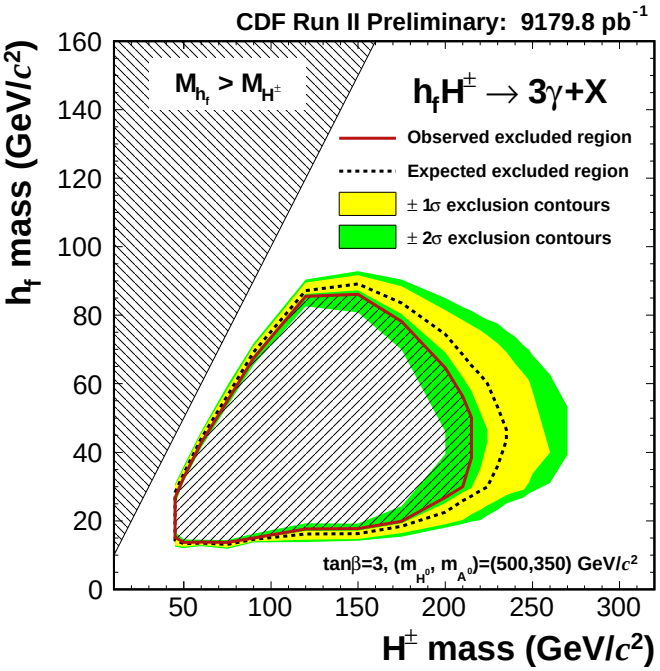

Figure 78: The expected and observed 95% C.L. excluded mass region calculated for the case of applying $E_T^{\gamma 1} + E_T^{\gamma 2} > 90$ GeV. The top plot corresponds to $\tan\beta = 30$ and the bottom plot $\tan\beta = 3$.

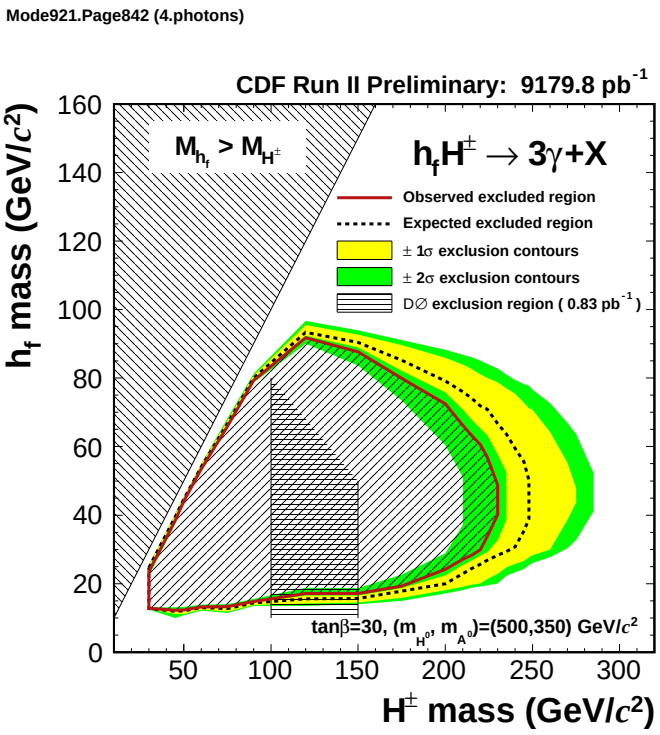

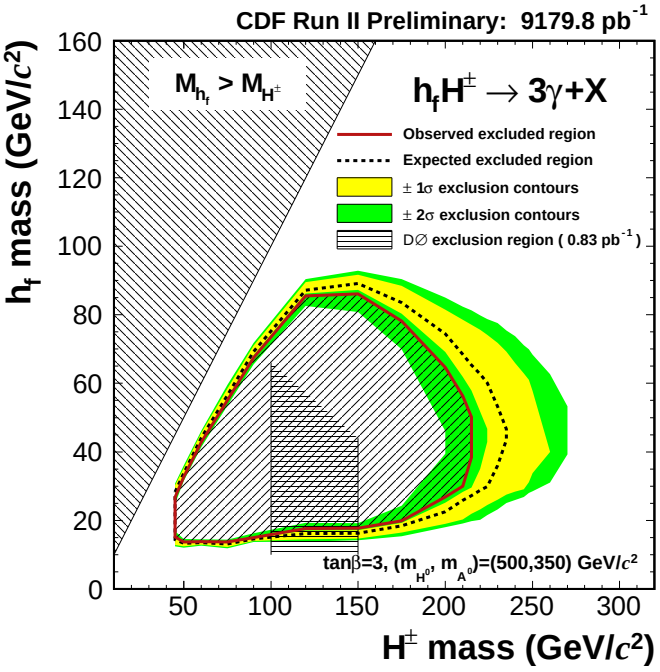

Figure 79: The expected and observed 95% C.L. excluded mass region calculated for the case of applying $E_T^{\gamma 1} + E_T^{\gamma 2} > 90$ GeV. The top plot corresponds to $\tan\beta = 30$ and the bottom plot $\tan\beta = 3$. As a reference, the excluded h_f masses by the DØ analysis are also shown in terms of two vertical lines. The shaded region between the lines are considered to be naturally excluded.

References

[1] ATLAS Collaboration, "Observation of a new particle in the search for the Standard Model Higgs boson with the ATLAS detector at the LHC", Phys. Lett. B716, 1 (2012); CMS Collaboration, "Observation of a new boson at a mass of 125 GeV with the CMS experiment at the LHC", Phys. Lett. B716, 30 (2012); CMS Collaboration, "Study of the Mass and Spin-Parity of the Higgs Boson Candidate via Its Decays to Z Boson Pairs", Phys. Rev. Lett. 110, 081803 (2013); ATLAS Collaboration, "Evidence for the spin-0 nature of the Higgs boson using ATLAS data", Phys. Lett. B726, 120 (2013);

[2] ATLAS Collaboration, "Evidence for Higgs Boson Decays to the $\tau^+\tau^-$ Final State with the ATLAS Detector", ATLAS-CONF-2013-108; CMS Collaboration, "Evidence for the direct decay of the 125 GeV Higgs boson to fermions", arXiv:1401.6527.

[3] H.E.Haber, G.L.Kane, and T.Sterling, Nucl. Phys. B161, 493 (1979).

[4] A. Stange, W.J. Marciano, and S. Willenbrock, Phys. Rev. D 49, 1354 (1994).

[5] M.A. Diaz and T.J. Weiler, hep-hp/9401259.

[6] V. Lemaitre for the ALEPH, DELPHI, L3, and OPAL collaborations, "Search for fermiophobic Higgs at LEP", Fundamental Interactions: Proceedings of the 20th Lake Louise Winter Institue, Canada, p199–203.

[7] The Tevatron New-Phenomena and Higgs Working Group for the CDF and DØ Collaborations, "Combined CDF and DØ Upper Limits on Fermiophobic Higgs Boson Production with up to 8.2 fb^{-1} of $p\bar{p}$ Data", arXiv:1302.1764, Supersymmetry 2011: 19th International Conference on Supersymmetry and Unification of Fundamental Interactions.

[8] ATLAS Collaboration, "Search for a fermiophobic Higgs boson in the diphoton decay channel with the ATLAS detector", Eur. Phys. J. C 72, 2157 (2012);

CMS Collaboration, "Searches for Higgs bosons in pp collisions at $\sqrt{s} = 7$ and 8 TeV in the context of four-generation and fermiophobic models", Phys. Lett. B 725, 36 (2013);

[9] A.G. Akeroyd and M.A. Díaz, Phys. Rev. D 67, 095007 (2003); A.G Akeroyd, A. Alves, M.A. Díaz, and O. Éboli, Eur. Phys. J. C48, 145 (2006).

[10] Since the production process that we consider in our analysis goes through a virtual W, the K factor similar to the one for the W production can be a reasonable choice.

[11] DØ Collaboration, "Search for Fermiophobic Higgs Boson in $3\gamma + X$ Events", DØ Note 5067-CONF.

[12] http://www-cdf.fnal.gov/internal/physics/photon/docs/cuts.html

[13] M. Dorigo and Shin-Shan Eiko Yu, "Diphoton Trigger Efficiency Study in 3 fb^{-1} of CDF II data", CDF Note 9533.

[14] C. Group, R. Culbertson, J. Ray, "Photon Efficiency Scale Factors", CDF Note 9429; Karen Bland, Jay Dittmann, Craig Group, Ray Culbertson, and Jamie Ray, "Photon Efficiency Scale Factors (p0–p23)", CDF Note 10038.

[15] O. Gonzalez and C. Rott, "Uncertainties due to the PDFs for the gluino-sbottom search", CDF Note 7051.

[16] http://www-cdf.fnal.gov/internal/physics/joint-physics/agenda/20050527-minutes.html

[17] C. Lester, J. Deng, A. Goshaw, B. Heinemann, A. Nagano, T. Phillips, "Measurement of the Rate of Jets Faking Central Isolated Photons Using 1 fb^{-1} of Data", CDF Note 9033.

[18] http::/www.mcfm.fnal.gov

[19] R. Rossin, "Systematics on the Luminosity Measurement", CDF Detector Lectures (http://fcdfwww.fnal.gov/internal/WebTalks/Archive/0410);

S. Klimenko, J. Konigsberg and T.M. Liss, FERMILAB-FN-0741 (2003).

[20] Luc Demortier, "Objective Bayesian Upper Limits for Poisson Processes", CDF Note 5928 (version 2.10); Joel Heinrich, Craig Blocker, John Conway, Luc Demortier, Louis Lyons, Giovanni Punzi, and Pekka K. Sinervo, "Inteval estimation in the presence of nuisance parameters. 1. Bayesian approach", CDF Note 7117 (September 27, 2004).

[21] S. Dawson, S.Dittmaier, and M. Spira, Phys. Rev. D 58, 115012 (1998).

[22] Craig Blocker, John Conway, Luc Demortier, Joel Heinrich, Tom Junk, Louis Lyons, and Giovanni Punzi, "Simple Facts about P-Values", CDF Note 8023.